

**Atomistic modeling of the solid-state chemistry  
of actinide materials**

**by**

**Lindsay C. Shuller**

A dissertation submitted in partial fulfillment  
of the requirements of the degree of  
Doctor of Philosophy  
(Materials Science and Engineering)  
in The University of Michigan  
2010

Doctoral Committee:

Professor Rodney C. Ewing, Co-Chair  
Professor Udo Becker, Co-Chair  
Professor Ronald F. Fleming  
Professor John Kieffer  
Assistant Professor Anton Van der Ven  
Professor Peter C. Burns, University of Notre Dame

© Lindsay C. Shuller  
2010

To my husband Blake

## Acknowledgements

I would like to start by thanking my husband, as of October 16<sup>th</sup>, Blake Nickles, for his continuous love, patience, and support. He has stood by my side every step of this process and made 200+ miles seem not so far. I also could not have kept my sanity without the constant love and support of my family – Jan and Don Shuller, Susan Shuller and Max Franz, Debbie and Steve Nickles, and Kristina, Patrick, and Alex Woodward. They were able to provide inspiration to my work without fully understanding the subject matter.

After nine years at Michigan, five of which I was a graduate student, I have met many people without whom my experience would not be complete. I decided to remain at Michigan for graduate school after working for one year as an undergraduate student in Rod Ewing and Udo Becker's group. I was given unpaired guidance as an undergraduate researcher by my mentor, Frannie Skomurski. She taught me that research was fun and provided constant encouragement and guidance as I began developing my thesis topic. Frannie has continued to support me academically and personally as both a mentor and friend.

My co-advisors, Rod Ewing and Udo Becker, have given me such a unique graduate experience. They provided the academic foundation for truly interdisciplinary research and encouraged me from the start to think creatively about science and problem solving. With their excellent guidance and superior leadership, I have had the opportunity to assist

with writing successful (and unsuccessful) grant proposals, presenting at conferences and workshops, both nationally and internationally, and discussing science with some of the brightest students, faculty, and researchers.

The rest of my dissertation committee has contributed significantly to, not only my dissertation, but my development as a scientist. John Kieffer and Anton Van der Ven have been some of my most influential teachers during my undergraduate and graduate coursework. Ron Fleming and I have spent countless hours discussing the thorium-fuel cycle – a shared passion. Peter Burns, from University of Notre Dame, has graciously agreed to serve on my dissertation committee. I appreciate his guidance from an experimental perspective. His insight into uranium and neptunium mineralogy has been irrefutably essential to my research on Np-incorporation into uranyl phases. Additionally, I have had the opportunity to get my hands “dirty” in his lab at Notre Dame, where he has allowed me to contribute to ongoing experiments looking at the corrosion of Np-doped UO<sub>2</sub>. My colleagues at University of Notre Dame – Ginger Sigmon-Brown, Daniel Unruh, and Jen Szymanowski – provided valuable assistance while I worked in their lab and made me feel like part of their research group.

I could never have completed paper work on time or as easily if it weren’t for the support staff in Materials Science and Engineering (Renee Hilgendorf) and Geology (Anne Hudon and Nancy Kingsbury). I would like to further thank Anne Hudon, without whom I would never have figured out my fellowship and would probably have had lapses in my health insurance. Furthermore, the level of computational support that I have received in my time at Michigan will be untouched. I am forever grateful to Janine

Taylor for being such a great computer doctor and to Mike Messina for helping on the research side of computer issues.

I had the privilege to work with Eric Essene, Carl Henderson, and Anja Schleicher, during my stint as a graduate assistant in the Central Campus Electron Microscopy Analysis Lab (EMAL). I learned a tremendous amount from them about mineralogy and microscopy.

I would like to thank Joanna Mirecki-Millunchick for giving me the opportunity to teach two semesters as her assistant. It was an honor to work with someone who obviously cares so much about her teaching. Additionally, I would like to thank Joanna for including me in her pedagogical research team. I have learned so much about teaching and pedagogical research from her and our colleague Tershia Pinder-Grover.

Many great friends provided interesting conversation and fun times during my years in graduate school. My roommates – both human and canine – helped keep me sane and provided loads of entertainment. Thanks to Kristen Parrish, Julie Sturza, Laura Povlich, Chris Nelson, and Leo Arnaboldi-Becker. Special thanks goes to Devon Renock. He was not only a lunch buddy, co-teacher, and lab-mate, but a great friend. And last, but not least, my colleagues at Michigan, who provided endless conversation about science, culture, and life – Subashis Biswas, Amy Bengston, Artur Deditius, Darius Dixon, Martin Reich, Elizabeth Ferriss, Qiaona Hu, Maik Lang, Jie Lian, Veronique Pointeau, Zsolt Rak, Chintalapalle Ramana, Sandra Rey, Rosa Sureda, Satoshi Utsunomiya, Jianwei Wang, Fuxiang Zhang, Jiaming Zhang.

I would like to acknowledge the Office of Civilian and Radioactive Waste Management Fellowship for three years of graduate support. Supplemental support was

provided by U.S. Department of Energy Office of Basic Energy Sciences (Grant DE FG02 06ER15783) and U.S. Department of Energy Nuclear Energy University Program (Grant DE-AC07-05ID14517). I have also been able to interact with great colleagues as part of the Materials Science of Actinides, an Energy Frontier Research Center funded by the U.S. Department of Energy, Office of Science, Office of Basic Energy Sciences under Award Number DE-SC0001089. Computational resources were provided by the NSF-NIRT grant (EAR-0403732)

## Table of Contents

<b>Dedication .....</b>	<b>ii</b>
<b>Acknowledgements .....</b>	<b>iii</b>
<b>List of Figures.....</b>	<b>xi</b>
<b>List of Tables .....</b>	<b>xiv</b>
<b>Abstract.....</b>	<b>xvi</b>
<b>Chapter 1 Introduction.....</b>	<b>1</b>
References.....	12
Publications and abstracts resulting from this dissertation.....	15
Publications and abstracts resulting from side-projects.....	17
<b>Chapter 2 Thermodynamic properties of <math>\text{Th}_x\text{U}_{1-x}\text{O}_2</math> (<math>0 &lt; x &lt; 1</math>) based on quantum-mechanical calculations and Monte-Carlo simulations.....</b>	<b>19</b>
Abstract.....	19
Introduction.....	20
Methodology .....	22
Quantum-mechanical calculations .....	23
Generating interaction parameters .....	24
Monte-Carlo simulations .....	28
Structure analysis of quantum-mechanical calculations .....	29
Thermodynamic properties of mixing .....	32

Composition of natural and synthetic $\text{Th}_x\text{U}_{1-x}\text{O}_2$ .....	43
Comparison with calorimetric measurements.....	45
Implications for $\text{Th}_x\text{U}_{1-x}\text{O}_2$ solid solutions .....	48
References.....	49
<b>Chapter 3 Atomistic calculations of the thermodynamic properties of mixing for tetravalent metal dioxide solid solutions: <math>(\text{Zr},\text{Th},\text{Ce})\text{O}_2</math> .....</b>	<b>54</b>
Abstract.....	54
Introduction.....	55
Methods.....	56
Results.....	57
Discussion .....	63
Exsolution tendency.....	63
Cation ordering and end-member stability .....	69
Miscibility limit .....	73
Conclusions.....	76
References.....	77
<b>Chapter 4 Quantum-mechanical evaluation of Np-incorporation into stutdtite.....</b>	<b>80</b>
Abstract.....	80
Introduction.....	81
Methods.....	85
Quantum-mechanical calculations .....	85
Calculation of incorporation energies.....	87

Calculations of the thermodynamic properties of the $(U^{6+}, Np^{6+})$ -studtite solid solution.....	89
Results and Discussion .....	91
Refined crystal structure .....	91
Electronic structure of studtite .....	96
Electronic structure of $(Np^{6+}_{0.25} U^{6+}_{0.75})$ -studtite .....	100
Thermodynamics of Np-incorporation into studtite .....	107
Thermodynamic properties of the $(U, Np)$ -studtite solid solution.....	113
Concluding Remarks.....	118
Appendix 1: $Np^{6+}$ -modified studtite .....	118
Appendix 2: $Np^{5+}$ -modified studtite .....	120
References.....	122
<b>Chapter 5 Np-incorporation into uranyl phases: A quantum-mechanical evaluation</b>	
.....	<b>128</b>
Abstract.....	128
Introduction.....	129
Boltwoodite: Occurrence and structure .....	132
Computational Methodology .....	134
What is the meaning of the CASTEP energy?.....	136
Calculating incorporation energies .....	138
Estimating the limit of Np-incorporation.....	141
Results.....	143
Substitution mechanism I: $Np^{5+} + H^+ \leftrightarrow U^{6+}$ .....	143

Substitution mechanism II: $\text{Np}^{5+} + \text{Ca}(\text{Mg})^{2+} \leftrightarrow \text{U}^{6+} + \text{K}^+$ .....	145
Substitution mechanism III: $\text{Np}^{5+} + \text{P}^{5+} \leftrightarrow \text{U}^{6+} + \text{Si}^{4+}$ .....	148
Discussion .....	148
Reference phase comparison.....	148
Limit of Np-incorporation.....	156
Impact of boltwoodite chemistry on Np incorporation.....	160
Feasibility of reaction mechanisms.....	161
Implications.....	166
References.....	167
<b>Chapter 6 Conclusions.....</b>	<b>174</b>
References.....	181

## List of Figures

Figure 1.1. Schematic of the open (blue) and closed (red) fuel cycle, where the steps present in both cycles are in black, which is a majority of the cycle.....	2
Figure 1.2. A schematic of UNF showing (left) where elements migrate during and after production in a nuclear reaction.....	5
Figure 2.1. Uraninite ( $\text{UO}_{2+x}$ ) and thorianite ( $\text{ThO}_2$ ) have the fluorite crystal structure, where the cations are octahedrally coordinated .....	25
Figure 2.2. (a) The weighted average of the quantum-mechanical calculations and experimental measurements (Hubert et al., 2006) lattice parameter <i>versus</i> concentration results are in agreement with Vegard's law .....	30
Figure 2.3. The calculated nearest-neighbor $\langle \text{Th-O} \rangle$ and $\langle \text{U-O} \rangle$ bond lengths are corrected for the 0.3% mismatch in the lattice parameter and compared with EXAFS measurements.....	34
Figure 2.4. Thermodynamic mixing properties with respect to concentration Th and temperature from the Monte-Carlo simulation .....	35
Figure 2.5. Estimated temperature-composition phase diagram indicating the miscibility gap in the $\text{Th}_x\text{U}_{1-x}\text{O}_2$ binary. ....	37
Figure 2.6. Schematic of cations indicating the (a) random arrangement of cations... (b) alternating U and Th layers...and (c) exsolved lamellae structure.....	38
Figure 2.7. Example Gibbs free energy of mixing curves <i>versus</i> composition .....	40
Figure 2.8. (a) Comparison of Monte-Carlo results at 1000 K and 1500 K with enthalpy of mixing from Kandan et al. (2009)...(b) Comparison of Monte-Carlo results at 1500 K with Gibbs free energy of mixing from Dash et al. (2009). ....	46
Figure 3.1. Positive enthalpy of mixing for the $\text{Th}_x\text{Zr}_{1-x}\text{O}_2$ , $\text{Ce}_x\text{Zr}_{1-x}\text{O}_2$ , and $\text{Th}_x\text{Ce}_{1-x}\text{O}_2$ binaries indicates some unmixing.....	60

Figure 3.2. Gibbs free energy of mixing curves indicating exsolution below 600 K for Th <sub>x</sub> Ce <sub>1-x</sub> O <sub>2</sub> , 3000 K for Ce <sub>x</sub> Zr <sub>1-x</sub> O <sub>2</sub> and Th <sub>x</sub> Zr <sub>1-x</sub> O <sub>2</sub> .....	61
Figure 3.3. Temperature-composition phase diagram showing miscibility gaps for the Th <sub>x</sub> Ce <sub>1-x</sub> O <sub>2</sub> , Ce <sub>x</sub> Zr <sub>1-x</sub> O <sub>2</sub> , and Th <sub>x</sub> Zr <sub>1-x</sub> O <sub>2</sub> binaries .....	62
Figure 3.4. Configurational entropy curves are nearly equal to the point entropy ( <i>i.e.</i> , configurational entropy without ordering).....	64
Figure 3.5. The Ce <sub>x</sub> Zr <sub>1-x</sub> O <sub>2</sub> binary displays exsolution lamellae at 100 K and $x = 0.5$ that are about two cation layers thick (~4.5 Å) and    to (10̄2) .....	68
Figure 3.6. Ordering is observed for the Th <sub>x</sub> Zr <sub>1-x</sub> O <sub>2</sub> binary at $x = 0.5$ and $T = 200$ K. ....	70
Figure 4.1. Studtite projected on the (010) showing chains of uranyl polyhedra bonded by peroxide molecules .....	83
Figure 4.2. The pre- (a) and post- (b) optimized uranyl polyhedra show the alignment of the H <sup>+</sup> parallel to the (010) plane .....	94
Figure 4.3. Partial density of states spectra of studtite over the entire calculated energy range, where interval A designates the inner valence band, interval B the outer valence band and interval C the conduction band .....	97
Figure 4.4. Electron density orbital projection between -8 and -6 eV showing O-H bonding in water molecules as well as hydrogen bonding between the water molecules and uranyl polyhedra. ....	99
Figure 4.5. Comparison of the total DOS for studtite (solid curve) and (Np <sup>6+</sup> <sub>0.25</sub> U <sup>6+</sup> <sub>0.75</sub> )-studtite (dotted curve). ....	101
Figure 4.6. Band structure showing the band gap of studtite ( $E_{gap} = 2.29$ eV) and (Np <sup>6+</sup> <sub>0.25</sub> U <sup>6+</sup> <sub>0.75</sub> )-studtite ( $E_{gap} = 1.09$ eV) .....	103
Figure 4.7. PDOS of (Np <sup>6+</sup> <sub>0.25</sub> U <sup>6+</sup> <sub>0.75</sub> )-studtite highlighting the 5f orbital contribution from the Np in the peroxide chain, Np-neighboring U in the peroxide chain, and U-neighboring U in the peroxide chain.....	105
Figure 4.8. PDOS of (Np <sup>6+</sup> <sub>0.25</sub> U <sup>6+</sup> <sub>0.75</sub> )-studtite highlighting the 2s and 2p orbital contribution from the Np-bonded and U-bonded peroxide oxygen.....	106
Figure 4.9. Enthalpy of mixing (kJ/mol exchangeable cation), configurational entropy of mixing (kJ/K mol exchangeable cation), and Gibbs free energy of mixing (kJ/mol	

exchangeable cation) <i>vs.</i> concentration of Np for $(\text{Np}^{6+}_{0.25}\text{U}^{6+}_{0.75})$ -studtite solid solution.....	115
Figure 5.1. This pale yellow to amber specimen from Rossing Mine, Arandis, Swakopmund District, Erongo Region, Namibia .....	133
Figure 5.2. Boltwoodite sheet structure shown from two directions: (a) uranyl sheet in which chains of edge-sharing uranyl polyhedra .....	135
Figure 5.3. Flowchart describing the relationship between formation energy, CASTEP energy, and lattice energy for $\text{UO}_2$ . ....	137
Figure 5.4. Boltwoodite unit cell showing possible locations for the charge-balancing $\text{H}^+$ . The table inset shows the Np-incorporation energy based for each $\text{H}^+$ location. ....	144
Figure 5.5. Boltwoodite unit cell indicating the distance between the two possible interlayer-cation substitution sites and the neptunium polyhedron. ....	147
Figure 5.6. Enthalpy of mixing ( $\Delta H_{mix}$ ) <i>versus</i> composition for the solid-solution series based on the coupled substitution of $\text{Np}^{5+}$ and $\text{P}^{5+}$ for $\text{U}^{6+}$ and $\text{Si}^{4+}$ .....	158
Figure 5.7. Schematic of the alpha-uranophane anion topology, composed of chains of edge-sharing pentagons.....	165

## List of Tables

Table 2.1. Margules and interaction parameters fit for $1 \times 1 \times 1$ unit cells and $2 \times 1 \times 1$ unit cells.....	27
Table 2.2. Comparison of calculated unit cell length with measured values.....	31
Table 2.3. Comparison of calculated $\langle \text{Me-O} \rangle$ (Me = Th, U) bond lengths with measured values.....	33
Table 3.1. Cation-cation exchange fit parameters including Margules parameters ( $W_1$ and $W_2$ ), interaction parameters ( $J_{I-5}$ ), and the correlation coefficient for the fit.....	59
Table 4.1. Comparison of measured unit-cell parameters and optimized unit-cell parameters of the conventional unit cell of studtite, $(\text{Np}^{6+}_{0.25}, \text{U}^{6+}_{0.75})$ -studtite, and $(\text{Np}^{5+}_{0.25}, \text{U}^{6+}_{0.75})$ -studtite.....	92
Table 4.2. Optimized unit-cell parameters, fractional atomic coordinates, and bond distances and angles for studtite.....	95
Table 4.3. Incorporation equations and energies for $\text{Np}^{6+}$ in studtite with various reference phases.....	108
Table 4.4. Incorporation equations and energies for $\text{Np}^{5+}$ in studtite with various reference phases.....	112
Table 4.5. Enthalpy of formation from the oxide components for studtite, $\text{Np}^{6+}$ -studtite, $\text{UO}_3$ , $\text{NpO}_3$ .....	117
Table 5.1. Lattice energy (eV) for $\text{UO}_2$ as calculated from various combinations of methods.....	139
Table 5.2. Incorporation energies for coupled substitution of $\text{Np}^{5+}$ and $\text{Ca}^{2+}$ or $\text{Mg}^{2+}$ for $\text{U}^{6+}$ and $\text{K}^+$ in boltwoodite .....	146
Table 5.3. Stoichiometric reactions describing the coupled-substitution of $\text{Np}^{5+}$ and $\text{H}^+$ for $\text{U}^{6+}$ in boltwoodite .....	150

Table 5.4. The estimated limit of Np-incorporation into boltwoodite for the coupled-substitution of $\text{Np}^{5+}$ and $\text{P}^{5+}$ for $\text{U}^{6+}$ and $\text{Si}^{4+}$ .....	159
---	-----

## Abstract

Materials that incorporate actinides are critical to the nuclear fuel cycle, either as nuclear fuels or nuclear waste forms. In this thesis, I examine four materials: *i*) ThO<sub>2</sub>-UO<sub>2</sub> solid solutions, *ii*) binary ThO<sub>2</sub>-CeO<sub>2</sub>-ZrO<sub>2</sub> solid solutions, *iii*) Np-doped studtite, *iv*) Np-doped boltwoodite. Computational methods, particularly density functional theory (DFT) calculations and Monte-Carlo (MC) simulations, are used to determine the energetics and structures of these actinide-bearing materials. The solid-solution behavior of nuclear fuels and nuclear waste forms indicate the thermodynamic stability of the material, which is important for understanding the in-reactor fuel properties and long-term stability of used fuel.

The Th<sub>x</sub>U<sub>1-x</sub>O<sub>2</sub> and Th<sub>x</sub>Ce<sub>1-x</sub>O<sub>2</sub> binaries are almost completely miscible; however,  $\Delta G_{mix}$  reveals a small tendency for the systems to exsolve (*e.g.*,  $\Delta E_{exsoln}(\text{Th}_x\text{U}_{1-x}\text{O}_2) = 0.13 \text{ kJ/(mol cations)}$  at 750 K). Kinetic hindrances (*e.g.*, interfacial energy) may inhibit exsolution, especially at the low temperatures necessary to stabilize the nanoscale exsolution lamellae observed in the Th<sub>x</sub>U<sub>1-x</sub>O<sub>2</sub> and Ce<sub>x</sub>Zr<sub>1-x</sub>O<sub>2</sub> binaries. Miscibility in the Zr-bearing binaries is limited. At 1400 °C, only 3.6 and 0.09 mol% ZrO<sub>2</sub> is miscible in CeO<sub>2</sub> and ThO<sub>2</sub>, respectively.

The incorporation of minor amounts of Np<sup>5+,6+</sup> into uranium alteration phases, *e.g.*, studtite [UO<sub>2</sub>O<sub>2</sub>(H<sub>2</sub>O)<sub>4</sub>] or boltwoodite [K(UO<sub>2</sub>)(SiO<sub>3</sub>OH)(H<sub>2</sub>O)<sub>1.5</sub>], may limit the mobility of aqueous neptunyl complexes released from oxidized nuclear fuels. Np<sup>6+</sup>-incorporation into studtite requires less energy than Np<sup>5+</sup>-incorporation (*e.g.*, with source/sink = Np<sub>2</sub>O<sub>5</sub>/UO<sub>3</sub>  $\Delta E_{incorp}(\text{Np}^{6+}) = 0.42 \text{ eV}$  and  $\Delta E_{incorp}(\text{Np}^{5+}) = 1.12 \text{ eV}$ ). In addition, Np<sup>6+</sup> is completely miscible in studtite at room temperature with respect to a hypothetical Np<sup>6+</sup>-studtite. Electronic structure calculations provide insight into Np-bonding in studtite. The Np 5f orbitals are within the band gap of studtite, resulting in

the narrowing of the band gap from 2.29 eV for studtite to 1.09 eV for Np-incorporated studtite.

Three charge-balancing mechanisms for the substitution of  $\text{Np}^{5+}$  for  $\text{U}^{6+}$  were compared: *i*) addition of  $\text{H}^+$  [ $\Delta E_{incorp}(\text{bolt}) = 0.79 \text{ eV}$ ;  $\Delta E_{incorp}(\text{stud}) = 1.12 \text{ eV}$ ], *ii*) interlayer coupled substitution [ $\Delta E_{incorp}(\text{bolt}) = 1.40 \text{ eV}$ ], *iii*) intra-layer coupled-substitution [ $\Delta E_{incorp}(\text{bolt}) = 0.86 \text{ eV}$ ]. Solid-solution calculations of the intra-layer coupled-substitution mechanism, where  $\text{Np}^{5+}$  and  $\text{P}^{5+}$  substitute for  $\text{U}^{6+}$  and  $\text{Si}^{4+}$ , predict an incorporation limit of 585 ppm at 300 °C.

# **Chapter 1**

## **Introduction**

Increasing global awareness on issues of climate change and the need for alternative energy has sparked a “Nuclear Renaissance.” Nuclear energy is a sustainable, carbon-neutral energy resource; however, many scientific obstacles, specifically materials challenges, need to be overcome for nuclear energy to take hold globally (Guerin et al., 2009).

In both an open (*i.e.*, direct disposal) and a closed (*i.e.*, reprocessing) fuel cycle, used nuclear fuel (UNF) is destined for long term geologic disposal (Figure 1.1) modified from Ewing, 2006). For the once-through fuel cycle, which is currently used for commercial UNF in the United States, the long-term disposal plan is that the UNF be directly disposed in a geologic repository. During reprocessing, the short-lived fission products  $^{137}\text{Cs}$  and  $^{90}\text{Sr}$  are removed to drastically reduce the radioactivity and heat load of the waste. U and Pu are extracted from the waste for reuse as new fuel, typically a mixed oxide fuel ( $\text{Pu}_x\text{U}_{1-x}\text{O}_2$ ). Less than 1% of the original U and Pu remain in the waste after reprocessing; however, according to the current separations plans in the United States, other actinides, such as Th, Np, and Am remain in the waste stream (Ewing, 2010).

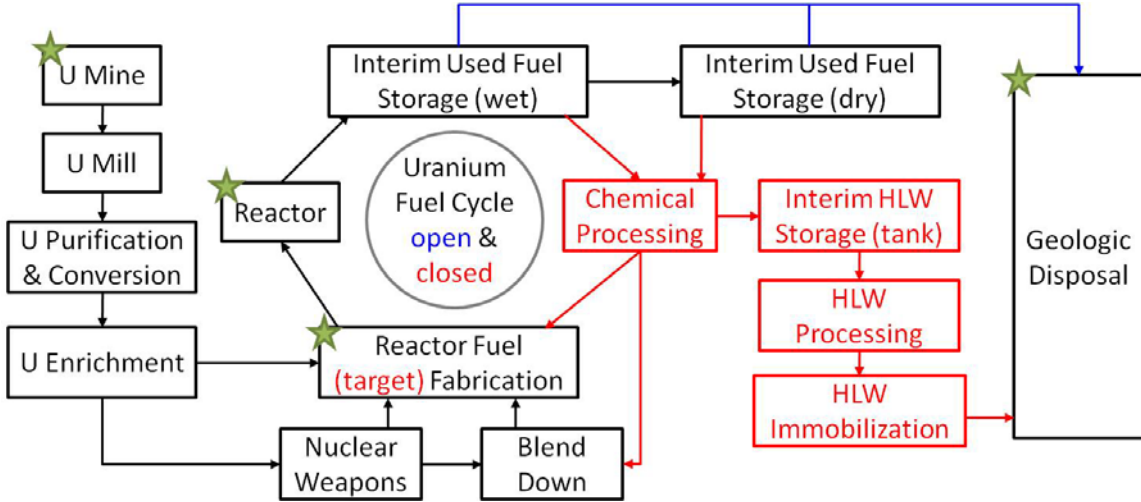


Figure 1.1. Schematic of the open (blue) and closed (red) fuel cycle, where the steps present in both cycles are in black, which is a majority of the cycle. The green stars indicate steps of the fuel cycle where materials properties calculated in this thesis are relevant. Note that for both the open and closed fuel cycle, the end stage is geologic disposal. Figure modified from (Ewing, 2006), where the figure was reprinted with permission from *End Points of Spent Nuclear Fuel and High-Level Radioactive Waste in Russia and the United States* by the National Academy of Sciences (National Research Council 2003).

Thus, even if the used fuel is reprocessed, some waste is generated that requires long-term geologic disposal.

There are many parts of the nuclear fuel cycle that have materials challenges. For example, the development of harder and more radiation resistant cladding material is crucial to extending the longevity and enhancing the safety of a reactor (Allen et al., 2008; Guerin et al., 2009; Zinkle and Busby, 2009). In terms of reprocessing, a huge research initiative is focused on developing compounds that can target and separate specific radionuclides. For example, the newly patented thorium borate ( $[\text{ThB}_5\text{O}_6(\text{OH})_6][\text{BO}(\text{OH})_2] \cdot 2.5\text{H}_2\text{O}$ ) capable of anionic exchange could be used to separate radionuclides, specifically  $\text{TcO}_4^-$ , from UNF (Wang et al., 2010). Decades of research has focused on the development and understanding of waste immobilization matrices, such as borosilicate glass or pyrochlore (Donald et al., 1997; Ewing et al., 2004; Lutze and Ewing, 1988). This thesis is focused on the thermochemistry of actinide oxides from their natural state (*e.g.*, uranothorianite) to their use as fuels (*e.g.*,  $\text{Th}_x\text{U}_{1-x}\text{O}_2$ ), and finally, to their altered radioactive waste forms (*e.g.*, uranyl minerals).

Uranium dioxide ( $\text{UO}_2$ ) is the primary nuclear fuel. After use in a commercial light water reactor with a burnup of 40 MWd/kg of U (MegaWatt days/kg of uranium), 96% of the  $\text{UO}_2$  remains, while 3% is converted to fission products (*e.g.*, Cs, Sr, Tc) and 1% transuranium elements (*e.g.*, Th, Np, Pu) (Bruno and Ewing, 2006). The volatile radionuclides form fission gas bubbles (*e.g.*, Xe, Kr, I), while others migrate to the grain boundaries (*e.g.*, Cs, Se, Tc). During a nuclear reaction, the fuel pellet expands and cracks releasing the radionuclides into the gap region between the pellet and the cladding. Radionuclides in the grain boundaries and gap region are immediately released upon

contact with water. Other fission products form oxide or  $\varepsilon$ -particle/metallic precipitates within the fuel matrix (left side of Figure 1.2). The release of these elements is slow and depends on the dissolution rate of the fuel matrix. Many of the actinides and lanthanides (*e.g.*, Ce, Th, Np, Pu) are expected to be in solid solution with the UO<sub>2</sub> matrix; however, nanoscale exsolution or cation-ordering may occur, which can affect properties such as the thermal conductivity of the fuel. The homogeneity of the dioxide solid solutions is also important for the development of mixed oxide fuels (*e.g.*, Th<sub>x</sub>U<sub>1-x</sub>O<sub>2</sub>) and inert matrix fuels (*e.g.*, U<sub>x</sub>Zr<sub>1-x</sub>O<sub>2</sub>). Interestingly, UO<sub>2</sub> corrodes more readily as compared with ThO<sub>2</sub> (Demkowicz et al., 2004; Skomurski et al., 2008). Thus, the addition of Th into the UO<sub>2</sub> matrix of nuclear fuel can have a significant impact on the long term corrosion resistance of the UNF.

Safety assessment for a nuclear waste repository or an environmental remediation site necessitates the evaluation of the mobility of radionuclides exposed to the environment. Although initially the waste is protected by barriers, such as stainless steel waste containers and geologic media (*e.g.*, bentonite clay is a proposed back-fill for repository tunnels in France), the waste will eventually be exposed to groundwater. If the radioactive waste comes into contact with water, several processes occur (right side of Figure 1.2). Radiolysis of the water in contact with the radioactive waste causes the generation of oxidants, such as, H<sub>2</sub>O<sub>2</sub>, (Amme, 2002). The oxidizing species cause oxidation and dissolution of the fuel matrix (UO<sub>2</sub>  $\rightarrow$  UO<sub>2+x</sub>) and concurrent oxidation of other redox-sensitive radionuclides (*e.g.*, Np<sup>4+</sup>  $\rightarrow$  Np<sup>5+</sup>). Matrix dissolution is enhanced by aqueous ligands (*e.g.*, HCO<sub>3</sub><sup>-</sup>), and the resulting actinide-complexes are mobile in the groundwater. However, aqueous uranyl-complexes are commonly immobilized via

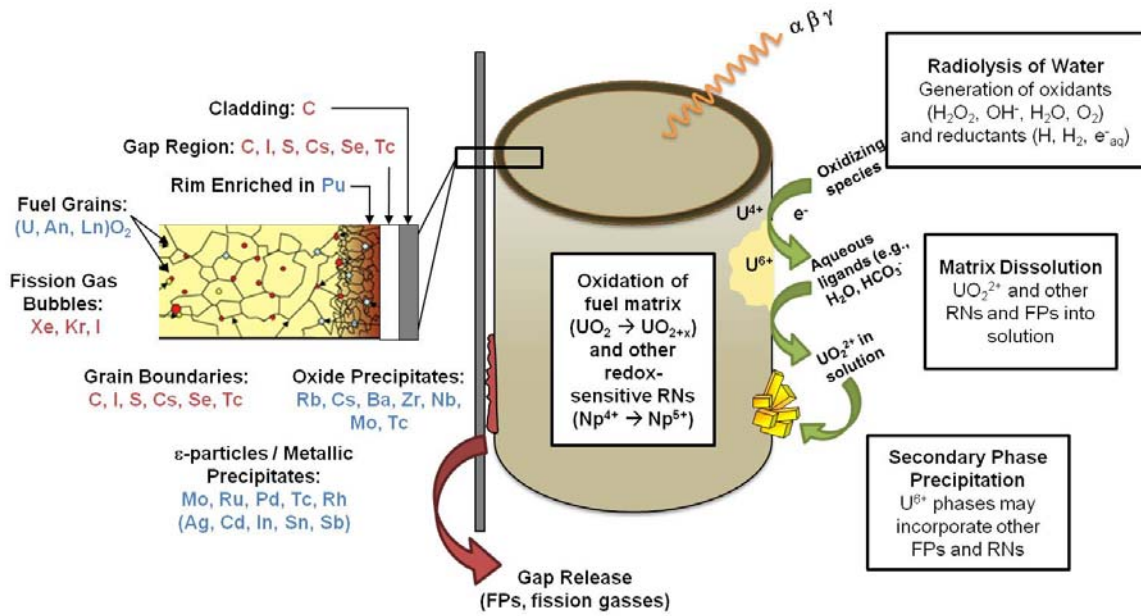


Figure 1.2. A schematic of UNF showing (left) where elements migrate during and after production in a nuclear reaction. The elements in red are instantaneously released when the UNF is in contact with water, while those in blue have slower release rates. (right) The processes that occur on or near the UNF surface when in contact with ground water in a geologic repository that cause the UNF to alter. Figure modified from (Bruno and Ewing, 2006).

precipitation as secondary phases. Uranium alteration phases are well documented at the natural reactors at Okelobondo, at uranium deposits (*e.g.*, Peña Blanca in Mexico), and as by-products of UNF corrosion studies (Finch and Murakami, 1999; Wronkiewicz et al., 1992; Wronkiewicz et al., 1996). The essential question is: **What happens to the long-lived radionuclides as the UO<sub>2</sub> alters to secondary U-phases?**

Just as uranyl minerals precipitate in oxidizing environments, other aqueous species may be immobilized via precipitation as alteration products. If the concentration of the aqueous species does not reach the solubility limit of a mineral phase, the aqueous complex may be immobilized by sorption onto a mineral surface, such as the (001) surface of hematite (Fe<sub>2</sub>O<sub>3</sub>). However, if the sorption substrates are colloidal mineral particles, mobility in the groundwater may actually be enhanced (Novikov et al., 2006; Utsunomiya et al., 2009). Finally, radionuclides may be incorporated into or co-precipitate with uranium alteration phases (Burns et al., 1997b).

A detailed understanding of the aqueous and solid-state geochemistry of the radionuclides is necessary to accurately evaluate their fate in the environment. Advances in the fields of actinide geochemistry and mineralogy have played, and will continue to play, a large role in enhancing scientists' understanding of the interactions between actinide species in aqueous environments, on mineral surfaces, and in solid solution with rock-forming minerals.

Basic actinide mineralogy has led the way for a comprehensive study on the crystal-chemistry (Burns, 2005; Burns et al., 1997a; Forbes et al., 2008), thermodynamics (Guillaumont et al., 2003; Helean et al., 2003; Kubatko et al., 2006) and kinetics (Gorman-Lewis et al., 2008; Shoesmith, 2000) of actinide-bearing materials. For

example, in the previous half century it was well accepted that uranium strongly partitioned between the 4+ and 6+ oxidation states, leaving the U<sup>5+</sup> inconsequential in oxidation models and the prediction of crystalline phases (Heal and Thomas, 1949). However, recent X-ray photoelectron spectroscopy (XPS) and computational modeling results indicate the presence of U<sup>5+</sup> during the reduction of U<sup>6+</sup> on magnetite nanoparticulates (Ilton et al., 2010). Thus, the fundamental concept of uranium redox processes includes a transition via U<sup>5+</sup>.

While U<sup>4+</sup>-minerals are limited primarily to uraninite ( $\text{UO}_{2+\chi}$ ) and coffinite ( $\text{USiO}_4$ ), the complexity of U<sup>6+</sup>-mineralogy warrants the use of a hierarchical classification system (Burns et al., 1997a). Ranging from clusters to sheets to framework structures, the structure and thermodynamic properties of U<sup>6+</sup>-phases, both natural and synthetic, have been widely studied over the past several decades to better understand the basic science of solid-state actinide chemistry, as well as to gain understanding on possible sources for uranium in the environment. The basic building block for U<sup>6+</sup> complexes and crystalline structures is the linear uranyl ion ( $\text{UO}_2^{2+}$ ), where the dioxo molecule is formed from a uranium atom strongly bound to two oxygen atoms. Similarly, neptunyl and plutonyl are also the basic building blocks of their respective aqueous actinyl complexes and crystalline phases (Forbes et al., 2008).

The ionic radii for 4+ Th, U, Np, and Pu with the same coordination are relatively similar. For example, the ionic radii for tetravalent actinides Th, U, Np, and Pu with coordination number (CN) 8 are 1.19, 1.14, 1.12, and 1.10 Å, respectively. In addition, the actinyl molecules for U, Np, and Pu have very similar geometries. The uranyl U<sup>6+</sup>-O bond length is 1.79 Å, while the neptunyl Np<sup>5+</sup>-O bond length is 1.84 Å (Burns et al.,

1997a; Forbes et al., 2008). Therefore, one might postulate that their solid-state chemistry is similar, and, in fact, the 4+ actinide oxides ( $\text{AnO}_2$ ) all have the cubic fluorite structure. However, the structural varieties are quite complex for the higher oxidation states, and the transuranium structures do not directly mimic the U-phases. For example, the  $\text{U}^{6+}$ -*silicate* boltwoodite has the  $\alpha$ -uranophane anion topology, while it is the  $\text{Np}^{5+}$ -*phosphate* that has the same anion topology (Note: Thus far, a  $\text{Np}^{6+}$ -silicate with the boltwoodite chemistry and crystallography has not been synthesized). In addition, mixed-oxidation state structures are more common for the transuranium structures than for uranium structures.

Quantum-mechanical calculations can be used to understand Np-phases on an electronic and atomic scale. While well-established in actinide quantum chemistry, the use of quantum-mechanical calculations is relatively new to the study of *solid-state* actinide chemistry. The ultimate goal of a computational study is to generate predictive results, thus careful comparison with experimental work at the early stages of computational simulation is essential in order to validate the theoretical model. Computational research is also used to test a theory or probe a material at a level beyond the capabilities of analytical techniques. Thus, calculations are meant to complement experiments – not only to repeat or confirm experimental findings, but actually provide insight into the experimental results. In terms of their predictive power, well established computational techniques can be used to guide experiments to save time and money.

This thesis is focused on understanding the thermodynamic stability of actinide containing materials using quantum-mechanical calculations and Monte-Carlo simulations. The specific aims of this dissertation are to:

- Understand the competition between the driving forces and hindrances for exsolution and/or ordering in solid solutions (**Chapter 2**);
- Determine the solid-solution behavior of binary dioxides with the fluorite structure (**Chapters 2 and 3**);
- Understand the impact of innate properties (*e.g.*, ionic radii, charge, electronic configuration) on the stability of solid solutions of actinides (**Chapters 2-5**);
- Evaluate possible incorporation mechanisms for the charge-balanced substitution of  $\text{Np}^{5+}$  for  $\text{U}^{6+}$  in uranyl minerals (**Chapters 4 and 5**).

The overarching scientific objective is to better understand the electronic behavior and crystal chemistry of actinide-containing materials via solid-solution calculations of actinide dioxides (*e.g.*,  $\text{Th}_x\text{U}_{1-x}\text{O}_2$ ) in which the thermodynamic mixing properties are calculated and phase diagrams are constructed (**Chapters 2 and 3**) and the determination of the electronic structure of uranyl phases (**Chapter 4**). The motivation for much of this work is to provide an understanding of actinide behavior that can be used in a safety assessment of a geologic repository, where the focus was primarily to understand natural mechanisms that immobilize actinide elements. Such mechanisms include the incorporation of Np into uranium alteration phases (**Chapters 4 and 5**).

My research has also included collaborations, where high pressure calculations were performed to support experimental measurements on coffinite ( $\text{USiO}_4$ ) phase transitions (Zhang et al., 2009), and with University of Notre Dame, where I have helped develop an experiment to complement my calculations in which the corrosion of Np-doped  $\text{UO}_2$  is observed. The corrosion experiment, which began almost two years ago, is ongoing. While the preliminary  $\text{UO}_2$  corrosion experiment revealed slight uranium alteration after

24 weeks, uranium alteration products have not been observed for the corrosion of Np-doped UO<sub>2</sub> pellets even after 64 weeks.

In **Chapters 2 and 3** quantum-mechanical calculations and Monte-Carlo simulations are used to calculate the thermodynamic mixing properties (*i.e.*, enthalpy, free energy, and configurational entropy) of oxide fuel materials, specifically Th<sub>x</sub>Me<sub>1-x</sub>O<sub>2</sub> and Me'<sub>x</sub>Zr<sub>1-x</sub>O<sub>2</sub> (Me = U, Ce; Me' = Th, Ce). Such oxide materials share the cubic fluorite structure. While ZrO<sub>2</sub> is typically monoclinic or tetragonal until extremely high  $T$ , a cubic structure can be stabilized (*e.g.*, Y-stabilized ZrO<sub>2</sub>). Phase diagrams are generated based on the free energy of mixing. The tendencies towards exsolution are evaluated based on the height of the peak of the  $\Delta G_{mix}$  curve above the tangent line connecting the minima of the curve. The competitive kinetic hindrances derived from the strain caused by the lattice mismatch at the lamellae interfaces are estimated and compared with the tendency towards exsolution in order to fully understand the thermodynamics of the oxide binaries. The solid-solution behavior of these materials impacts fuel fabrication, in-reactor performance, and the corrosion-resistance of the waste.

When UNF alters, aqueous actinide complexes are released from the waste. Incorporation of Np into uranium alteration phases may be a mechanism for immobilization of the aqueous actinides. Experimental corrosion studies of UO<sub>2</sub> and UNF have shown the precipitation of several hexavalent uranium phases including studtite [(UO<sub>2</sub>)O<sub>2</sub>(H<sub>2</sub>O)<sub>4</sub>] and boltwoodite [K(UO<sub>2</sub>)(SiO<sub>3</sub>OH)(H<sub>2</sub>O)<sub>1.5</sub>]. The objective of this computational study is to gain an atomistic understanding of the behavior of Np in a uranyl bonding environment, which will indicate favorable or unfavorable incorporation under repository conditions. Coupled-substitutions are necessary to substitute Np<sup>5+</sup> for

$\text{U}^{6+}$  in order to maintain charge neutrality. An addition of an  $\text{H}^+$  atom provides the charge-balance in  $\text{Np}^{5+}$ -incorporation into studtite. Boltwoodite has a more complex crystal structure. Therefore, the following coupled-substitutions for  $\text{Np}^{5+}$ -incorporation into boltwoodite include: *i*) addition of an  $\text{H}^+$  atom, *ii*) interlayer substitution (*i.e.*, divalent cation for  $\text{K}^+$ ), and *iii*) intra-layer substitution (*i.e.*,  $\text{P}^{5+}$  for  $\text{Si}^{4+}$ ). The energy required for the system to incorporate Np is calculated and the limit of Np incorporation for a specific charge-balancing mechanism is estimated. That is, for the intralayer substitution mechanism, the limit of  $\text{Np}^{5+}$ -incorporation into boltwoodite at 300 °C is about 585 ppm. These results are significant as they complement experimental work (*e.g.*, Burns and Klingensmith, 2006) and, with further calculations, can be used to interpret and extrapolate the results from laboratory experiments to predict Np-behavior under repository conditions.

The incorporation energy is calculated based on a stoichiometric reaction that describes the incorporation. For example,  $\text{Np}^{5+}$ -incorporation into studtite (*i.e.*,  $\text{Np}^{5+}$  and  $\text{H}^+$  substitution for  $\text{U}^{6+}$ ) is described by the following reaction:  $2[\text{UO}_2\text{O}_2(\text{H}_2\text{O})_4] + \frac{1}{2}\text{Np}_2\text{O}_5 + \frac{1}{2}\text{H}_2\text{O} \rightarrow (\text{NpOOH})(\text{UO}_2)(\text{O}_2)_2(\text{H}_2\text{O})_8 + \text{UO}_3$ . The incorporation energy is the difference of the sum of the total energy of the products minus that of the reactants. Quantum-mechanical geometry optimizations are performed for not only studtite and Np-substituted studtite, but also the reference phases (*e.g.*,  $\text{Np}_2\text{O}_5$ ).  $\text{Np}^{5+}$  has 2 unpaired 5f electrons; therefore, the spin configuration is important for obtaining the lowest energy structure. My results indicate that the anti-ferromagnetic spin configuration is favorable, which is in agreement with experimental results (Forbes et al., 2007), and provides insight into magnetic spin ordering.

## References

- Allen, T.R., Busby, J.T., Klueh, R.L., Maloy, S.A., and Toloczko, M.B. (2008) Cladding and duct materials for advanced nuclear recycle reactors. *JOM*, 60(1), 15-23.
- Amme, M. (2002) Contrary effects of the water radiolysis product H<sub>2</sub>O<sub>2</sub> upon the dissolution of nuclear fuel in natural ground water and deionized water. *Radiochimica Acta*, 90(7), 399-406.
- Bruno, J., and Ewing, R.C. (2006) Spent nuclear fuel. *Elements*, 2(6), 343-349.
- Burns, P.C. (2005) U<sup>6+</sup> minerals and inorganic compounds: Insights into an expanded structural hierarchy of crystal structures. *Canadian Mineralogist*, 43, 1839-1894.
- Burns, P.C., Ewing, R.C., and Hawthorne, F.C. (1997a) The crystal chemistry of hexavalent uranium: Polyhedron geometries, bond-valence parameters, and polymerization of polyhedra. *Canadian Mineralogist*, 35, 1551-1570.
- Burns, P.C., Ewing, R.C., and Miller, M.L. (1997b) Incorporation mechanisms of actinide elements into the structures of U<sup>6+</sup> phases formed during the oxidation of spent nuclear fuel. *Journal of Nuclear Materials*, 245(1), 1-9.
- Burns, P.C., and Klingensmith, A.L. (2006) Uranium mineralogy and neptunium mobility. *Elements*, 2(6), 351-356.
- Demkowicz, P.A., Jerden, J.L., Cunnane, J.C., Shibuya, N., Baney, R., and Tulenko, J. (2004) Aqueous dissolution of urania-thoria nuclear fuel. *Nuclear Technology*, 147(1), 157-170.
- Donald, I.W., Metcalfe, B.L., and Taylor, R.N.J. (1997) The immobilization of high level radioactive wastes using ceramics and glasses. *Journal of Materials Science*, 32(22), 5851-5887.
- Ewing, R.C. (2006) The nuclear fuel cycle: A role for mineralogy and geochemistry. *Elements*, 2(6), 331-334.
- Ewing, R.C., Weber, W.J., and Lian, J. (2004) Nuclear waste disposal-pyrochlore (A<sub>2</sub>B<sub>2</sub>O<sub>7</sub>): Nuclear waste form for the immobilization of plutonium and "minor" actinides. *Journal of Applied Physics*, 95(11), 5949-5971.

- Finch, R., and Murakami, T. (1999) Systematics and paragenesis of uranium minerals. In P.C. Burns, and R. Finch, Eds. Uranium: Mineralogy, Geochemistry, and the Environment, 38, p. 91-179.
- Forbes, T.Z., Burns, P.C., Skanthakumar, S., and Soderholm, L. (2007) Synthesis, structure, and magnetism of  $\text{Np}_2\text{O}_5$ . *Journal of the American Chemical Society*, 129(10), 2760.
- Forbes, T.Z., Wallace, C., and Burns, P.C. (2008) Neptunyl compounds: Polyhedron geometries, bond-valence parameters, and structural hierarchy. *The Canadian Mineralogist*, 46(6), 1623-1645.
- Gorman-Lewis, D., Burns, P.C., and Fein, J.B. (2008) Review of uranyl mineral solubility measurements. *Journal of Chemical Thermodynamics*, 40(3), 335-352.
- Guerin, Y., Was, G.S., and Zinkle, S.J. (2009) Materials challenges for advanced nuclear energy systems. *MRS Bulletin*, 34(1), 10-14.
- Guillaumont, D., Fanghanel, J., Fuger, J., Grenthe, I., Neck, V., Palmer, D.A., and Rand, M.H. (2003) Update on Chemical Thermodynamics of Uranium, Neptunium, Plutonium, Americium, and Technetium. Elsevier, Amsterdam.
- Heal, H.G., and Thomas, J.G.N. (1949) Unstable ions of quinquivalent uranium. *Transactions of the Faraday Society*, 45(1), 11-20.
- Helean, K.B., Navrotsky, A., Lumpkin, G.R., Colella, M., Lian, J., Ewing, R.C., Ebbinghaus, B., and Catalano, J.G. (2003) Enthalpies of formation of U-, Th-, Ce-brannerite: implications for plutonium immobilization. *Journal of Nuclear Materials*, 320(3), 231-244.
- Ilton, E.S., Boily, J.F., Buck, E.C., Skomurski, F.N., Rosso, K.M., Cahill, C.L., Bargar, J.R., and Felmy, A.R. (2010) Influence of dynamical conditions on the reduction of U-VI at the magnetite-solution interface. *Environmental Science & Technology*, 44(1), 170-176.
- Kubatko, K.A., Helean, K., Navrotsky, A., and Burns, P.C. (2006) Thermodynamics of uranyl minerals: Enthalpies of formation of uranyl oxide hydrates. *American Mineralogist*, 91(4), 658-666.

- Lutze, W., and Ewing, R.C. (1988) Radioactive waste forms for the future. 778 p. North-Holland, Amsterdam.
- Novikov, A.P., Kalmykov, S.N., Utsunomiya, S., Ewing, R.C., Horreard, F., Merkulov, A., Clark, S.B., Tkachev, V.V., and Myasoedov, B.F. (2006) Colloid transport of plutonium in the far-field of the Mayak Production Association, Russia. *Science*, 314(5799), 638-641.
- Shoesmith, D.W. (2000) Fuel corrosion processes under waste disposal conditions. *Journal of Nuclear Materials*, 282(1), 1-31.
- Skomurski, F.N., Shuller, L.C., Ewing, R.C., and Becker, U. (2008) Corrosion of  $\text{UO}_2$  and  $\text{ThO}_2$ : A quantum-mechanical investigation. *Journal of Nuclear Materials*, 375(3), 290-310.
- Utsunomiya, S., Kersting, A.B., and Ewing, R.C. (2009) Groundwater nanoparticles in the far-field at the Nevada Test Site: Mechanism for radionuclide transport. *Environmental Science & Technology*, 43(5), 1293-1298.
- Wang, S.A., Alekseev, E.V., Juan, D.W., Casey, W.H., Phillips, B.L., Depmeier, W., and Albrecht-Schmitt, T.E. (2010) NDTB-1: A supertetrahedral cationic framework that removes  $\text{TcO}_4^-$  from solution. *Angewandte Chemie-International Edition*, 49(6), 1057-1060.
- Wronkiewicz, D.J., Bates, J.K., Gerding, T.J., Veleckis, E., and Tani, B.S. (1992) Uranium release and secondary phase formation during unsaturated testing of  $\text{UO}_2$  at 90 degrees C. *Journal of Nuclear Materials*, 190, 107-127.
- Wronkiewicz, D.J., Bates, J.K., Wolf, S.F., and Buck, E.C. (1996) Ten-year results from unsaturated drip tests with  $\text{UO}_2$  at 90 degrees C: Implications for the corrosion of spent nuclear fuel. *Journal of Nuclear Materials*, 238(1), 78-95.
- Zhang, F.X., Pointeau, V., Shuller, L.C., Reaman, D.M., Lang, M., Liu, Z.X., Hu, J.Z., Panero, W.R., Becker, U., Poinsot, C., and Ewing, R.C. (2009) Structural transitions and electron transfer in coffinite,  $\text{USiO}_4$ , at high pressure. *American Mineralogist*, 94(7), 916-920.
- Zinkle, S.J., and Busby, J.T. (2009) Structural materials for fission & fusion energy. *Materials Today*, 12(11), 12-19.

## **Publications and abstracts resulting from this dissertation**

### ***Publications***

- Shuller, L.C., Ewing, R.C., and Becker, U. (2010) Quantum-mechanical evaluation of Np-incorporation into studtite. *American Mineralogist*, 95, 1151-1160.
- Shuller, L.C., Ewing, R.C., and Becker, U. Thermodynamic properties of  $\text{Th}_x\text{U}_{1-x}\text{O}_2$  ( $0 < x < 1$ ) based on quantum-mechanical calculations and Monte-Carlo simulations (submitted to *Journal of Nuclear Materials*).
- Shuller, L.C., Ewing, R.C., and Becker, U. A quantum-mechanical approach for the evaluation of Np-incorporation into uranyl phases (submitted to *Journal of Nuclear Materials Special Issue: Spent Nuclear Fuel*).
- Shuller, L.C., Ewing, R.C., and Becker, U. (2010) Atomistic calculations of the thermodynamic properties of mixing for dioxide solid solutions containing tetravalent cations with unoccupied f orbitals (in preparation for *Journal of Nuclear Materials*).

### ***Proceedings***

- Shuller, L.C., Pavenayotin, N., Ewing, R.C., and Becker, U. (2009) Thermodynamic properties of actinide dioxide solid solutions. *Materials Research Society Conference Proceedings*, 1125: R10-06.
- Shuller, L.C., Pavenayotin, N., Skomurski, F.N., Ewing, R.C., and Becker, U. (2008) Thermodynamic properties of actinide-zirconium dioxide solid-solutions relevant for advanced nuclear fuels. *Waste Management 2008 Conference Proceedings*, 8438.
- Shuller, L.C., Ewing R.C., and Becker U. (2008) Np incorporation into K-boltwoodite. *Materials Research Society Conference Proceedings*, 1107: 455-463.
- Shuller, L.C., Ewing R.C., and Becker U. (2007) Np incorporation into uranyl alteration phases: A quantum mechanical approach. *Materials Research Society Conference Proceedings*, 985: 407-412

### ***Presentations***

- Shuller, L.C., Ewing, R.C., and Becker, U. (2010) Quantum-mechanical evaluation of Np-incorporation into studtite. American Nuclear Society, Las Vegas, NV (1st place in Department of Energy's Innovations in Fuel Cycle Research student paper competition).
- Shuller, L.C., Ewing, R.C., and Becker, U. (2009) ECI Integrated Waste Forms for Future Fuel Cycles, Charleston, SC (Best student poster).
- Shuller, L.C., Ewing, R.C., and Becker, U. (2009) Computational investigation of the thermodynamic mixing properties of actinide dioxide solid solutions. Materials Science and Technology, Pittsburgh, PA.
- Shuller, L.C., Ewing, R.C., and Becker, U. (2008) Thermodynamic properties of actinide oxide solid solutions. Materials Research Society, Boston, MA.
- Shuller, L.C., Pavenayotin, N., Skomurski, F.N., Ewing, R.C., and Becker, U. (2008) Thermodynamic properties of actinide-zirconium dioxide solid-solutions relevant for advanced nuclear fuels. Waste Management Conference, Phoenix, AZ (Best poster in session).
- Shuller, L.C., Ewing, R.C., and Becker, U. (2007) Np incorporation into K-boltwoodite. Materials Research Society, Sheffield, England.
- Shuller, L.C., Ewing, R.C., and Becker, U. (2007) Computational investigation of Np incorporation into K-boltwoodite. American Chemical Society, Chicago, IL.
- Shuller L.C., Ewing R.C., and Becker U. (2006) Np-incorporation into uranyl phases: A quantum-mechanical approach. Materials Research Society, Boston, MA.
- Shuller, L.C., Ewing, R.C., Becker, U. (2006) Np<sup>5+</sup> incorporation into uranyl alteration phases: a quantum mechanical approach. AGU, 87(36), Jt. Assem. Suppl., Abstract M21A-05. (Poster)

## **Publications and abstracts resulting from side-projects**

### ***Publications***

- Zhang, F., Pointeau, V., Shuller, L.C., Reaman, D., Lang, M., Liu, Z., Hu, J., Panero, W., Becker, U., Ewing, R. (2009) Structural transitions and electron transfer in coiffinite,  $\text{USiO}_4$ , at high pressure. *American Mineralogist*, 94(7): 916-920.
- Skomurski, F.N., Shuller, L.C., Ewing, R.C., and Becker U. (2008) Corrosion of  $\text{UO}_2$  and  $\text{ThO}_2$ : A quantum-mechanical investigation. *Journal of Nuclear Materials*, 375(3): 290-310.

### ***Proceedings***

- Pinder-Grover, T., Millunchick, J.M., Bierwert, C., and Shuller, L. (2009) Leveraging Screencasts to Strategically Clarify Unclear Materials Science Concepts. American Society of Engineering Education.
- Pinder-Grover, T., Millunchick, J.M., Bierwert, C., and Shuller, L. (2009) The Efficacy of Screencasts on Diverse Students in a Large Lecture Course. American Society of Engineering Education.

### ***Presentations***

- Hastings, P.T. Jr., Krall, L., Shuller, L.C., Zhang, J.M., and Ewing, R.C. (2010) Fen Complex carbonates, Telemark, Norway: Mineralogy of niobium and thorium bearing minerals. *Geochemical Society of America*, Denver, CO. (Poster)
- Shuller, L.C., Poling, J., Ewing, R.C., and Becker, U. (2009) Quantum-mechanical calculations of aqueous actinide adsorption onto hematite (001). *Radionuclide Migration*, Kennewick, WA. (Poster)
- Shuller, L.C., Poling, J., Ewing, R.C., and Becker, U. (2008) Actinide adsorption onto hematite (001) surface. *Geochimica et Cosmochimica Acta*, 72(12): A864-A864.
- Pinder-Grover, T., Millunchick, J.M., Bierwert, C., and Shuller, L. (2009) Leveraging Screencasts to Strategically Clarify Unclear Materials Science Concepts. American Society of Engineering Education, Austin, TX.

- Pinder-Grover, T., Millunchick, J.M., Bierwert, C., and Shuller, L. (2009) The Efficacy of Screencasts on Diverse Students in a Large Lecture Course. American Society of Engineering Education, Austin, TX.
- Skomurski, F.N., Shuller, L.C., Ewing, R.C., and Becker U. (2006) Adsorption energy trends on  $\text{UO}_2$  and  $\text{ThO}_2$  surfaces. Eos Trans., AGU, 87(36), Jt. Assem. Suppl., Abstract M33A-04.
- Skomurski, F.N., Shuller, L., Ewing, R.C., and Becker, U. (2006) The surface-water interface: where spectroscopy meets atomic-scale modeling. Workshop on In-Situ Characterization of Surface and Interface Structures and Processes, Argonne, IL.
- Skomurski, F.N., Shuller, L., Ewing, R.C., and Becker, U. (2005) The corrosion of  $\text{UO}_2$  versus  $\text{ThO}_2$ : a quantum mechanical investigation. Geochimica et Cosmochimica Acta, 69(10): A411-A411.

## **Chapter 2**

# **Thermodynamic properties of $\text{Th}_x\text{U}_{1-x}\text{O}_2$ ( $0 < x < 1$ ) based on quantum-mechanical calculations and Monte-Carlo simulations**

### **Abstract**

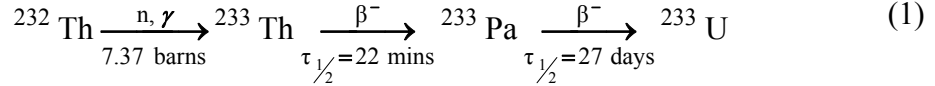
$\text{Th}_x\text{U}_{1-x}\text{O}_2$  ( $0 < x < 1$ ) binary compositions occur in nature, uranothorianite, and as a mixed oxide nuclear fuel. As a nuclear fuel, important properties, such as the melting point, thermal conductivity, and the thermal expansion coefficient change as a function of composition. Additionally, for direct disposal of  $\text{Th}_x\text{U}_{1-x}\text{O}_2$ , the chemical durability changes as a function of composition, with the dissolution rate decreasing with increasing thoria content.  $\text{UO}_2$  and  $\text{ThO}_2$  have the same isometric structure, and the ionic radii of octahedrally coordinated  $\text{U}^{4+}$  and  $\text{Th}^{4+}$  are similar (1.14 nm and 1.19 nm, respectively). Thus, this binary is expected to form a complete solid solution. However, atomic-scale measurements or simulations of cation ordering and the associated thermodynamic properties of the  $\text{Th}_x\text{U}_{1-x}\text{O}_2$  system have yet to be determined. A combination of density-functional theory, Monte-Carlo methods, and thermodynamic integration are used to calculate thermodynamic properties of the  $\text{Th}_x\text{U}_{1-x}\text{O}_2$  binary ( $\Delta H_{mix}$ ,  $\Delta G_{mix}$ ,  $\Delta S_{mix}$ , phase

diagram). The Gibbs free energy of mixing ( $\Delta G_{mix}$ ) indicates a small tendency for the system to exsolve at equilibration temperatures below 1000 K (e.g.,  $E_{exsoln} = 0.13 \text{ kJ}/(\text{mol cations})$  at 750 K). However, the energy gain by exsolution may not overcome the increase in interface energy between exsolution lamellae ( $E_{IF} = 0.4 \text{ kJ}/(\text{mol cations})$ ) for an exsolution lamellae thickness of 10.2 Å, unless the lamellae reach a thickness of 45.9 Å. Monte-Carlo simulations converge to an exsolved structure [lamellae  $\parallel (21\bar{1})$ ] only for very low equilibration temperatures (below room temperature). In addition to the weak tendency to exsolve, there is an ordered arrangement of Th and U in the solid solution [alternating U and Th layers  $\parallel \{100\}$ ] that is energetically favored for the homogeneously mixed 50% Th configurations. Still, this tendency to order is so weak that ordering is seldom reached. The excess configurational entropy ( $\Delta S_{mix}$ ) is approximately equal to the point entropy at all temperatures, indicating that the system is not ordered.

## Introduction

Thorium and uranium are the two heaviest naturally-occurring elements, and both are utilized in nuclear fuels. While 0.7% of naturally-occurring uranium is the fissile  $^{235}\text{U}$  isotope, thorium only occurs as the fertile  $^{232}\text{Th}$  isotope. However,  $^{232}\text{Th}$  can be converted to  $^{233}\text{U}$ , which can be bred in both thermal and fast neutron reactors, because the value of  $\eta$  (*i.e.*, the mean number of fission neutrons produced per thermal neutron) is greater than 2.0 over a wide range of the thermal neutron spectrum (IAEA, 2005). The  $^{232}\text{Th}$  to  $^{233}\text{U}$  conversion occurs via the neutron absorption and subsequent  $\beta$ -decays in

Reaction 1. Either fissile  $^{235}\text{U}$  or  $^{239}\text{Pu}$  is needed in Th-fuels to initiate the fission required to convert fertile  $^{232}\text{Th}$  to fissile  $^{233}\text{U}$ .



There has been renewed interest in Th-based fuels because of advantages related to proliferation resistance (Herring et al., 2001; IAEA, 2005; MacDonald and Lee, 2004) and enhanced in-reactor performance (Kurina et al., 2002; Kutty et al., 2008; Murabaya et al., 1969; Takahashi and Murabayashi, 1975; Tyagi et al., 2004). In addition, Th-based fuels have a higher chemical durability, as thorium only exists in its 4+ oxidation state, whereas uranium exists primarily in the 4+ and 6+ oxidation states. Due to the presence of two unpaired electrons for  $\text{U}^{4+}$ ,  $\text{UO}_2$  is easily oxidized in the presence of water and oxygen to a wide variety of U(VI)-compounds (Skomurski et al., 2008). Aqueous dissolution of  $\text{UO}_2$  is significantly decreased when doped with Th (Demkowicz et al., 2004). Thus, the addition of  $\text{ThO}_2$  improves the chemical durability of oxide fuels in a geologic repository.

Naturally-occurring isometric thorianite,  $\text{ThO}_2$ , is isostructural with uraninite,  $\text{UO}_{2+x}$ . Unit cell parameters change almost linearly according to Vegard's law with changing composition, which has lead most to conclude that this binary forms a complete solid solution (Hazen et al., 2009; Robinson and Sabina, 1955). However, mixed Th-U oxides, uranothorianite, may be exsolved at the nanoscale (Becker et al., 2006; McEnroe et al., 2002). The same type of nano-scale exsolution and/or cation ordering of mixed-Th-U nuclear fuels may affect important properties, such as thermal conductivity, the thermal expansion coefficient, and the melting point of such a solid solution. Thus, in addition to

knowledge of the thermophysical and thermodynamic properties of polycrystalline Th-based fuels, an understanding of cation ordering of mixed oxide fuels is essential to fully understand the in-reactor behavior of the fuel. Quantum-mechanical calculations and Monte-Carlo simulations of the complete  $\text{Th}_x\text{U}_{1-x}\text{O}_2$  solid-solution binary have been used to calculate the enthalpy of mixing ( $\Delta H_{mix}$ ). Subsequent thermodynamic integration was applied to derive the Gibbs free energy ( $\Delta G_{mix}$ ) and configurational entropy ( $\Delta S_{mix}$ ) of mixing. The Gibbs free energy of mixing ( $\Delta G_{mix}$ ) is used to generate a binary temperature-composition phase diagram for  $\text{Th}_x\text{U}_{1-x}\text{O}_2$ , and atomic-scale cation ordering is evaluated.

## Methodology

Three consecutive computational methods were used to determine the solid-solution thermodynamic properties of  $\text{Th}_x\text{U}_{1-x}\text{O}_2$ : 1) quantum-mechanical geometry optimizations, 2) Monte-Carlo simulations, and 3) thermodynamic integration. The quantum-mechanical calculations were conducted in order to determine the optimized geometry of the end-members (*i.e.*,  $\text{ThO}_2$ ,  $\text{UO}_2$ ), as well as intermediate compositions (*e.g.*,  $\text{Th}_x\text{U}_{1-x}\text{O}_2$ , where  $0 < x < 1$ ). The enthalpy of mixing was calculated from the quantum-mechanical results. The final energies from the quantum-mechanical calculations are then used to calculate cation-cation interaction parameters for all possible pairs of exchangeable cations. For instance, in the  $\text{Th}_x\text{U}_{1-x}\text{O}_2$  series, interaction parameters are calculated for Th-U, Th-Th, and U-U for first-, second-, third-, and fifth-nearest neighbor interactions. The interaction parameters are then used in the Monte-Carlo simulation to calculate temperature-dependent thermodynamic properties of the solid-solution series.

Using a Monte-Carlo approach allows one to evaluate millions of configurations for different compositions in much larger supercells than is possible using quantum-mechanical calculations.

### ***Quantum-mechanical calculations***

The program CASTEP (CAmbridge Serial Total Energy Package; Payne et al., 1992; Segall et al., 2002) was used for the ground state total energy calculations. CASTEP is a density functional theory-based code that uses plane waves as the basis function and pseudo-potentials to approximate the behavior of the core electrons. Ultra-soft pseudopotentials were used to approximate the role of the core and inner valence electrons (Vanderbilt, 1990). Outer valence electrons ( $\text{U } 5\text{f}^3 6\text{s}^2 6\text{p}^6 6\text{d}^1 7\text{s}^2$ ,  $\text{Th } 6\text{s}^2 6\text{p}^6 6\text{d}^2 7\text{s}^2$ , and  $\text{O } 2\text{s}^2 2\text{p}^4$ ) are treated explicitly in the Hamiltonian of the Schrödinger equation. The spin-polarized generalized gradient approximation (GGA) with the PW-91 (Perdew and Wang, 1992) functional was used to approximate the electron exchange and correlation energies. GGA has shown greater structural agreement for  $\text{UO}_2$  geometry optimizations than localized density approximation (LDA) (Skomurski et al., 2006). The kinetic energy cut-off for the planewaves was 800 eV and the k-point spacing was  $0.1 \text{ \AA}^{-1}$ , which results in 9 k-points for the  $2 \times 1 \times 1$  unit cell without symmetry. The total energy convergence tolerance was  $1 \cdot 10^{-5} \text{ eV/atom}$ . Geometry optimizations were performed without symmetry constraints (*i.e.*, PI), and the starting lattice parameters for the intermediate structures were weighted averages of the end-member unit cell parameters. A spin-polarized approach was used for unit cells containing U to take into account the behavior of the two unpaired 5f electrons in the 4+ oxidation state.

Both binary oxides have the cubic fluorite structure, and each unit cell contains four formula units ( $Z = 4$ ). The cation occupies every other cube formed by the oxygen sublattice (Figure 2.1), resulting in four possible exchangeable cation sites for a  $1 \times 1 \times 1$  unit cell and eight exchangeable cation sites for a  $2 \times 1 \times 1$  unit cell. The four exchangeable cations of a unit cell are equidistant from each other, forming a tetrahedral coordination polyhedron around the oxygen.

### ***Generating interaction parameters***

The total energy as calculated by CASTEP is the formation energy from the zero valent gaseous species. The enthalpy of mixing from the quantum-mechanical calculations is determined as the difference between the total energy with some concentration  $x$  of Th in  $\text{UO}_2$  and a linear combination of the total energies of the end-members (Equation 2). The quantum-mechanical calculations are ground-state (0 K) calculations; therefore, the enthalpy of mixing is considered to be an energy of mixing ( $\Delta E_{\text{mix}}$ ). The energy of mixing of Th into  $\text{UO}_2$  can also be described by a Hamiltonian that takes into account the interactions between the cations, *i.e.*, the Th-Th, U-U, and Th-U interactions (Equation 3).

$$\Delta E_{\text{mix}}^{\text{CASTEP}} = E(\text{Th}_x \text{U}_{1-x} \text{O}_2) - [x E(\text{ThO}_2) + (1 - x) E(\text{UO}_2)] \quad (2)$$

$$\Delta E_{\text{mix}}^{\text{fit}} = E_0 + \sum_i (n^i_{\text{Th-U}} E^i_{\text{Th-U}} + n^i_{\text{Th-Th}} E^i_{\text{Th-Th}} + n^i_{\text{U-U}} E^i_{\text{U-U}}) \quad (3)$$

In Equation 3,  $i$  is the type of interaction as identified by the distance of the cation interaction (*i.e.*, next-, second-, third-nearest neighbor interaction),  $n^i$  is the number of iterations of a type  $i$  in a given cell configuration (*e.g.*,  $n^1_{\text{Th-U}}$  would be the number of first nearest-neighbor Th-U interactions), and  $E^i$  is the excess energy contribution associated

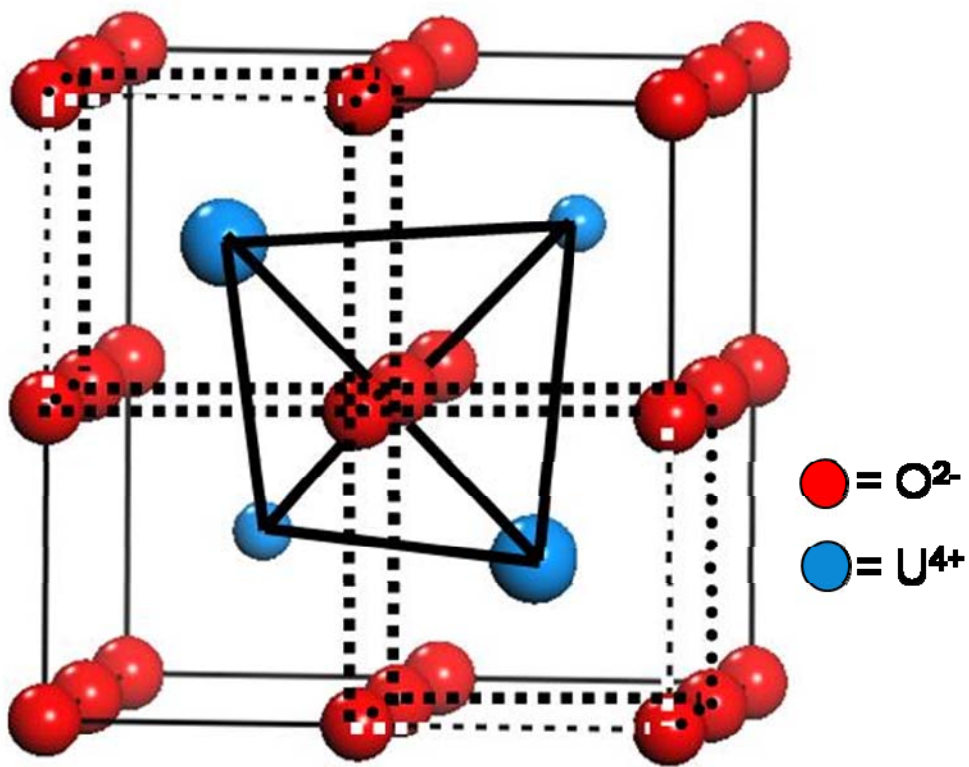


Figure 2.1. Uraninite ( $\text{UO}_{2+x}$ ) and thorianite ( $\text{ThO}_2$ ) have the fluorite crystal structure, where the cations are octahedrally coordinated and occupy every other cube generated by the oxygen sublattice. The larger atoms in this figure represent the cation in the foremost oxygen cube and the smaller atoms occupy the cubes into the page.

with a given cation-cation pair. The asymmetry of the system and the overall shape of a randomly ordered sub-regular solid solution are approximated by a Margules function (Equation 4). Later calculations are concerned with excess properties, so the interaction energies from Equation 3 ( $E^i$ ) are combined into an exchange parameter  $J^i$ , which describes the energy associated with the Th-U cation exchange (Equation 5).

$$E_0 = x(1-x)[W_1x + W_2(1-x)] \quad (4)$$

$$J^i_{Th-U} = E^i_{Th-U} - \frac{1}{2}(E^i_{Th-Th} + E^i_{U-U}) \quad (5)$$

The interaction parameters  $J^i_{Th-U}$  and the Margules parameters  $W_1$  and  $W_2$  are fit to the quantum-mechanically determined energy of mixing according to Equation 6. The interaction parameters for the solid-solution series and Margules parameters are listed in Table 2.1.

$$E_{excess} = E_0 + \sum n^i_{Th-U} J^i_{Th-U} \quad (6)$$

The quality of fit for the interaction parameters is evaluated by comparing the fit using different numbers of configurations and compositions across the  $\text{Th}_x\text{U}_{1-x}\text{O}_2$  binary. Two fit scenarios are compared in Table 2.1. For a  $1\times1\times1$  unit cell, the only type of cation-cation interaction, as identified by the distance between two cations, is the first nearest-neighbor interaction because all cations are at an equal distance  $r$  from each other ( $r = 3.86 \text{ \AA}$ ). Due to the computational expense of the quantum-mechanical calculations, the expansion of the unit cell was limited to  $2\times1\times1$ . This unit cell expansion improved the fit for the exchange parameters, and increasing the number of configurations adds more energetic information on longer-range interactions. The types of cation-cation interactions increased from only first nearest-neighbor interactions to the inclusion of

Table 2.1. Margules and interaction parameters fit for  $1\times1\times1$  unit cells and  $2\times1\times1$  unit cells.

Parameter	Cation-cation distance (Å)	$1\times1\times1$	$2\times1\times1$
$W_1$ (kJ/mol exchangeable cations)		25.1	15.2
$W_2$ (kJ/mol exchangeable cations)		7.4	2.8
$J_1$ (J/mol Th-U interactions)	3.86	-3.0	24.0
$J_2$ (J/mol Th-U interactions)	5.48	N/A	24.0
$J_3$ (J/mol Th-U interactions)	6.69	N/A	-2.0
$J_4$ (J/mol Th-U interactions)	7.72	N/A	linearly dependent → N/A
$J_5$ (J/mol Th-U interactions)	8.65	N/A	-18.0
<i>Correlation coefficient</i>		0.926	0.960

fifth nearest-neighbor interactions.  $J_{1-3}$  represent the first, second, and third nearest neighbor interactions ( $r_1 = 3.86 \text{ \AA}$ ,  $r_2 = 5.48 \text{ \AA}$ ,  $r_3 = 6.69 \text{ \AA}$ ), and  $J_5$  represents the fifth nearest neighbor interactions ( $r_5 = 8.65 \text{ \AA}$ ). The forth nearest-neighbor interaction does not improve the fit because this parameter is linearly dependent on the first nearest-neighbor interaction. The absolute value of the first and fifth nearest-neighbor interaction parameters are about equal but opposite in sign (*i.e.*, if the system tends to have more nearest-neighbor U-Th interactions, homocationic U-U and Th-Th fifth nearest-neighbor interactions would be favored and *vice versa*). The  $2\times 1\times 1$  fit was used for the Monte-Carlo simulations to include the most information about the energetics of the Th-U system.

### ***Monte-Carlo simulations***

The exchange parameters,  $J_i$ , are used in the Monte-Carlo simulations to calculate the lattice energy for millions of different cation configurations. The excess enthalpy of mixing is calculated for the solid-solution series using the methodology previously described (Ferriss et al., 2008; Ferriss et al., 2010; Reich and Becker, 2006). An energy  $E$  is associated with each starting configuration, and the energy change associated with swapping cation positions is  $\Delta E$ . If  $\Delta E$  is negative, meaning that the new configuration is more energetically favored than the previous configuration, the new configuration is accepted. If  $\Delta E$  is positive, then the new configuration is accepted with a probability following a Boltzmann distribution. In practice, the swap is accepted if  $\exp(-\Delta E/kT)$  is greater than a random number between 0 and 1. An  $8\times 8\times 8$  supercell of the conventional unit cell was constructed for the Monte-Carlo simulations, resulting in 2048

exchangeable cation sites. The excess entropy and free energy of mixing are then calculated using the Bogoliubov integration scheme (Ferriss et al., 2010; Myers, 1998; Yeomans, 1992).

### **Structure analysis of quantum-mechanical calculations**

The unit cell parameter and  $\langle \text{Me-O} \rangle$  ( $\text{Me} = \text{U}, \text{Th}$ ) bond lengths are compared to extended X-ray adsorption fine structure (EXAFS) and X-ray diffraction (XRD) measurements in order to validate the quantum-mechanical calculations. The relationship between the  $\text{Th}_x\text{U}_{1-x}\text{O}_2$  unit cell parameter and concentration of Th, where  $0 < x < 1$ , follows Vegard's law (Figure 2.2); that is, the deviation of the lattice parameters from a line connecting uraninite and thorianite is less than the scatter of the experimental and the calculated values for different configurations. The calculated unit cell parameter for the end-members (Table 2.2) are within  $\pm 0.3\%$  of the experimental values, where the  $\text{UO}_2$  end-member is calculated to be 0.3% larger, and the  $\text{ThO}_2$  end-member is calculated to be 0.3% smaller than the experimental unit cell measurements (Hubert et al., 2006). The shorter  $\langle \text{Th-O} \rangle$  distances are expected according to the findings that DFT-GGA calculations typically result in smaller lattice parameters and shorter bond lengths. The longer  $\langle \text{U-O} \rangle$  distances may be attributed to the commonly reported errors of DFT calculations on highly correlated 5f electrons ( $\text{U}^{4+}$  contains two). However, the reported lattice parameters for  $\text{UO}_2$  range from 5.468 to 5.471 Å (Hubert et al., 2006; Wyckoff, 1963).

The  $\langle \text{Me-O} \rangle$  bond lengths for the first-shell distances and  $\langle \text{Me-Me} \rangle$  bond lengths for the second-shell distances are compared to experimental EXAFS results, which show that

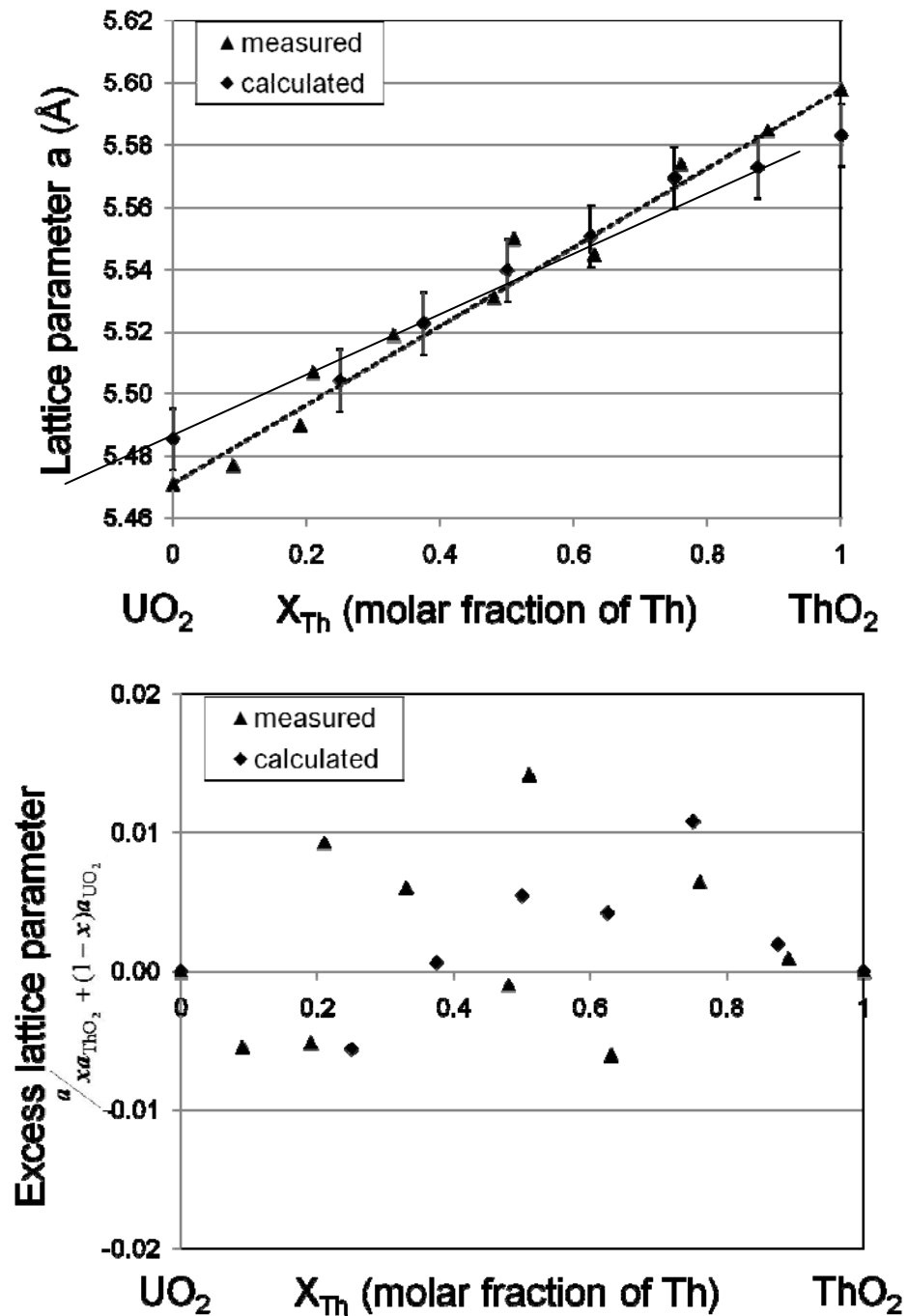


Figure 2.2. (a) The weighted average of the quantum-mechanical calculations and experimental measurements (Hubert et al., 2006) lattice parameter *versus* concentration results are in agreement with Vegard's law (solid line based on experimental results) within  $\sim 0.3\% (\pm 0.015 \text{ \AA})$  based on (b) the plot of the excess values with respect to the end-member lattice parameters.

Table 2.2. Comparison of calculated unit cell length with measured values.

Structure	Calculated	Measured	Difference
ThO <sub>2</sub>	5.583 Å	5.598 Å	-0.3%
UO <sub>2</sub>	5.487 Å	5.471 Å	0.3%

the first-shell  $\langle \text{Me-O} \rangle$  distances vary slightly across the solid solution range; however, second-shell  $\langle \text{Me-Me} \rangle$  distances vary significantly with composition (Hubert et al., 2006). Similar results are observed for the calculated  $\langle \text{Me-O} \rangle$  and  $\langle \text{Me-Me} \rangle$  distances (Table 2.3). After correcting the bond lengths based on the 0.3% mismatch in the lattice parameter, the bond length as a function of Th concentration has no specific trend in excess bond length based on a linear combination of the end-members (Figure 2.3).

### **Thermodynamic properties of mixing**

The enthalpy of mixing is positive at all temperatures, indicating that this is not an ideal solid-solution, which is a first indication that some unmixing may occur (Figure 2.4a). The absolute values of the maxima of the enthalpy of mixing, however, are relatively small, only about 3 kJ/(mol exchangeable cations) at 1000 K. For comparison, the maximum enthalpy of mixing at 1000 K for the  $\text{ThSiO}_4\text{-USiO}_4$  solid solution is about 11 kJ/(mol exchangeable cations) (Ferriss et al., 2010). The enthalpy of mixing curves are asymmetric with a maxima around  $x = 0.63$  Th mole fraction; thus, the greatest amount of unmixing is expected to occur in this composition range. Lower enthalpy structures (*i.e.*, an ordered structure and an exsolved structure) are marked in Figure 2.4a and discussed below.

In order to quantify the degree of unmixing, the free energy of mixing has to be evaluated. At temperatures below 1000 K, the free energy of mixing curves for the  $\text{Th}_x\text{U}_{1-x}\text{O}_2$  binary have a minimum at low and high Th concentrations, indicating exsolution (Figure 2.4b). The contact points, where the tangent line touches the energy of mixing curve, define the minimum and maximum Th concentration between which

Table 2.3. Comparison of calculated  $\langle \text{Me-O} \rangle$  ( $\text{Me} = \text{Th}, \text{U}$ ) bond lengths with measured values. The calculated values are averaged over all  $\langle \text{Me-Me} \rangle$  and  $\langle \text{Me-O} \rangle$  bonds within each configuration.

solid	Calculated distance Å			Measured distance Å		
	$\langle \text{Th-O} \rangle$	$\langle \text{U-O} \rangle$	$\langle \text{Me-Me} \rangle$	$\langle \text{Th-O} \rangle$	$\langle \text{U-O} \rangle$	$\langle \text{Me-Me} \rangle$
$\text{ThO}_2$	2.42		3.95	2.42		3.96
$\text{Th}_{0.5}\text{U}_{0.5}\text{O}_2$	2.41	2.39	3.91	2.42	2.38	3.92
$\text{UO}_2$		2.38	3.87		2.37	3.87

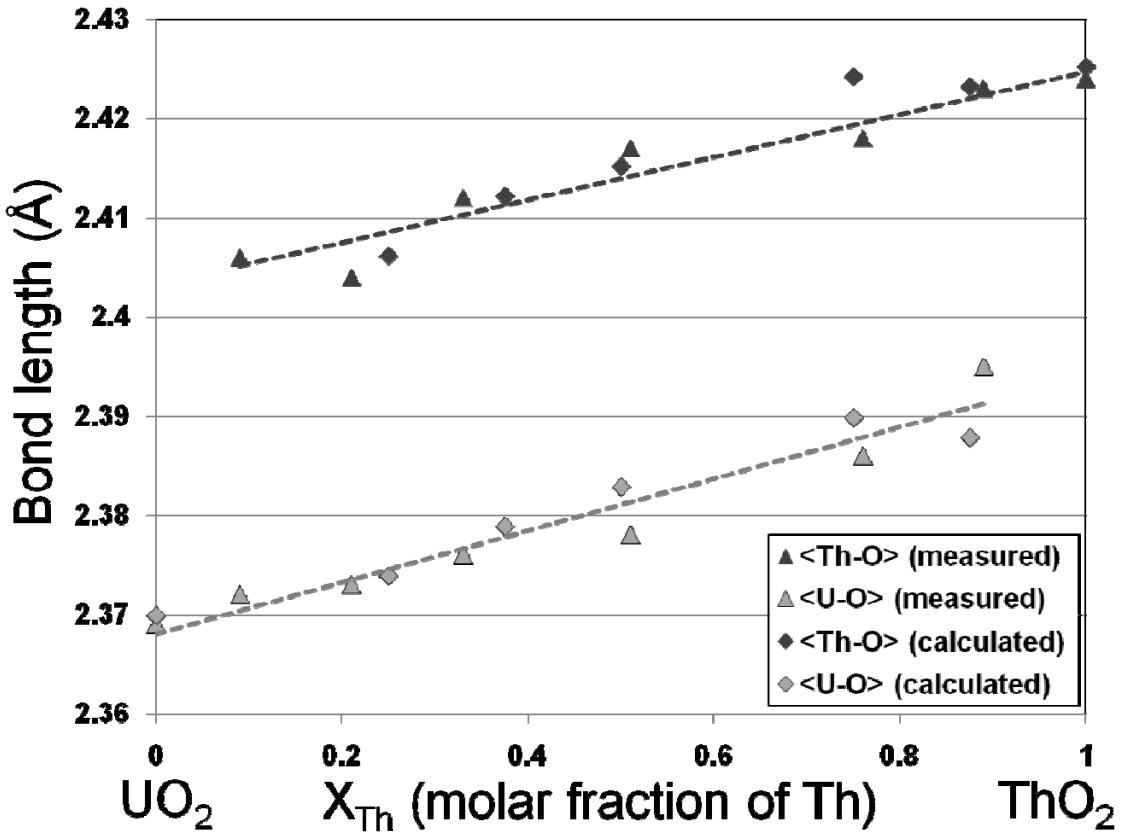


Figure 2.3. The calculated nearest-neighbor  $\langle \text{Th}-\text{O} \rangle$  and  $\langle \text{U}-\text{O} \rangle$  bond lengths are corrected for the 0.3% mismatch in the lattice parameter and compared with EXAFS measurements.

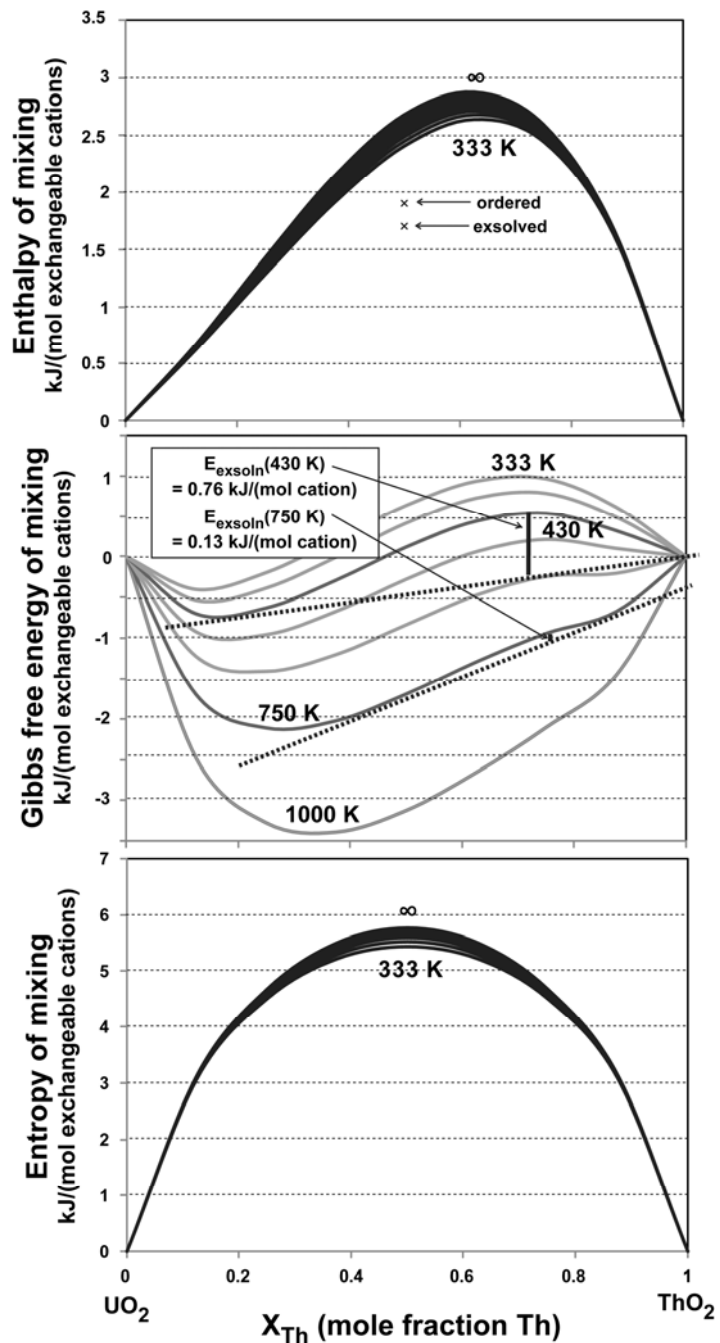


Figure 2.4. Thermodynamic mixing properties with respect to concentration Th and temperature from the Monte-Carlo simulation (a) Enthalpy of mixing with the enthalpy for the ordered and exsolved structures marked; (b) Gibbs free energy of mixing indicates a tendency for exsolution, where the driving force ( $E_{\text{exsoln}}$ ) is labeled at 750 K and 430 K; (c) Configurational entropy is nearly equal to the point entropy (configurational entropy without ordering) at all temperatures.

exsolution can potentially occur. Thus, the solvus can be derived based on the intersection of the tangents to each temperature-dependent free energy curve, and the resulting temperature-composition phase diagram for the  $\text{Th}_x\text{U}_{1-x}\text{O}_2$  binary is shown in Figure 2.5. The phase diagram in Figure 2.5 is, however, based on the assumption that all energy contributions are considered in the Monte-Carlo calculations and the subsequent thermodynamic integration. The validity of this assumption and additional energy contributions are discussed below. As shown in Figure 2.4c, the configurational entropy at all temperatures is almost equal to the point entropy, which is the configurational entropy without ordering, indicating that the system is not converging to a specifically ordered state.

The lack of cation ordering, as indicated from the configurational entropy curves, is observed from the Monte-Carlo results at all calculated temperatures (Figure 2.6a). However, based on the free energy of mixing, exsolution is expected to occur below 1000 K. Figure 2.6b shows a completely mixed ordering scheme of alternating Th/U layers  $\parallel$  to (100) that is homogeneous down to the scale of the original conventional unit cell. Symmetrically equivalent to this ordered structure are alternating Th/U layers  $\parallel$  to (001) and (010). Slightly more energetically favorable, according to the Monte-Carlo simulations, is the nano-exsolved structure in Figure 2.6c. The driving force, or respective energy to go from the mixed to the exsolved structure, is defined as the exsolution energy ( $E_{exsoln}$ ) labeled in Figure 2.4b. A further complication arises from the fact that the exsolved layers, which are indexed to be (21 $\bar{1}$ ) in Figure 2.6c, may be a linear combination of exsolution in the {111}, {100}, and their symmetry-equivalent directions. That means that the exsolution pattern can change direction as shown in the

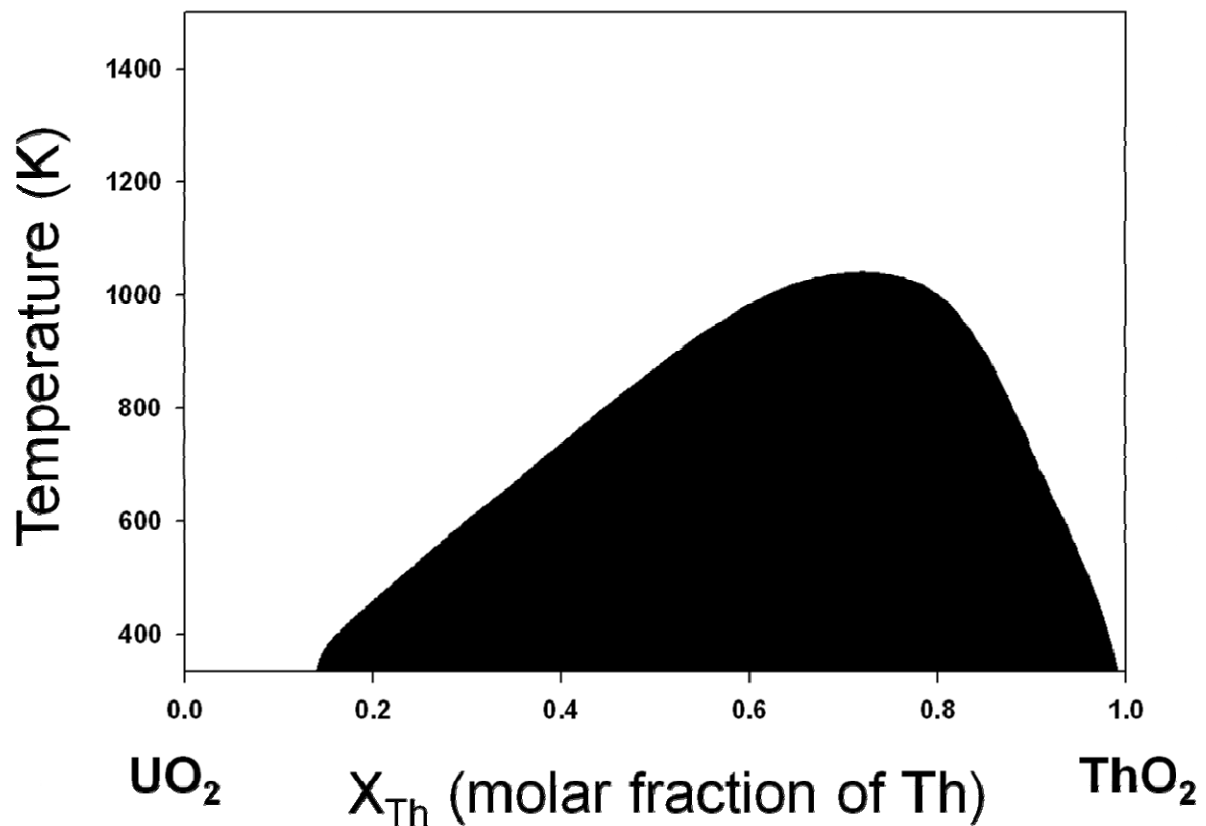


Figure 2.5. Estimated temperature-composition phase diagram indicating the miscibility gap in the  $\text{Th}_x\text{U}_{1-x}\text{O}_2$  binary.

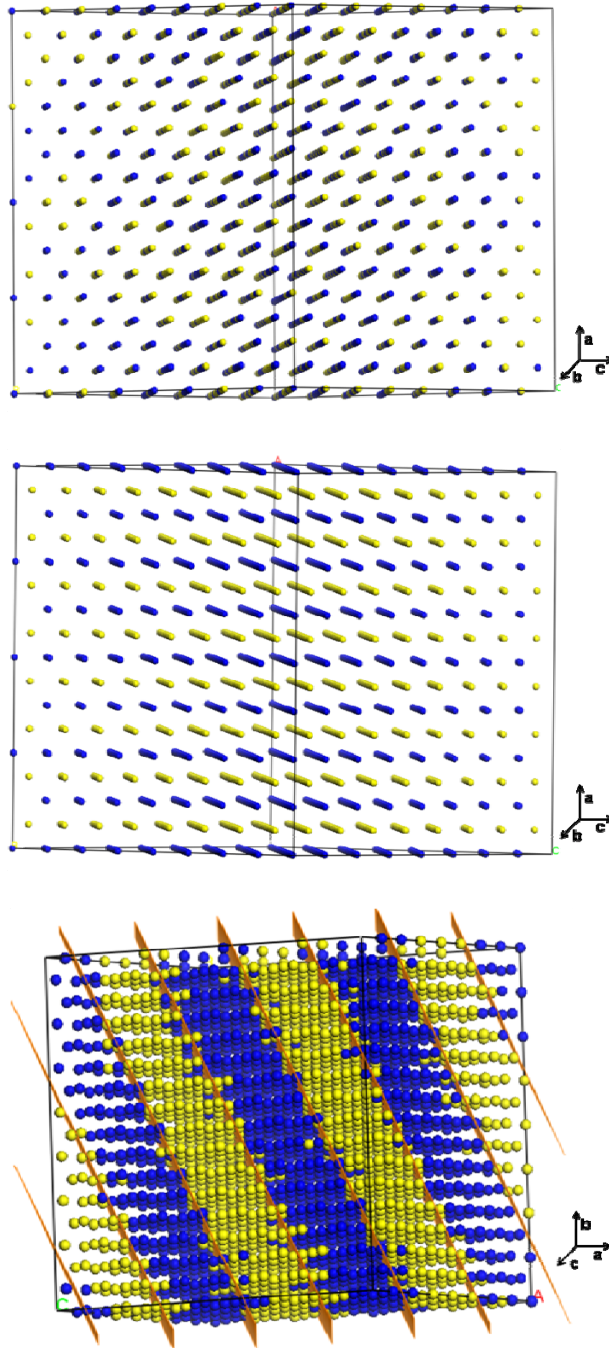


Figure 2.6. Schematic of cations indicating the (a) random arrangement of cations at temperatures above 200 K, (b) alternating U and Th layers  $\parallel \{1\ 0\ 0\}$ , which is the most favorable unexsolved configuration for a 50:50 composition, and (c) exsolved lamellae structure  $\parallel (2\ 1\ \bar{1})$  at temperatures below 200 K which is one of the most favorable exsolved structures.

experimental BSE image of exsolved grossular-andradite garnet by Pollok et al. (2001).

Extremely low equilibration temperatures (< 200 K) would be necessary to stabilize a lamellar structure, which would result in a substantially lower enthalpy of mixing for 0.5 mole fraction Th (1.69 kJ/(mol exchangeable cation)). If the system were to order, the enthalpy of mixing would be 1.87 kJ/(mol exchangeable cation) at 0.5 mole fraction Th. However, energetic competition between ordering in different directions and exsolution in different directions out-weighs the driving forces for ordering and/or exsolution.

The driving force for the exsolution,  $E_{exsoln}$ , is determined as the difference between the maximum of the free energy of mixing curve and the tangent line that connects the minima of the same curve. The tendency towards exsolution is exemplified in Figure 2.7, which shows free energy of mixing curves for three simulated binaries at a given temperature,  $T$ . The free energy of mixing curves have different maxima at 0.5 concentration; however, the phase diagram for each of the simulated binaries would be identical, solely based on the concentrations corresponding to the intersection of a tangent line through the minima. The system with largest  $E_{exsoln}$  has the greatest tendency for exsolution. The  $E_{exsoln}$  for the  $\text{Th}_x\text{U}_{1-x}\text{O}_2$  binary at temperatures below 1000 K is small – from 0.13 kJ/(mol cations) at 750 K up to 1.12 kJ/(mol cations) at 333 K – indicating that the tendency towards exsolution is low. The Monte-Carlo simulations inherently “flatten” the free energy curves because the cations are able to swap positions with cations some distance away. Basically, the system is able to tunnel through kinetically hindered configurations (*e.g.*, consisting of very thin exsolution lamellae with a number of interfaces between U-rich and Th-rich phases) that would be caused by slow

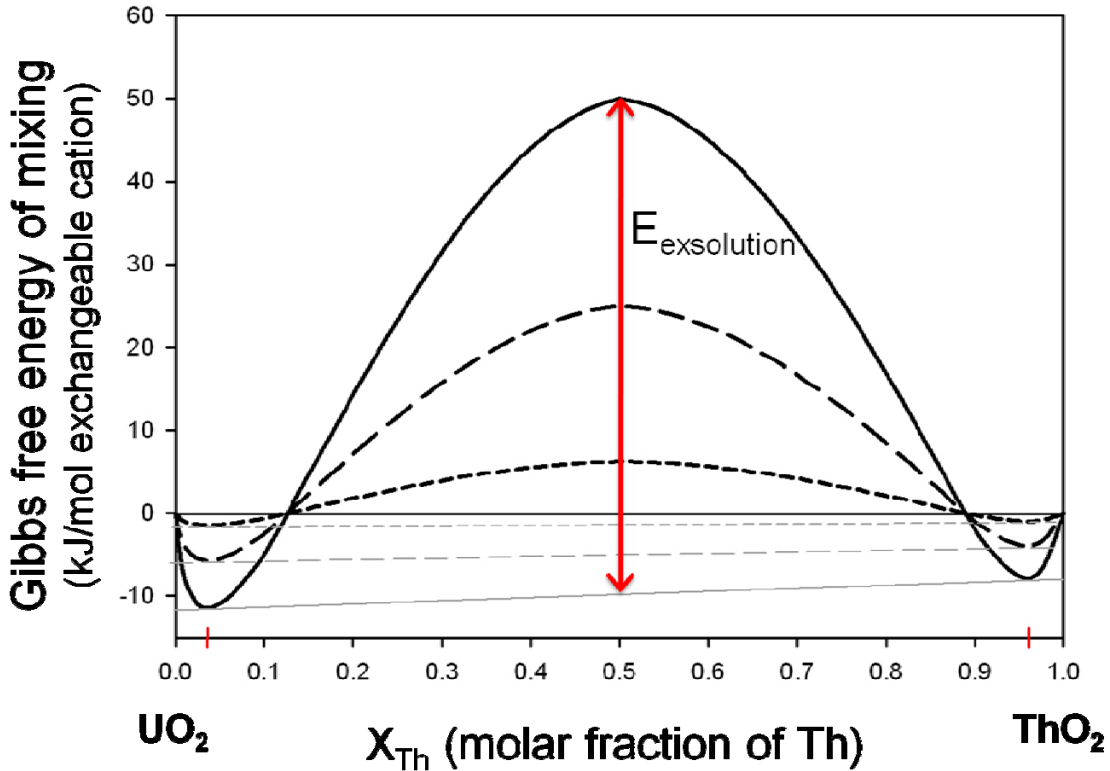


Figure 2.7. Example Gibbs free energy of mixing curves *versus* composition indicating that, while the maximum of the curves are different in magnitude, the composition at which the tangential line to the minima intersects each curve is the same (marked in red on the x-axis).

cation diffusion rates; however, diffusion is not explicitly considered during the Monte-Carlo simulation. Exsolution is further hindered by factors such as the buildup of a lattice mismatch at the interface. Low temperatures are necessary for exsolution (by producing high  $E_{exsoln}$  values) to overcome the interfacial energy ( $E_{IF}$ ) of the exsolution lamellae; however, the same low temperatures would slow down the diffusion that is needed to actually generate low-energy exsolution features, such as lamellae.

Exsolution occurs when the  $E_{exsoln}$  is greater than the  $E_{IF}$ , which is composed of a chemical and strain component. The chemical contributions (*i.e.*, the local U-Th interactions across the interface) to the interface energy are contained in the interaction parameters,  $J_i$ . However, the strain that accumulates as a result of the lattice mismatch is not included because only small unit cells can be used in the quantum-mechanical calculations that are the basis for the derivation of the  $J$ 's. A large quantum-mechanical unit cell would be required in order to calculate the strain between a U-rich and Th-rich phase, which would be computationally expensive. Thus, results from a study on the solid solution and phase separation of the isometric garnet compositions, andradite [ $\text{Ca}_3\text{Fe}_2(\text{SiO}_4)_3$ ] and grossular [ $\text{Ca}_3\text{Al}_2(\text{SiO}_4)_3$ ], are used as a rough estimate for the interface energy (Becker and Pollok, 2002). The garnet solid solution may be a suitable analogy because the grossular-andradite system has similar lattice mismatch (1.8%) as the uraninite-thorianite system, and interfaces are chemically similar, *i.e.*, between high-spin ( $\text{U}^{4+}$  or  $\text{Fe}^{3+}$ ) and low-spin ( $\text{Th}^{4+}$  or  $\text{Al}^{3+}$ ) phases. The  $E_{IF}$  for the grossular-andradite exsolution lamellae was calculated to be  $\sim 1 \text{ meV}/\text{\AA}^2$  or  $96.5 \cdot 10^{-3} \text{ kJ}/(\text{mol } \text{\AA}^2)$  (Becker and Pollok, 2002), and this value is used in Equation 7 to calculate the  $E_{IF}$  for the  $\text{ThO}_2$ - $\text{UO}_2$  lamellae.

$$E_{IF} = A (\text{\AA}^2/\text{unit cell}) \cdot E'_{IF} (\text{kJ}/(\text{mol \AA}^2)) \cdot I/N_c (\text{unit cell}/\# \text{ cations}) \quad (7)$$

$$= 37778.72 \text{ \AA}^2/\text{cell} \cdot 96.5 \cdot 10^{-3} \text{ kJ}/(\text{mol \AA}^2) \cdot 1/8198 (\text{cell}/\# \text{ cations})$$

$$\approx 0.4 \text{ kJ}/(\text{mol cations})$$

where  $A$  is the area of the interface,  $E'_{IF}$  is the interface energy per unit area taken from the grossular-andradite example, and the  $N_c$  is the number of cations in the unit cell. The factor  $I/N_c$  is used to normalize the interface energy to a number of cations involved in the formation of the interfaces rather than an interface area, which makes it easier to compare  $E_{IF}$  with  $E_{exsoln}$ . The total interface area was obtained by cleaving the  $8 \times 8 \times 8$  supercell along the  $(21\bar{1})$  starting at the first interface, resulting in a rectangular slab with 8 interchanging layers of U and Th. The total interface area is  $37,778 \text{ \AA}^2/\text{cell}$ , and the total number of cations in the slab is 8,198 cations/cell. The  $E_{IF}$  for the exsolved  $\text{Th}_{0.5}\text{U}_{0.5}\text{O}_2$  structure is  $0.4 \text{ kJ}/(\text{mol cation})$  – substantially larger than the  $E_{exsoln}$  at 750 K, which indicates that the driving force for exsolution cannot overcome the interface energy. The above estimate of the driving force to form lamellae *versus* the build-up of interface energy becomes more favorable for the former if the lamellae are thicker. In the above example,  $E_{IF}$  and  $E_{exsoln}$  become equal if the average thickness of the lamellae increases from  $\sim 10.2 \text{ \AA}$  (*i.e.*, the lamellae are about three cation rows thick and spaced about  $3.4 \text{ \AA}$  apart) to  $\sim 45.9 \text{ \AA}$ . However, slow diffusion requires much longer equilibration times. In addition, wider/thicker lamellae would have to be formed without going through the less energetically favored thinner ones, which is unlikely. These additional hindrances are even greater at lower temperatures. For example, the  $E_{exsoln}$  at 333 K ( $E_{exsoln} = 1.12 \text{ kJ}/(\text{mol cations})$ ) is greater than the  $E_{IF}$ , yet exsolution is not

observed in the Monte-Carlo simulation until below room temperature. The onset of exsolution is reached well before discernable exsolution lamellae are observed because the driving force for exsolution is small.

### **Composition of natural and synthetic $\text{Th}_x\text{U}_{1-x}\text{O}_2$**

One approach to validating the incorporation limit of  $\text{ThO}_2$  in  $\text{UO}_2$ , as calculated in this study, is to compare the calculated results with analytical data on the compositions of natural and synthetic samples. The difficulty with such an approach is that most analytical methods do not distinguish between nanoscale exsolution features and truly homogeneous solid solutions. In addition, especially for synthetic samples, equilibrium is often not reached due to insufficient time for equilibration. Finally, whether the thermodynamically-possible incorporation limit is actually reached in natural samples may be limited by the composition of the fluid from which the solid solution formed.

Natural samples of uraninite and thorianite containing various amounts of Th and U, respectively, have been documented (Berman, 1957; Evins et al., 2005; Frondel, 1958; Jensen and Ewing, 2001; Robinson and Sabina, 1955). Uraninite samples from the natural fission reactor at Oklo-Okélobondo uranium deposit in southeast Gabon contain minimal amounts of  $\text{ThO}_2$  (< 0.1 wt% oxide) (Evins et al., 2005; Jensen and Ewing, 2001). The Oklo-Okélobondo uranium deposits formed during the accumulation of oxidized U-rich saline fluids, which later came into contact with reducing oil-rich fluids, causing the reduction of  $\text{U}^{6+}$  to  $\text{U}^{4+}$ . Thorium, which only occurs in the 4+ oxidation state, would not have been mobilized in the oxidized U-rich saline fluid. Thus, Th is present as a fissiogenic daughter product of  $^{240}\text{Pu}$  and  $^{236}\text{U}$  generated by neutron-capture

reactions (Jensen and Ewing, 2001). Similarly, only minimal concentrations of ThO<sub>2</sub> are found in sedimentary and vein-type uraninite deposits due the oxidation of uranium to U(VI) in solution prior to precipitation.

Of the three types of natural uraninite deposits (sedimentary, vein-type, or igneous), typically only the igneous deposits contain fractions of ThO<sub>2</sub> greater than 1 mol % (Berman, 1957; Finch and Ewing, 1992). The composition of uraninite and thorianite from igneous rocks of the Grenville province of the Canadian Shield contain U:Th ratios ranging from 9.2 to 0.43. The compositions of the uraninites were evaluated based on oxide weight % using U<sub>3</sub>O<sub>8</sub> as the U-oxide (25-73 wt% U<sub>3</sub>O<sub>8</sub> and 7-55 wt% ThO<sub>2</sub>) (Robinson and Sabina, 1955). Frondel (1958) noted that uraninites primarily contain < 20 wt% ThO<sub>2</sub>, and those containing equal amounts of U and Th are rare. Based on the compositions of natural samples, there is no clear evidence that the Th<sub>x</sub>U<sub>1-x</sub>O<sub>2</sub> binary is a continuous solid solution.

Chemical analysis and XRD data for synthetic Th<sub>x</sub>U<sub>1-x</sub>O<sub>2</sub> support the hypothesis of complete solid solution, based on the agreement of the unit cell parameters with Vegard's law, which is an indirect measure that indicates the linearity of the energetics of the binary (Lambertson et al., 1953; Slowinski and Elliott, 1952; Trzebiatowski and Selwood, 1950; Tyagi et al., 2004). The unit cell parameters of natural and synthetic samples are typically measured using bulk analysis techniques, such as X-ray diffraction (XRD); thus, potential local expansion or contraction beyond Vegard's law would be difficult to detect. In addition, Vegard's law is only a rough indication of the thermodynamics across a solid-solution series. The synthesis temperatures for typical specimens range from 1273 K to 1573 K - above the critical temperature based on the

calculations in this study. Thus, if the synthetic samples were cooled rapidly, a homogeneous composition would be quenched.

### **Comparison with calorimetric measurements**

Calorimetric measurements can be used to determine the energetic state of intermediate compositions for direct comparison to the calculated thermochemical parameters of the solid solution. The calculated enthalpies and Gibbs free energies are reported as enthalpies of mixing and free energies of mixing. Thermodynamic mixing properties are calculated in reference to a linear combination of the end-members and can be directly compared to measured thermodynamic mixing properties. The measured enthalpies and Gibbs free energies from solid-solution experiments are typically for intermediate compositions; thus, end-member enthalpies and Gibbs free energies must be obtained from different studies in order to calculate the excess properties. For example, Kandan et al. (2009) reported enthalpy increments ( $H_T - H_{298}$ ) for  $\text{Th}_x\text{U}_{1-x}\text{O}_2$ , where  $x = 0.1, 0.5$ , and  $0.9$ . The enthalpy increments reported by Fink (1982) for the end-members are used to convert the enthalpy increments of the intermediate members to enthalpies of mixing so that the measurements can be compared with the computationally-determined enthalpies of mixing (Figure 2.8a). The calculated and measured enthalpies of mixing both have limited temperature dependence. In addition, the asymmetry of the calculated enthalpy curve is similar to the asymmetry of the measured enthalpy curve, as indicated by the similar change in the enthalpy between  $X_{\text{Th}} = 0.1$  and  $0.9$  for the calculated (1.8 kJ/(mol cations)) and measured (1.5 kJ/(mol cations)) results.

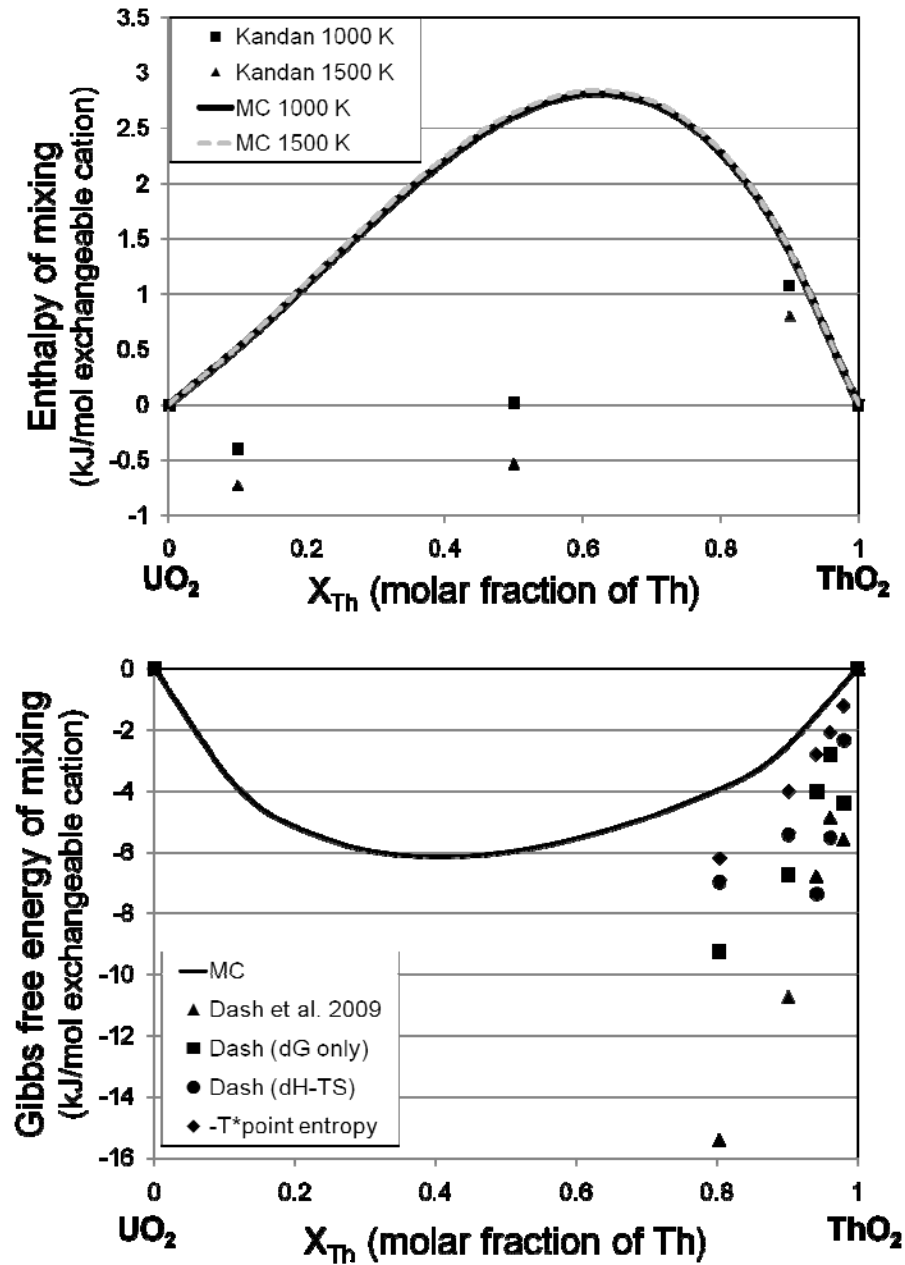


Figure 2.8. (a) Comparison of Monte-Carlo results at 1000 K and 1500 K with enthalpy of mixing from Kandan et al. (2009), using Fink (1982) for end-member enthalpies. Both have a similar asymmetry and small changes with temperature. (b) Comparison of Monte-Carlo results at 1500 K with Gibbs free energy of mixing from Dash et al. (2009), using Robie and Hemingway (1995) for end-member energies. Dash et al. results are shown as they appear to be calculated based on Equation 23 in their paper, based on only  $\Delta G$ , and based on Equation 23 using  $\Delta H$  instead of  $\Delta G$ . In addition,  $-T^*$ point entropy is shown.

The enthalpies of mixing across the  $\text{Th}_x\text{U}_{1-x}\text{O}_2$  binary are small ( $< 3 \text{ kJ}/(\text{mol exchangeable cation})$ ); therefore, the Gibbs free energy of mixing is dominated by the configurational entropy. This effect is observed by comparing the calculated Gibbs free energy of mixing with the measured Gibbs free energy of mixing (Dash et al., 2009). The measurements, reported for  $\Delta_f G_m^\circ$ , are for the intermediate compositions ( $x = 0.8036, 0.902, 0.9412, 0.9608, 0.9804$ ) and  $\text{ThO}_2$ , but not  $\text{UO}_2$ . Both end-members are required in order to convert the measurements to Gibbs free energies of mixing, so the  $\Delta_f G_m^\circ$  for  $\text{ThO}_2$  and  $\text{UO}_2$  were taken from Robie and Hemingway (1995). Figure 2.8b shows a comparison of the  $\Delta G_{mix}$  at 1500 K for the intermediate compositions measured by Dash et al. (2009) with respect to the end members reported in Robie and Hemingway (1995) and the computationally-determined Gibbs free energies of mixing. The measured  $\Delta G_{mix}$  are calculated based Equation 8, which is modified from Dash et al. to convert the reference frame from  $\text{Th}_{1-y}\text{U}_y\text{O}_2$  to  $\text{Th}_x\text{U}_{1-x}\text{O}_2$  (*i.e.*, the reference system of this study).

$$\begin{aligned} \Delta G_{mix}(\text{Th}_x\text{U}_{1-x}\text{O}_2, s, T) &= \{\Delta_f G_m^\circ(\text{Th}_x\text{U}_{1-x}\text{O}_2, s, T)\} - \{x \Delta_f G_m^\circ(\text{ThO}_2, s, T) \\ &\quad + (1-x) \cdot \Delta_f G_m^\circ(\text{UO}_2, s, T)\} + T \cdot R \{(1 - x) \cdot \ln(1 - x) + x \cdot \ln x\} \end{aligned} \quad (8)$$

Based on Equation 8, the measured  $\Delta G_{mix}$  are about four times more negative (*i.e.*, lower in energy) than the calculated results. However, Equation 8, as written in Dash et al., is inaccurate. The last term is the point entropy, which is the ideal entropy of mixing, but the  $\Delta_f G_m^\circ$  term already includes entropy. If the point entropy term is eliminated, the calculated  $\Delta G_{mix}$  is only twice that of the measured  $\Delta G_{mix}$ . Equation 8 can be rewritten such that the enthalpy of formation ( $\Delta_f H_m^\circ$ ) replaces the free energy of formation ( $\Delta_f G_m^\circ$ ) (Equation 9). The measured  $\Delta_f H_m^\circ$  across the binary decreases almost linearly with

increasing temperature; however, above 1000 K the  $\Delta_f H_m^\circ$  fluctuates slightly (Dash et al., 2009; Robie and Hemingway, 1995).

$$\begin{aligned}\Delta G_{mix}(\text{Th}_x\text{U}_{1-x}\text{O}_2, s, T) = & \{\Delta_f H_m^\circ(\text{Th}_x\text{U}_{1-x}\text{O}_2, s, T)\} - \{x \Delta_f H_m^\circ(\text{ThO}_2, s, T) \\ & + (1-x) \cdot \Delta_f H_m^\circ(\text{UO}_2, s, T)\} + T \cdot R \{(1 - x) \cdot \ln(1 - x) + x \cdot \ln x\}\end{aligned}\quad (9)$$

The calculated and measured enthalpy of mixing is small (< 3 kJ/mol for the calculated values and < 1 kJ/mol for the measured samples; Figure 2.8a). Thus, a good estimate of the Gibbs free energy of mixing is based on the ideal entropy of mixing (also shown in Figure 2.8b). While systematic measurements of  $\Delta G_{mix}$  for the full solid solution from ThO<sub>2</sub> to UO<sub>2</sub> are currently not available, the measurements described above are in good agreement with the calculated  $\Delta G_{mix}$ .

### **Implications for Th<sub>x</sub>U<sub>1-x</sub>O<sub>2</sub> solid solutions**

Analysis of nanoscale exsolution (shown in Figure 2.6c as a computational example) in experiments is often difficult because one has to have nano-scale resolution, and this is often difficult to detect. For example, transmission electron microscopy has been used to resolve the nano-scale exsolution lamella in the isometric garnet compositions, andradite and grossular, which was previously considered a complete solid solution (Pollock et al., 2001). However, few studies exist in which such high-resolution techniques are used to re-evaluate solid solutions. Ordering within the unit cell, as shown in Figure 2.6b, but extending only to the range of a nano-domain is often even harder to detect experimentally. To a certain degree, one would be able to detect the internal domain structure (*e.g.*, number of Th-U interactions in the first coordination shell) using EXAFS. However, the local structure information obtained using EXAFS is spatially averaged.

To the authors' knowledge, an atomic-scale investigation of the energetics and cation ordering in the  $\text{Th}_x\text{U}_{1-x}\text{O}_2$  system has not been conducted.

The cation ordering determined from the Monte-Carlo simulations and the phase diagram generated from the calculated Gibbs free energy of mixing indicate that the  $\text{Th}_x\text{U}_{1-x}\text{O}_2$  system has a small tendency to exsolve below 1000 K (727 °C); however, exsolution lamellae are observed only for calculations at temperatures below 200 K. The only experimental evidence that may indicate exsolution in the  $\text{Th}_x\text{U}_{1-x}\text{O}_2$  binary is the sharp increase in magnetic susceptibility at 55 mol%  $\text{ThO}_2$  in  $\text{UO}_2$  (Trzebiatowski and Selwood, 1950). However, nano-scale exsolution cannot be detected from bulk analysis techniques (*e.g.*, XRD). Natural and synthetic samples could be homogeneous, and appear completely miscible, due to quenching from the high synthesis temperatures (> 1000 °C), and kinetic hindrances due to slow cation diffusion may inhibit exsolution.

## References

- Becker, U., and Pollok, K. (2002) Molecular simulations of interfacial and thermodynamic mixing properties of grossular-andradite garnets. *Physics and Chemistry of Minerals*, 29(1), 52-64.
- Becker, U., Risthaus, P., Brandt, F., and Bosbach, D. (2006) Thermodynamic properties and crystal growth behavior of the hashemite ( $\text{BaSO}_4\text{-BaCrO}_4$ ) solid solution. *Chemical Geology*, 225(3-4), 244-255.
- Berman, R.M. (1957) The role of lead and excess oxygen in uraninite. *American Mineralogist*, 42(11-2), 705-731.
- BNL. (1973) Neutron Cross Sections, 3rd ed. Brookhaven National Laboratory.
- Dash, S., Parida, S.C., Singh, Z., Sen, B.K., and Venugopal, V. (2009) Thermodynamic investigations of  $\text{ThO}_2\text{-UO}_2$  solid solutions. *Journal of Nuclear Materials*, 393(2), 267-281.

- Demkowicz, P.A., Jerden, J.L., Cunnane, J.C., Shibuya, N., Baney, R., and Tulenko, J. (2004) Aqueous dissolution of urania-thoria nuclear fuel. Nuclear Technology, 147(1), 157-170.
- Evins, L.Z., Jensen, K.A., and Ewing, R.C. (2005) Uraninite recrystallization and Pb loss in the Oklo and Bangombe natural fission reactors, Gabon. *Geochimica Et Cosmochimica Acta*, 69(6), 1589-1606.
- Ferriss, E.D.A., Essene, E.J., and Becker, U. (2008) Computational study of the effect of pressure on the Ti-in-zircon geothermometer. European Journal of Mineralogy, 20(5), 745-755.
- Ferriss, E.D.A., Ewing, R.C., and Becker, U. (2010) Simulation of thermodynamic mixing properties of actinide-containing zircon solid solutions. American Mineralogist, 95(2-3), 229-241.
- Finch, R.J., and Ewing, R.C. (1992) The corrosion of uraninite under oxidizing conditions. *Journal of Nuclear Materials*, 190, 133-156.
- Fink, J.K. (1982) Enthalpy and heat capacity of the actinide oxides. *International Journal of Thermophysics*, 3(2), 165-200.
- Frondel, C. (1958) Systematic mineralogy of uranium and thorium. viii, 400 p. p. U.S. G.P.O., Washington, [D.C.].
- Hazen, R.M., Ewing, R.C., and Sverjensky, D.A. (2009) Evolution of uranium and thorium minerals. *American Mineralogist*, 94(10), 1293-1311.
- Herring, J.S., MacDonald, P.E., Weaver, K.D., and Kullberg, C. (2001) Low cost, proliferation resistant, uranium-thorium dioxide fuels for light water reactors. *Nuclear Engineering and Design*, 203(1), 65-85.
- Hubert, S., Purans, J., Heisbourg, G., Moisy, P., and Dacheux, N. (2006) Local structure of actinide dioxide solid solutions  $\text{Th}_{1-x}\text{U}_x\text{O}_2$  and  $\text{Th}_{1-x}\text{Pu}_x\text{O}_2$ . *Inorganic Chemistry*, 45(10), 3887-3894.
- IAEA. (2005) Thorium fuel cycle - Potential benefits and challenges. International Atomic Energy Agency, Vienna, Austria.
- Janeczak, J., and Ewing, R.C. (1992) Dissolution and alteration of uraninite under reducing conditions. *Journal of Nuclear Materials*, 190, 157-173.

- Jensen, K.A., and Ewing, R.C. (2001) The Okelobondo natural fission reactor, southeast Gabon: Geology, mineralogy, and retardation of nuclear-reaction products. Geological Society of America Bulletin, 113(1), 32-62.
- Kandan, R., Babu, R., Manikandan, P., Krishnan, R.V., and Nagarajan, K. (2009) Calorimetric measurements on (U,Th)O<sub>2</sub> solid solutions. Journal of Nuclear Materials, 384(3), 231-235.
- Kurina, I.S., Gudkov, L.S., and Rumyantsev, V.N. (2002) Investigation of ThO<sub>2</sub> and (U, Th)O<sub>2</sub>. Atomic Energy, 92(6), 461-467.
- Kutty, T.R.G., Kulkarni, R.V., Sengupta, P., Khan, K.B., Bhanumurthy, K., Sengupta, A.K., Panakkal, J.P., Kumar, A., and Kamath, H.S. (2008) Development of CAP process for fabrication of ThO<sub>2</sub>-UO<sub>2</sub> fuels Part II: Characterization and property evaluation. Journal of Nuclear Materials, 373(1-3), 309-318.
- Lambertson, W.A., Mueller, M.H., and Gunzel, F.H. (1953) Uranium oxide phase equilibrium systems .4. UO<sub>2</sub>-ThO<sub>2</sub>. Journal of the American Ceramic Society, 36(12), 397-399.
- MacDonald, P.E., and Lee, C.B. (2004) Use of thoria-urania fuels in PWRs: A general review of a NERI project to assess feasible core designs, economics, fabrication methods, in-pile thermal/mechanical behavior, and waste form characteristics. Nuclear Technology, 147(1), 1-7.
- McEnroe, S.A., Harrison, R.J., Robinson, P., and Langenhorst, F. (2002) Nanoscale haematite-ilmenite lamellae in massive ilmenite rock: an example of 'lamellar magnetism' with implications for planetary magnetic anomalies. Geophysical Journal International, 151(3), 890-912.
- Murabaya, M., Namba, S., Takahash.Y, and Mukaibo, T. (1969) Thermal conductivity of ThO<sub>2</sub>-UO<sub>2</sub> system. Journal of Nuclear Science and Technology-Tokyo, 6(3), 128.
- Myers, E.R. (1998) A statistical-mechanics model of ordering in aluminosilicate solid solutions. Physics and Chemistry of Minerals, 25(6), 465-468.
- Payne, M.C., Teter, M.P., Allan, D.C., Arias, T.A., and Joannopoulos, J.D. (1992) Iterative minimization techniques for ab initio total-energy calculations -

- Molecular-dynamics and conjugate gradients. *Reviews of Modern Physics*, 64(4), 1045-1097.
- Perdew, J.P., and Wang, Y. (1992) Accurate and simple analytic representation of the electron-gas correlation-energy. *Physical Review B*, 45(23), 13244-13249.
- Pollok, K., Jamtveit, B., and Putnis, A. (2001) Analytical transmission electron microscopy of oscillatory zoned grandite garnets. *Contributions to Mineralogy and Petrology*, 141(3), 358-366.
- Reich, M., and Becker, U. (2006) First-principles calculations of the thermodynamic mixing properties of arsenic incorporation into pyrite and marcasite. *Chemical Geology*, 225(3-4), 278-290.
- Robie, R.A., and Hemingway, B.S. (1995) Thermodynamic properties of minerals and related substances at 298.15 K and 1 bar (10 p5 s pascals) pressure and at higher temperatures. *U.S. Geological Survey Bulletin*, 2131, p. 461.
- Robinson, S.C., and Sabina, A.P. (1955) Uraninite and thorianite from Ontario and Quebec. *American Mineralogist*, 40(7-8), 624-633.
- Segall, M.D., Lindan, P.J.D., Probert, M.J., Pickard, C.J., Hasnip, P.J., Clark, S.J., and Payne, M.C. (2002) First-principles simulation: ideas, illustrations and the CASTEP code. *Journal of Physics-Condensed Matter*, 14(11), 2717-2744.
- Skomurski, F.N., Ewing, R.C., Rohl, A.L., Gale, J.D., and Becker, U. (2006) Quantum mechanical vs. empirical potential modeling of uranium dioxide ( $\text{UO}_2$ ) surfaces: (111), (110), and (100). *American Mineralogist*, 91(11-12), 1761-1772.
- Skomurski, F.N., Shuller, L.C., Ewing, R.C., and Becker, U. (2008) Corrosion of  $\text{UO}_2$  and  $\text{ThO}_2$ : A quantum-mechanical investigation. *Journal of Nuclear Materials*, 375(3), 290-310.
- Slowinski, E., and Elliott, N. (1952) Lattice constants and magnetic susceptibilities of solid solutions of uranium and thorium dioxide. *Acta Crystallographica*, 5(6), 768-770.
- Takahashi, Y., and Murabayashi, M. (1975) Measurement of thermal properties of nuclear materials by laser flash method. *Journal of Nuclear Science and Technology*, 12(3), 133-144.

- Trzebiatowski, W., and Selwood, P.W. (1950) Magnetic susceptibilities of urania thoria solid solutions. *Journal of the American Chemical Society*, 72(10), 4504-4506.
- Tyagi, A.K., Mathews, M.D., Ambekar, B.R., and Ramachandran, R. (2004) Thermal expansion of ThO<sub>2</sub>-2, 4 and 6 wt.% UO<sub>2</sub> by HT-XRD. *Thermochimica Acta*, 421(1-2), 69-71.
- Vanderbilt, D. (1990) Soft self-consistent pseudopotentials in a generalized eigenvalue formalism. *Physical Review B*, 41(11), 7892-7895.
- Wyckoff, R. (1963) Crystal structures 1. Interscience Publishers, New York, New York.
- Yeomans, J.M. (1992) Statistical Mechanics of Phase Transitions. Oxford Science Publications, Clarendon Press, Oxford.

## Chapter 3

# Atomistic calculations of the thermodynamic properties of mixing for tetravalent metal dioxide solid solutions: $(\text{Zr}, \text{Th}, \text{Ce})\text{O}_2$

### Abstract

The thermodynamic properties of mixing for  $\text{Th}_x\text{Ce}_{1-x}\text{O}_2$ ,  $\text{Ce}_x\text{Zr}_{1-x}\text{O}_2$ , and  $\text{Th}_x\text{Zr}_{1-x}\text{O}_2$  were calculated using quantum-mechanical calculations and Monte-Carlo simulations. The solid-solution properties are calculated within the isometric *Fm3m* framework, and phase transitions have yet to be considered. The maximum enthalpies of mixing, which occur at infinite temperature and  $x = 0.5$ , are 2.7, 11.8, and 23 kJ/(mol exchangeable cations) for  $\text{Th}_x\text{Ce}_{1-x}\text{O}_2$ ,  $\text{Ce}_x\text{Zr}_{1-x}\text{O}_2$ , and  $\text{Th}_x\text{Zr}_{1-x}\text{O}_2$ , respectively. While the  $\text{Th}_x\text{Ce}_{1-x}\text{O}_2$  binary indicates exsolution below 600 K, the tendency for exsolution is small ( $E_{exsoln} = 1.5$  kJ/(mol cations) at  $T = 200$  K). The tendency for exsolution is significant for the Zr-bearing binaries, where at  $T = 1000$  K  $E_{exsoln} = 6$  kJ/(mol cations) for the  $\text{Ce}_x\text{Zr}_{1-x}\text{O}_2$  binary and  $E_{exsoln} = 17$  kJ/(mol cations) for the  $\text{Th}_x\text{Zr}_{1-x}\text{O}_2$  binary. Thus, there is complete miscibility for the  $\text{Th}_x\text{Ce}_{1-x}\text{O}_2$  solid solution, but miscibility in the Zr-bearing solid solutions is limited. At 1400 °C, only 3.6 and 0.09 mol%  $\text{ZrO}_2$  is miscible in  $\text{CeO}_2$  and  $\text{ZrO}_2$ , respectively. Cation ordering is observed for both the  $\text{Ce}_x\text{Zr}_{1-x}\text{O}_2$  and  $\text{Th}_x\text{Zr}_{1-x}\text{O}_2$

binaries at 200 K for composition  $x = 0.5$ ; however, the superstructure ordering for the  $\text{Ce}_x\text{Zr}_{1-x}\text{O}_2$  binary may also be considered nanoscale exsolution, in which the two-cation-layer thick lamellae exsolve parallel to the  $(10\bar{2})$ .

## Introduction

Several  $\text{AX}_2$  oxides are known to share the isometric fluorite,  $\text{CaF}_2$ , structure, including those relevant to current and advanced nuclear fuels (*e.g.*,  $\text{UO}_2$ ,  $\text{ThO}_2$ ). For U-based fuels, Zr, Ce, and Th are all the result of nuclear reactions or radioactive decay. Mixed-Th-U fuels are being researched in the United States and are already in use in India. Ce is often used experimentally as a surrogate for Pu because of similarities in atomic radii and valence states. In addition, the Ce-Zr dioxide binary has been extensively studied for use as an automobile exhaust catalyst, fuel cell electrolyte, and oxygen gas sensor (Subbarao, 1981; Yashima et al., 1996; Kaspar et al., 1999). At high temperatures,  $\text{ZrO}_2$ , which has been proposed as an inert matrix fuel, can also have the fluorite structure. These oxides are thought to form complete solid solutions. The homogeneity of the solid solutions, as well as the thermodynamic properties of mixing, must be known to truly understand the behavior of such materials in fuel fabrication, performance in a reactor, and behavior as a waste form. An extensive atomistic evaluation of the  $\text{Th}_x\text{U}_{1-x}\text{O}_2$  binary was previously reported (Shuller et al. 2010) and that work is now expanded to the dioxide solid solutions containing tetravalent cations with unoccupied f orbitals. Specifically, binaries within the  $\text{ThO}_2\text{-CeO}_2\text{-ZrO}_2$  system are evaluated here. The thermodynamic mixing properties of these dioxide solid solutions are calculated, including the enthalpy of mixing, Gibbs free energy of mixing, and configurational entropy of mixing. From these properties, one can identify any tendency

toward exsolution or the formation of stable ordered phases. The mixing in these binaries may affect physical and chemical properties, such as thermal conductivity, which will influence the performance of nuclear fuels.

## Methods

Quantum-mechanical (QM) geometry optimizations are used to calculate the enthalpy of mixing for a variety of compositions and configurations. QM calculations are used to capture electronic information, which may be important for the evaluation of cation ordering. Approximations are necessary for solving the Schrödinger equation for multi-bodied systems. The current results were calculated using the planewave (as basis functions for the overall wavefunction), pseudo-potential (to mimic the role of the core electrons) code CASTEP (Segall et al., 2002) with the generalized gradient approximation (Perdew et al., 1996) for the electron exchange and correlation contributions to the total energy. The kinetic energy cut-off for the planewaves was 500 eV and the k-point spacing was  $0.1 \text{ \AA}^{-1}$ , which results in 9 k-points for the  $2 \times 1 \times 1$  unit cell (*P1*) that was chosen for calculating the energy of a limited number of cation configurations within the  $(\text{Zr},\text{Th},\text{Ce})\text{O}_2$  solid solution. The total energy convergence tolerance was  $1 \cdot 10^{-5} \text{ eV/atom}$ . Geometry optimizations were performed without symmetry constraints, and, in order to improve convergence and save computational time, the starting unit cell parameters for the intermediate structures were weighted averages of the end-member parameters. A spin-polarized approach was unnecessary because none of the cations involved in the solid solution have unpaired electrons. For this same reason, the Hubbard U theory was not applied, as there were no unpaired 5f electrons that needed to be screened for Columbic interactions.

Cation-cation interaction parameters are fit to the energies from the QM calculations and are subsequently used in Monte-Carlo (MC) simulations, in which the system is scaled up to 2048 exchangeable cations (Ferriss et al., 2008; Reich and Becker, 2006). The Bogoliubov integration scheme is then used to determine the temperature-dependent Gibbs free energy and configurational entropy (Myers, 1998). The details of the interaction parameter fitting and subsequent MC simulation and thermodynamic integration are in the Methods section of Chapter 2 (Shuller et al., 2010b).

The dioxide end members all have the isometric fluorite structure, where the cations are in octahedral coordination and fill every other cube of the oxygen sublattice (Figure 2.1).  $\text{ZrO}_2$  is typically monoclinic or tetragonal unless at high temperature; however, an isometric structure can be stabilized at ambient conditions (*e.g.*, Y-stabilized  $\text{ZrO}_2$ ) (Duwez et al., 1951). The  $2 \times 1 \times 1$  unit cell contains 8 exchangeable cation sites, and there are multiple configurations at different compositions, resulting in 26 different configurations across the binary. For the  $2 \times 1 \times 1$  unit cell 4 interaction types ( $J_1, J_2, J_3, J_5$ ) were included in the fit, where the first interaction type describes nearest-neighbor interactions, the second describes second nearest-neighbor interactions, and so forth. The fourth nearest-neighbor interaction is linearly dependent on the first nearest-neighbor interaction; therefore,  $J_4$  is not included in the fit.

## Results

The first and fifth interaction parameters are the largest in magnitude and provide the most information about the system. For example, the nearest-neighbors for the  $\text{Th}_x\text{Ce}_{1-x}\text{O}_2$  binary want to be the same cations (negative  $J$ ), but at longer distances, heterocationic ordering (positive  $J$ ) is preferred. The fits for the different binaries are

compared in Table 3.1. The Margules parameters show that the  $\text{Th}_x\text{Ce}_{1-x}\text{O}_2$ ,  $\text{Ce}_x\text{Zr}_{1-x}\text{O}_2$ , and  $\text{Th}_x\text{Zr}_{1-x}\text{O}_2$  binaries are nearly symmetric. Additionally, the binaries containing Zr have larger Margules parameters and larger interaction parameters than the other solid solutions, indicating a greater tendency for unmixing or cation ordering.

The temperature-dependent thermodynamic properties of mixing, specifically  $\Delta H_{mix}$ ,  $\Delta G_{mix}$ , and  $\Delta S_{mix}$ , were calculated according to the Monte-Carlo simulation and thermodynamic integration described above. The enthalpy of mixing is positive for all binaries; however, the magnitudes of the  $\Delta H_{mix}$  and  $\Delta G_{mix}$  curves, which are indicative of the ideality of the solid solution, vary significantly (Figure 3.1). The maximum enthalpy of mixing, which occurs at a theoretical infinite temperature and  $x = 0.5$  is only 2.7 kJ/(mol exchangeable cations) for  $\text{Th}_x\text{Ce}_{1-x}\text{O}_2$ , while the maximum enthalpy of mixing is 11.8 kJ/(mol exchangeable cations) for  $\text{Ce}_x\text{Zr}_{1-x}\text{O}_2$  and 23 kJ/(mol exchangeable cations) for  $\text{Th}_x\text{Zr}_{1-x}\text{O}_2$ . Interestingly, the enthalpy curves for the solid solutions containing Zr appear to flatten at  $x = 0.5$  at 100 K for  $\text{Ce}_x\text{Zr}_{1-x}\text{O}_2$  and 300 K for  $\text{Th}_x\text{Zr}_{1-x}\text{O}_2$ .

The Gibbs free energy of mixing curves (Figure 3.2), which clearly show miscibility gaps for all binaries, is used to generate the temperature-composition phase diagram (Figure 3.3). The  $\text{Th}_x\text{Zr}_{1-x}\text{O}_2$  binary has a miscibility gap for all calculated temperatures (below 3000 K), while the  $\text{Ce}_x\text{Zr}_{1-x}\text{O}_2$  binary has a miscibility gap below 1500 K. While the  $\text{Th}_x\text{Ce}_{1-x}\text{O}_2$  binary indicates exsolution below 600 K, the tendency for exsolution is small ( $E_{exsoln} = 1.5$  kJ/(mol cations) at  $T = 200$  K). The tendency for exsolution is significant for the Zr-bearing binaries, where at  $T = 1000$  K  $E_{exsoln} = 6$  kJ/(mol cations) for the  $\text{Ce}_x\text{Zr}_{1-x}\text{O}_2$  binary and  $E_{exsoln} = 17$  kJ/(mol cations) for the  $\text{Th}_x\text{Zr}_{1-x}\text{O}_2$  binary. Thus, exsolution is expected based on the Gibbs free energy of mixing.

Table 3.1. Cation-cation exchange fit parameters including Margules parameters ( $W_1$  and  $W_2$ ), interaction parameters ( $J_{1-5}$ ), and the correlation coefficient for the fit. Note negative  $J_i$  indicates heterocationic interactions are preferred, while positive  $J_i$  indicates homocationic interactions are preferred.

Parameter	$\text{Th}_x\text{U}_{1-x}\text{O}_2$	$\text{Th}_x\text{Ce}_{1-x}\text{O}_2$	$\text{Ce}_x\text{Zr}_{1-x}\text{O}_2$	$\text{Th}_x\text{Zr}_{1-x}\text{O}_2$
$W_1$	15.2	10.1	46.7	99.3
$W_2$	2.8	10.5	51.9	95.7
$J_1$	0.024	-0.022	-0.038	-0.030
$J_2$	0.024	0.009	-0.027	-0.085
$J_3$	-0.002	0.007	0.021	0.033
$J_4$	Linearly dependent on $J_1$			
$J_5$	-0.018	0.005	-0.001	-0.019
Corr coeff	0.960	0.995	0.996	0.997

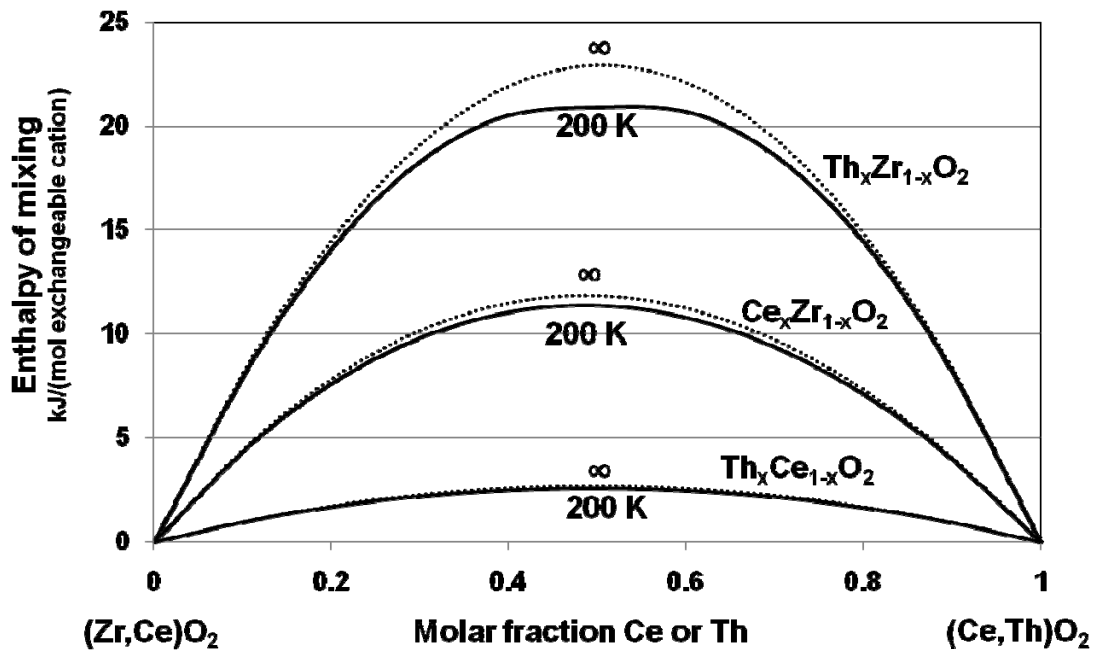


Figure 3.1. Positive enthalpy of mixing for the  $\text{Th}_x\text{Zr}_{1-x}\text{O}_2$ ,  $\text{Ce}_x\text{Zr}_{1-x}\text{O}_2$ , and  $\text{Th}_x\text{Ce}_{1-x}\text{O}_2$  binaries indicates some unmixing, the degree of which depends on the magnitude of the enthalpy of mixing at  $x = 0.5$ .

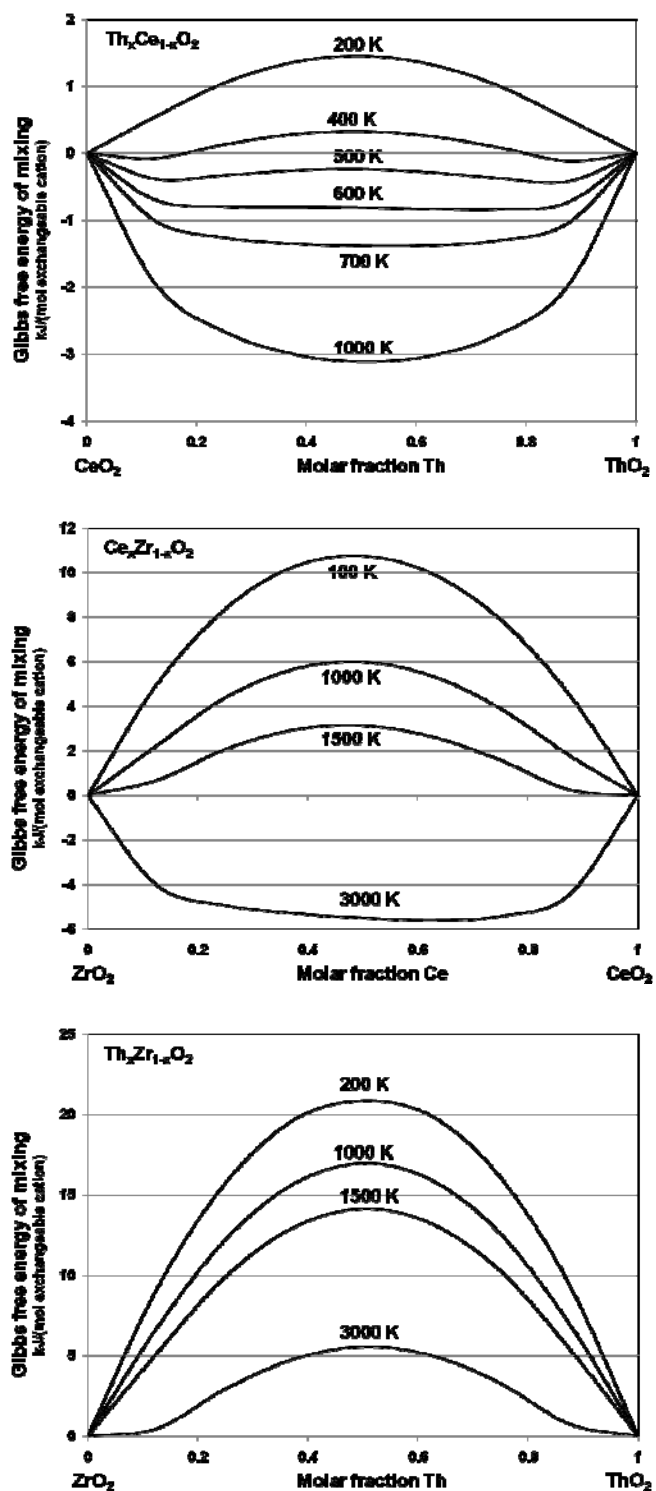


Figure 3.2. Gibbs free energy of mixing curves indicating exsolution below 600 K for  $\text{Th}_x\text{Ce}_{1-x}\text{O}_2$ , 3000 K for  $\text{Ce}_x\text{Zr}_{1-x}\text{O}_2$  and  $\text{Th}_x\text{Zr}_{1-x}\text{O}_2$ .

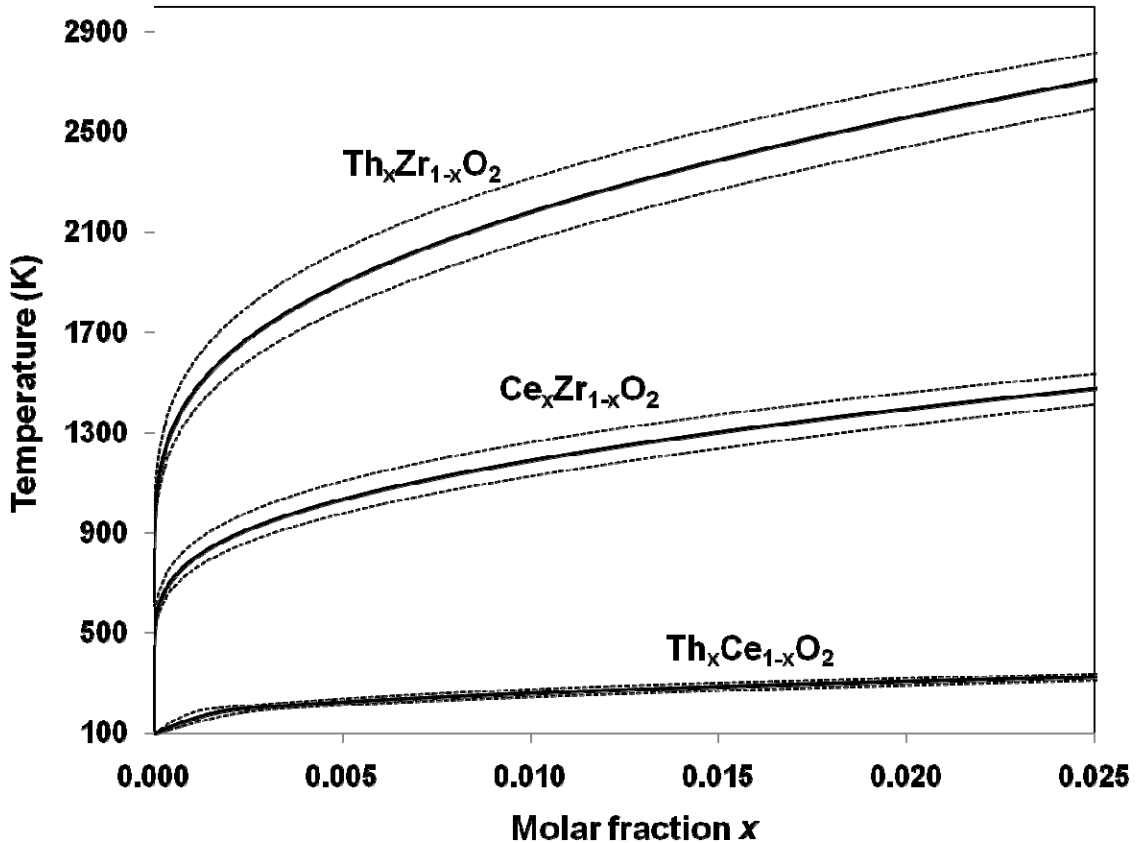


Figure 3.3. Temperature-composition phase diagram showing miscibility gaps for the  $\text{Th}_x\text{Ce}_{1-x}\text{O}_2$ ,  $\text{Ce}_x\text{Zr}_{1-x}\text{O}_2$ , and  $\text{Th}_x\text{Zr}_{1-x}\text{O}_2$  binaries. The solid black solidus is an average of the linear and Margules approximations for the incorporation limit ( $x_{inc}$ ), and the dotted lines represent the solidus are the Margules approximation (above the average) and the linear approximation (below the average).

In addition, the configurational entropy curves are nearly  $T$ -independent and equal to the point entropy, which is the configurational entropy without ordering (Figure 3.4). However, for the  $\text{Ce}_x\text{Zr}_{1-x}\text{O}_2$  and  $\text{Th}_x\text{Zr}_{1-x}\text{O}_2$  binaries, the configurational entropy drops significantly at low temperature at  $x = 0.5$ . Thus, some cation ordering or exsolution lamellae are expected as discussed below.

## Discussion

### *Exsolution tendency*

Although immiscibility is evident for all binaries based on the Gibbs free energy of mixing, the driving force for exsolution for the  $\text{Th}_x\text{Ce}_{1-x}\text{O}_2$  binary may not be great enough to allow the system to actually exsolve. The driving force for exsolution,  $E_{exsoln}$ , is defined as the height between the peak of the free energy curve and the tangent connecting the minima of that curve (Shuller et al., 2010b). The value for  $E_{exsoln}$  is small for the  $\text{Th}_x\text{Ce}_{1-x}\text{O}_2$  binary (only 1.5 kJ/(mol cations) at 200 K), which can be closely compared with the  $\text{Th}_x\text{U}_{1-x}\text{O}_2$  binary presented in the previous chapter. Similarly, the  $E_{exsoln}$  for the  $\text{Th}_x\text{U}_{1-x}\text{O}_2$  binary is 1.12 kJ/(mol cations) at 333 K, which was the lowest calculated  $T$ . While exsolution lamellae develop for the  $\text{Th}_x\text{U}_{1-x}\text{O}_2$  binary, no lamellae are observed computationally for the  $\text{Th}_x\text{Ce}_{1-x}\text{O}_2$  binary. The lack of exsolution lamellae are attributed to several factors, including kinetic hindrances (*i.e.*, slow cation diffusion and interfacial energies), differences in cation-cation interaction parameters, and challenges in trying to find the appropriate exsolution pathway.

The kinetic hindrances for the  $\text{Th}_x\text{Ce}_{1-x}\text{O}_2$  binary probably outweigh the driving forces for exsolution. Specifically, the  $E_{exsoln}$  does not overcome the interfacial energy

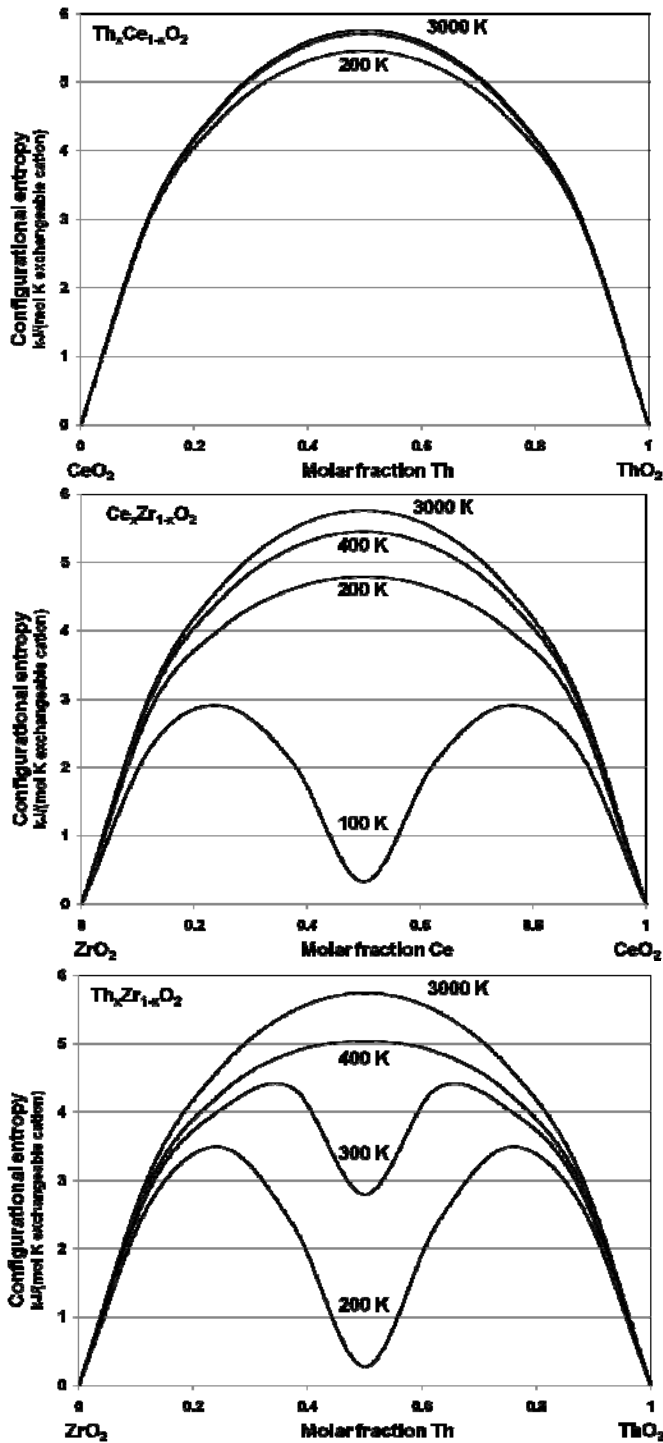


Figure 3.4. Configurational entropy curves are nearly equal to the point entropy (*i.e.*, configurational entropy without ordering). However, a sharp minima at  $x = 0.5$  at extremely low  $T$  is present for the Zr-bearing binaries indicating ordering.

due to the lattice mismatch between the end-member phases. The interfacial energy for the  $\text{Th}_x\text{Ce}_{1-x}\text{O}_2$  binary is expected to be larger than that of the Th-U binary because the difference in ionic radii, and thus unit cell parameter, is larger. That is, the difference in unit cell parameter for the  $\text{ThO}_2$ - $\text{CeO}_2$  end-members is 0.19 Å, while that for the  $\text{ThO}_2$ - $\text{UO}_2$  end-members is 0.17 Å. While this difference between the lattice mismatch of the binaries is only 0.02 Å, the kinetic hindrances towards exsolution, specifically slow cation diffusion, are enhanced at low temperatures, preventing the formation of exsolution lamellae. Such kinetic hindrances are less important in the Monte-Carlo simulations because cation swaps are allowed across some kinetic barriers; therefore, they may not be the primary cause for the difference between the  $\text{Th}_x\text{U}_{1-x}\text{O}_2$  and  $\text{Th}_x\text{Ce}_{1-x}\text{O}_2$  simulation results.

The primary computational difference arises from the difference in the cation-cation interaction parameters. While both binaries have small interaction parameters, the sign of the parameters differ for different interaction types. Most importantly, the first and fifth nearest neighbor interactions for the  $\text{Th}_x\text{U}_{1-x}\text{O}_2$  binary indicate homocationic interactions (U-U or Th-Th) are favored between nearest neighbors, while the  $\text{Th}_x\text{Ce}_{1-x}\text{O}_2$  binary indicates heterocationic interactions are favored at nearest neighbor distances. Thus, neighboring cations in the  $\text{Th}_x\text{Ce}_{1-x}\text{O}_2$  binary prefer to be different. Additionally, the fifth nearest-neighbor interaction for the  $\text{Th}_x\text{Ce}_{1-x}\text{O}_2$  binary is three times less than the same interaction for the  $\text{Th}_x\text{U}_{1-x}\text{O}_2$  binary, indicating that the system has little preference at longer cation distances.

Finally, exsolution in the  $\text{Th}_x\text{Ce}_{1-x}\text{O}_2$  binary does not strongly favor any of the three most common planes, that is  $\{100\}$ ,  $\{110\}$ , or  $\{111\}$ . MC simulations starting with

exsolution lamellae parallel to (100), (110), and (111) resulted in relatively homogeneous solid solutions with energies of about -0.161 kJ/(mol cations) for lamellae  $\parallel$  to (100) and (110) and -0.157 kJ/(mol cations) for lamellae  $\parallel$  to (111) at 100 K. Thus, even at extremely low temperature and initially exsolved cation arrangements, the potential lamellae of the  $\text{Th}_x\text{Ce}_{1-x}\text{O}_2$  binary tend to form a random distribution of cations, resulting in a homogeneous solid solution. The homogeneity of the  $\text{Th}_x\text{Ce}_{1-x}\text{O}_2$  solid solution is further confirmed by several experimental measurements (Bukaemskiy et al., 2009; Pepin and McCarthy, 1981 and references therein) that show the linearity of the change in the unit cell parameter with composition, which is in accordance to Vegard's law.

As in the  $\text{Th}_x\text{Ce}_{1-x}\text{O}_2$  binary, exsolution is evident from the energy of mixing curves for the  $\text{Ce}_x\text{Zr}_{1-x}\text{O}_2$  and  $\text{Th}_x\text{Zr}_{1-x}\text{O}_2$  binaries. While no exsolution lamellae were observed computationally for the  $\text{Th}_x\text{Ce}_{1-x}\text{O}_2$  binary, exsolution is expected for the Zr-containing binaries because the driving forces for exsolution are much larger. The driving force for exsolution for the  $\text{Ce}_x\text{Zr}_{1-x}\text{O}_2$  and  $\text{Th}_x\text{Zr}_{1-x}\text{O}_2$  binaries at  $T = 1000$  K are  $E_{exsoln} = 6$  kJ/(mol cations) and  $E_{exsoln} = 17$  kJ/(mol cations), respectively. Such large tendencies for exsolution are expected based on a simple comparison of ionic radii, where the ionic radii of octahedrally-coordinated Zr(IV) is only 0.98 Å as compared with the ionic radii of octahedrally-coordinated Ce(IV) and Th(IV) (1.11 Å and 1.19 Å, respectively). A local strain is imposed on the system when a cation is substituted by another cation that is significantly ( $>10\%$ ) smaller or larger. To overcome this strain, the system may exsolve into lamellae that are rich in one cation and depleted in the other. Alternatively, the cations may order in such a way as to reduce the total energy of the binary. The configurational entropy for both the  $\text{Ce}_x\text{Zr}_{1-x}\text{O}_2$  and  $\text{Th}_x\text{Zr}_{1-x}\text{O}_2$  binaries

show a drop in entropy at low  $T$  (Figure 3.4), which is consistent with either ordering or exsolution.

Detailed experimental analysis of the nanoscale structure of  $\text{Ce}_{0.5}\text{Zr}_{0.5}\text{O}_2$  particles shows nanocrystallites on the order of  $21.5 - 41.5 \text{ \AA}$  in diameter (Mamontov et al., 2003). Such nanocrystallites were not observed as exsolution features from the Monte-Carlo simulation; however, size of the nanocrystallites would require the simulation of a much larger system. In this study, a  $3 \times 3 \times 3$  supercell is used for the MC simulation, which results in a  $40.7 \times 40.7 \times 40.7 \text{ \AA}^3$  structure. Thus, only one nanocrystallite could possibly form in the MC simulation. However, nanoscale exsolution lamellae are observed for the  $\text{Ce}_x\text{Zr}_{1-x}\text{O}_2$  binary at low  $T$  (Figure 3.5), where the lamellae are about two cation layers thick and form  $\parallel$  to the  $(10\bar{2})$ , which is a linear combination of  $(101)$  and  $(00\bar{1})$ . Competitive exsolution of lamellae  $\parallel$  to any linear combination of the  $\{110\}$  and  $\{100\}$ , which are equivalent to  $\{101\}$  and  $\{001\}$  in an isometric system, such as fluorite, may be the cause of the experimentally observed nanocrystallites for  $\text{Ce}_{0.5}\text{Zr}_{0.5}\text{O}_2$ . The nanoscale exsolution in the  $\text{Ce}_x\text{Zr}_{1-x}\text{O}_2$  binary may alternatively be considered as a superstructure ordering, which is responsible for the decrease in the enthalpy of mixing at  $x = 0.5$  at 100 K (Figure 3.1). Complete exsolution would correspond to an enthalpy of mixing of zero. However, further exsolution into thicker lamellae may be kinetically hindered due to slow cation diffusion, especially at the low temperatures required for the nanoscale exsolution lamellae to form.

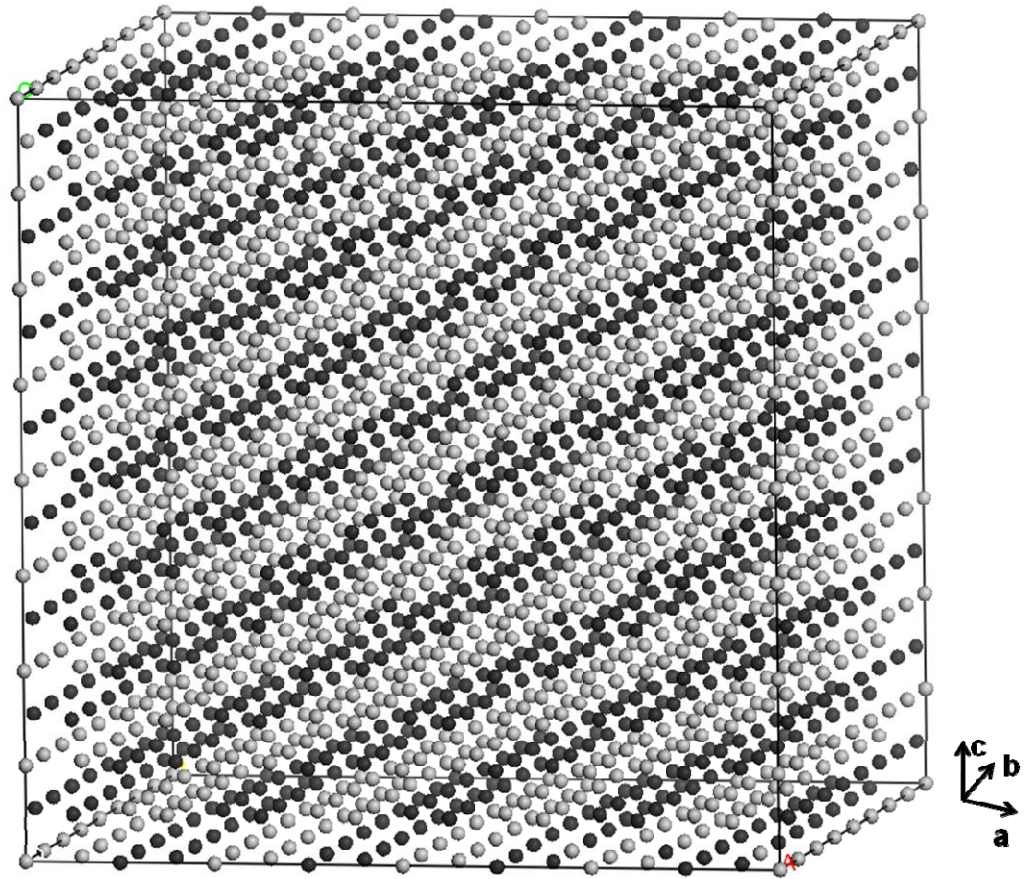


Figure 3.5. The  $\text{Ce}_x\text{Zr}_{1-x}\text{O}_2$  binary displays exsolution lamellae at 100 K and  $x = 0.5$  that are about two cation layers thick ( $\sim 4.5 \text{ \AA}$ ) and  $\parallel$  to  $(10\bar{2})$ .

### **Cation ordering and end-member stability**

Although the thermodynamic properties of mixing for the  $\text{Th}_x\text{Zr}_{1-x}\text{O}_2$  binary appear similar to the  $\text{Ce}_x\text{Zr}_{1-x}\text{O}_2$  binary, exsolution is not observed from the MC simulation. Thus, the significant drop in configurational entropy at low  $T$  when  $x = 0.5$  is due to the ordering of the cations in an energetically favored arrangement. A good example of cation-ordering is in the calcite-magnesite ( $\text{CaCO}_3$ - $\text{MgCO}_3$ ) solid solution, which exhibits a significant drop in entropy at  $x = 0.5$ . This drop in entropy corresponds to ordering of the Ca and Mg, which results in the phase dolomite  $\text{CaMg}(\text{CO}_3)_2$  with alternating Ca and Mg layers in the [001] direction (Navrotsky and Capobianco, 1987). Similarly, cation ordering is observed for the  $\text{Th}_x\text{Zr}_{1-x}\text{O}_2$  binary at 200 K at  $x = 0.5$ , where rows of alternating cations lie in the (100). Additionally, the cation rows lying in subsequent (100) layers along the [001] zone axis are rotated by 30° (Figure 3.6).

No experimental evidence of an ordered phase in the  $\text{Th}_x\text{Zr}_{1-x}\text{O}_2$  binary has been found; however, the solid-solution behavior of the  $\text{Th}_x\text{Zr}_{1-x}\text{O}_2$  binary is highly dependent on the synthesis method. For example, solid solutions synthesized in a series of three grinding, pelletizing, annealing (at 1200 °C, 1300 °C, and 1400 °C), and cooling cycles show phase separations from  $\text{Th}_{0.05}\text{Zr}_{0.95}\text{O}_2$  to  $\text{Th}_{0.95}\text{Zr}_{0.05}\text{O}_2$  (Grover and Tyagi, 2002). The phase separations were identified by the appearance of monoclinic zirconia peaks in powder diffraction patterns. However, solid solutions synthesized from a melt (about 3000 °C) and quenched show miscibility of 17.5 mol % Th in cubic- $\text{ZrO}_2$  (Duwez and Loh, 1957). The melting points for  $\text{ThO}_2$ ,  $\text{ZrO}_2$ , and  $\text{CeO}_2$  are about 3300 °C, 2750°C, and 2600 °C, respectively; therefore, at small concentrations of  $x$ , homogeneous cation

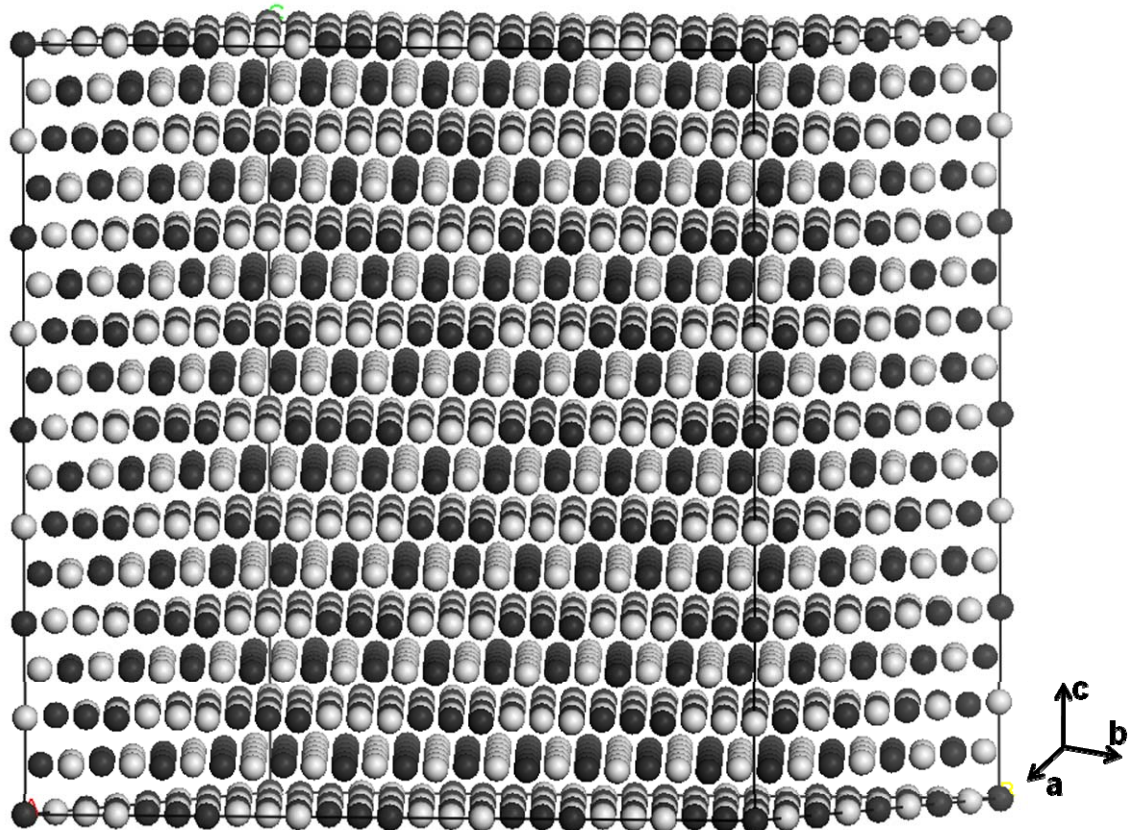


Figure 3.6. Ordering is observed for the  $\text{Th}_x\text{Zr}_{1-x}\text{O}_2$  binary at  $x = 0.5$  and  $T = 200$  K.

arrangements in the  $\text{Th}_x\text{Zr}_{1-x}\text{O}_2$  and  $\text{Ce}_x\text{Zr}_{1-x}\text{O}_2$  binaries could be quenched from a melt. However, upon further heat treatment, phase separation occurs due to the transformation of  $\text{ZrO}_2$  from a cubic to tetragonal structure. Although the cation coordination remains the same in the cubic to tetragonal phase transition ( $\text{CN} = 8$ ), the oxygen atoms are displaced, and the unit cell parameter in the  $c$ -direction is lengthened. Experiments have identified two tetragonal forms (termed  $t$ ,  $t'$ ) for the  $\text{Ce}_x\text{Zr}_{1-x}\text{O}_2$  binary with identical  $P4_2/nmc$  space group and connectivity but different  $c/a$  ratios, where  $t$  and  $t'$  exist in the compositional ranges 5-20 mol% and 40-60 mol%  $\text{CeO}_2$  in  $\text{ZrO}_2$  with a  $c/a = 1.018$  and 1.010, respectively (Vlaic et al., 1999). The  $t$  tetragonal form is stable at high temperatures and transformable to the monoclinic form at room temperature, while the  $t'$  tetragonal form is metastable and does not transform (Otsuka-Yao-Matsuo et al., 2003; Vlaic et al., 1998; Yashima et al., 1994). In addition, a metastable tetragonal phase ( $t''$ ) is found at high  $\text{CeO}_2$  compositions and is often misinterpreted as cubic because the  $c/a$  value is 1 (Yashima et al., 1994). Oxygen displacements can be used to identify the metastable tetragonal structure. In the cubic structure the  $z$ -position for the oxygen atom is 0.125; however, for the tetragonal structure the  $z$  position for the oxygen atom is 0.185 (Teufer, 1962).

Further, the tetragonal to monoclinic inversion of  $\text{ZrO}_2$  at room temperature cannot be suppressed. The phase transition to the monoclinic structure involves a change in the coordination of the cations from 8 to 7. The small ionic radius of Zr requires the shortening of the  $\langle \text{Zr-O} \rangle$  bond distance, therefore, the coordination number decreases due to coulombic repulsion between the oxygen atoms. Monoclinic  $\text{ZrO}_2$  ( $P2_1/c$ ) is stable at room temperature and occurs in nature as baddelyite. However,  $\text{ThO}_2$  and  $\text{CeO}_2$  are

stable at room temperature with the isometric fluorite symmetry (*Fm*3*m*), and occur naturally as the minerals thorianite and cerianite, respectively.

The calculations presented here are based on the isometric *Fm*3*m* symmetry across the entire binary, yet the calculations are actually performed with *P*1 symmetry. Unit cell elongation along one direction was observed in several quantum-mechanical structural optimizations, which hinted at the binary being tetragonal. One indication that a structure is tetragonal or deviates from being isometric is the deviation of the *c/a* ratio from unity (e.g., Vlaic et al., 1999). The largest *c/a* ratio (*c/a* = 1.011) for the Th<sub>x</sub>Zr<sub>1-x</sub>O<sub>2</sub> binary calculations is for the configuration with a concentration *x* = 0.5, in which the cations (*i.e.*, Th and Zr) exsolve || to (001) and form lamellae that are 2 cation-layers thick. For this configuration, the final unit cell parameters in the *a* and *b* directions are 5.334 Å, while the final unit cell parameter in the *c* direction is 5.393 Å. Based on the *c/a* ration, where *c/a* = 1.011, this configuration could be considered as tending towards a tetragonal structure. In addition, the oxygen atoms are displaced by 0.0147 fractional units in the *c*-direction, which corresponds to 0.158 Å. The original <Me-O> (Me = Th, Zr) bond distance was 2.32 Å, while the final <Zr-O> bond distance is 2.27 Å, and the final <Th-O> bond distances are 2.38 Å and 2.35 Å, respectively, where the longer <Th-O> distances are for O that are also coordinated by Zr. The shortening of the <Zr-O> bond distance is due to compensation for the smaller ionic radii of Zr. Based on the crystal structure of tetragonal zirconia, the oxygen positions are expected to deviate by ~ 0.060 fractional units in the *c*-direction, which corresponds to about 0.32 Å based on a *c* parameter of 5.27 Å (Teufer, 1962). Thus, with knowledge of experimentally-determined end-member stability in addition to the quantum-mechanical calculations and MC

simulations, one can say that the  $\text{Th}_x\text{Zr}_{1-x}\text{O}_2$  binary is not expected to form a solid solution because of the structural instability of cubic zirconia at room temperature.

The instability of cubic zirconia at room temperature clearly contributes to the immiscibility of the Zr-bearing binaries. However, cubic zirconia can be stabilized at room temperature with the addition of trivalent or divalent cations (*e.g.*,  $\text{Y}_2\text{O}_3$ ,  $\text{CaO}$ ,  $\text{MgO}$ ). Yttria ( $\text{Y}_2\text{O}_3$ ) is the most common trivalent oxide used to stabilize zirconia, where 7-70 mol %  $\text{Y}_2\text{O}_3$  stabilizes  $\text{ZrO}_2$  in the cubic fluorite structure (Duwez et al., 1951) and the solid solution referred to as yttria-stabilized zirconia (YSZ). While the  $\text{CeO}_2\text{-ZrO}_2$  binary contains a large miscibility gap, the  $\text{CeO}_2\text{-YSZ}$  binary shows complete miscibility (Grover et al., 2007). However, based on a combination of XRD and EMPA analyses from the same study, YSZ has minimal solubility in  $\text{ThO}_2$ . Further work is necessary to understand the differences in the two systems. First, if the  $\text{Ce}^{4+}$  is reduced to  $\text{Ce}^{3+}$ , the Ce could contribute, in addition to the Y, to the stabilization of cubic zirconia. Second, the ordering of  $\text{Y}^{3+}$  and associated oxygen vacancies may influence the solid solution of  $\text{ThO}_2$  and YSZ because of the single 4+ oxidation state of both Th and Zr.

### ***Miscibility limit***

Typically, the limit of incorporation is determined based on a tangent line connecting the minima of a Gibbs free energy curve. The  $x$  values where the tangent meets the curve are the limits of incorporation. For example, the tangent to the  $\text{Th}_x\text{Ce}_{1-x}\text{O}_2$  curve at 400 K meets the curve at  $x = 0.1$  and 0.9 molar fraction of  $\text{ThO}_2$ . Thus, based solely on the Gibbs free energy of mixing, 0.1 mol% of  $\text{CeO}_2$  can be incorporated into  $\text{ThO}_2$  and 0.1 mol% of  $\text{ThO}_2$  can be incorporated into  $\text{CeO}_2$ . The minima of Gibbs free energy curves

for the  $\text{Ce}_x\text{Zr}_{1-x}\text{O}_2$  and  $\text{Th}_x\text{Zr}_{1-x}\text{O}_2$  binaries are very close to the end members; therefore, a graphical approach such as the use of a tangential line is not a reliable estimate of the incorporation limit.

The minima of the Gibbs free energy of mixing for the  $\text{Ce}_x\text{Zr}_{1-x}\text{O}_2$  and  $\text{Th}_x\text{Zr}_{1-x}\text{O}_2$  binaries are beyond the resolution of the calculations. Therefore, an estimate for the incorporation limit can be made based on an approximation of the Gibbs free energy curve,  $\Delta G_{mix}$ , which can be written in terms of  $\Delta H_{mix}$  and  $\Delta S_{mix}$  (Equation 1).  $\Delta H_{mix}$  is approximated with a symmetric Margules function [ $\Delta H_{mix} = Ax(1-x)$ ], and  $\Delta S_{mix}$  is approximated with the Stirling's approximation [ $\Delta S_{mix} = -R\{x \ln x + (1-x) \ln(1-x)\}$ ]. The  $A$  parameter is determined based on the enthalpy of mixing at the lowest concentration  $x$  calculated. For the quantum-mechanical calculations the lowest concentration is  $x = 0.125$ , while the smallest concentration possible in the Monte-Carlo simulation is  $x = 0.0005$ . This approximation becomes especially useful if only quantum-mechanical calculations are available (*e.g.*, Shuller et al., 2010a). The condition for the minimum of the  $\Delta G_{mix}$  becomes Equation 2, where the first derivative of Equation 1 is set equal to zero. The solution to Equation 2 (Equation 3) can be numerically solved using the Banach fixed point theorem.

$$\Delta G_{mix}(x) = Ax(1-x) + RT(x \ln x + (1-x) \ln(1-x)) \quad (1)$$

$$\frac{\partial}{\partial x} [Ax(1-x) + RT(x \ln x + (1-x) \ln(1-x))] = 0 \quad (2)$$

$$x = (1-x) \exp\left(\frac{-A[1-2x]}{RT}\right) \quad (3)$$

Alternatively, the limit of incorporation,  $x_{inc}$ , can be approximated based on the assumption that the  $\Delta H_{mix}$  curve is linear at low  $x$ , where  $x_{min}$  is the minimum concentration evaluated in the Monte-Carlo simulation (Ferriss et al., 2008; 2010). Again,  $\Delta G_{mix}$  is written in terms of  $\Delta H_{mix}$  and  $\Delta S_{mix}$ , where the  $\Delta H_{mix}$  term is described by a linear approximation, *i.e.*,  $\Delta H_{mix} = (\Delta H_1/x_1) \cdot x$ . The solution to the minimum of the  $\Delta G_{mix}$ , based on the linear approximation of  $\Delta H_{mix}$ , is an analytical expression (Equation 4), where  $\Delta H_1$  is the enthalpy of mixing corresponding to a specific temperature  $T$  and concentration  $x_1$ .

$$x_{inc} = \frac{e^{\left(\frac{-\Delta H_1}{X_1}\right)\left(\frac{1}{RT}\right)}}{1 + e^{\left(\frac{-\Delta H_1}{X_1}\right)\left(\frac{1}{RT}\right)}} \quad (4)$$

The estimated  $x_{inc}$  can be used to generate a temperature-composition phase diagram (Figure 3.3). The phase diagram in Figure 3.3 shows the composition  $x_{inc}$  *versus* temperature based on an average of the  $x_{inc}$  estimated by the Margules and the linear approximations. The dotted line above the average is the result from the Margules approximation, while the dotted line below the average is the result from the linear approximation. The calculated miscibility limits are significantly lower than those measured experimentally. For example, at 1400 °C (1673 K), Grover and Tyagi found 5 mol% ZrO<sub>2</sub> in ThO<sub>2</sub> and 20 mol% ZrO<sub>2</sub> in CeO<sub>2</sub> (2002), based on the refinement of unit cell parameters from powder X-ray diffraction patterns across the solid-solution. However, the calculated miscibility limit of ZrO<sub>2</sub> in ThO<sub>2</sub> and CeO<sub>2</sub> at 1673 K is 0.09

and 3.6 mol%, respectively. Similar discrepancies between calculated and measured miscibility limits were noted for solid solutions with zircon, *e.g.*,  $\text{Me}_x\text{Zr}_{1-x}\text{SiO}_4$ , where  $\text{Me} = \text{Ce}, \text{Hf}, \text{Th}, \text{U}$ , and  $\text{Pu}$  (Ferriss et al., 2010). Both computational and experimental limitations are noted as the source of possible error. Computationally, the limited number of configurations evaluated quantum-mechanically may be insufficient to capture the cation-cation interactions. Experimentally, solid-solutions may not have reached thermodynamic equilibrium. In addition, solid solutions may be exsolved on the nanoscale, such as the  $\text{Ce}_{0.5}\text{Zr}_{0.5}\text{O}_2$  nanocrystallite exsolution (Mamontov et al., 2003) described above.

## Conclusions

The thermodynamic properties of mixing, specifically the enthalpy of mixing ( $\Delta H_{mix}$ ), Gibbs free energy of mixing ( $\Delta G_{mix}$ ), and configurational entropy ( $\Delta S_{mix}$ ), were calculated for the  $\text{Th}_x\text{Ce}_{1-x}\text{O}_2$ ,  $\text{Ce}_x\text{Zr}_{1-x}\text{O}_2$ , and  $\text{Th}_x\text{Zr}_{1-x}\text{O}_2$  binaries across the complete solid solution within an isometric framework ( $Fm\bar{3}m$ ). As determined experimentally, the Th-Ce binary forms a complete solid solution, and no cation-ordering or nanoscale exsolution was observed. Below room temperature at  $x = 0.5$ , nanoscale exsolution with lamellae  $\parallel$  to  $(10\bar{2})$  are observed for the  $\text{Ce}_x\text{Zr}_{1-x}\text{O}_2$  binary. At the same conditions a complex cation ordering scheme is observed for the Th-Zr binary. Cation-ordering for the  $\text{Th}_x\text{Zr}_{1-x}\text{O}_2$  binary is unexpected due to the large miscibility gap observed in the Gibbs free energy of mixing, as well as the instability of cubic  $\text{ZrO}_2$  at room temperature.  $\text{ZrO}_2$ , however, has limited solubility for both  $\text{CeO}_2$  and  $\text{ThO}_2$ . Calculated estimates of the miscibility limit within the  $\text{Ce}_x\text{Zr}_{1-x}\text{O}_2$  and  $\text{Th}_x\text{Zr}_{1-x}\text{O}_2$  binaries are significantly lower than measured limits. This discrepancy may be reduced by further calculations in which

the ZrO<sub>2</sub> end-member is considered to be tetragonal (*P4<sub>2</sub>/nmc*) and monoclinic (*P2<sub>1</sub>/c*).

Further analysis of the complete range of Ce<sub>x</sub>Zr<sub>1-x</sub>O<sub>2</sub> and Th<sub>x</sub>Zr<sub>1-x</sub>O<sub>2</sub> solid solutions within a tetragonal and monoclinic framework are necessary in order to understand the impact of the structural stability on the solid-solution properties of these binaries.

## References

- Bukaemskiy, A.A., Barrier, D., and Modolo, G. (2009) Thermal and crystallization behaviour of ThO<sub>2</sub>-CeO<sub>2</sub> system. *Journal of Alloys and Compounds*, 485(1-2), 783-788.
- Duwez, P., Brown, F.H., and Odell, F. (1951) The zirconia-yttria system. *Journal of the Electrochemical Society*, 98(9), 356-362.
- Duwez, P., and Loh, E. (1957) Phase relationships in the system zirconia-thoria. *Journal of the American Ceramic Society*, 40(9), 321-324.
- Ferriss, E.D.A., Essene, E.J., and Becker, U. (2008) Computational study of the effect of pressure on the Ti-in-zircon geothermometer. *European Journal of Mineralogy*, 20(5), 745-755.
- Ferriss, E.D.A., Ewing, R.C., and Becker, U. (2010) Simulation of thermodynamic mixing properties of actinide-containing zircon solid solutions. *American Mineralogist*, 95(2-3), 229-241.
- Grover, V., Sengupta, P., and Tyagi, A.K. (2007) Sub-solidus phase relations in CeO<sub>2</sub>-YSZ and ThO<sub>2</sub>-YSZ systems: XRD, high temperature-XRD and EPMA studies. *Materials Science and Engineering B-Solid State Materials for Advanced Technology*, 138(3), 246-250.
- Grover, V., and Tyagi, A.K. (2002) Sub-solidus phase equilibria in the CeO<sub>2</sub>-ThO<sub>2</sub>-ZrO<sub>2</sub> system. *Journal of Nuclear Materials*, 305(2-3), 83-89.
- Kaspar, J., Fornasiero, P., and Graziani, M. (1999) Use of CeO<sub>2</sub>-based oxides in the three-way catalysis. *Catalysis Today*, 50(2), 285-298.
- Mamontov, E., Brezny, R., Koranne, M., and Egami, T. (2003) Nanoscale heterogeneities and oxygen storage capacity of Ce<sub>0.5</sub>Zr<sub>0.5</sub>O<sub>2</sub>. *Journal of Physical Chemistry B*, 107(47), 13007-13014.

- Myers, E.R. (1998) A statistical-mechanics model of ordering in aluminosilicate solid solutions. *Physics and Chemistry of Minerals*, 25(6), 465-468.
- Navrotsky, A., and Capobianco, C. (1987) Enthalpies of formation of dolomite and of magnesian calcites. *American Mineralogist*, 72(7-8), 782-787.
- Otsuka-Yao-Matsuo, S., Yao, T., and Omata, T. (2003) Thermodynamic stability of metastable tetragonal t'-Ce<sub>0.5</sub>Zr<sub>0.5</sub>O<sub>2</sub> phase in the CeO<sub>2</sub>-ZrO<sub>2</sub> system. *High Temperature Materials and Processes*, 22(3-4), 157-164.
- Pepin, J.G., and McCarthy, G.J. (1981) Phase-relations in crystalline ceramic nuclear waste forms - The system UO<sub>2+x</sub>-CeO<sub>2</sub>-ZrO<sub>2</sub>-ThO<sub>2</sub> at 1200 degrees C in air. *Journal of the American Ceramic Society*, 64(9), 511-516.
- Perdew, J.P., Burke, K., and Ernzerhof, M. (1996) Generalized gradient approximation made simple. *Physical Review Letters*, 77(18), 3865-3868.
- Reich, M., and Becker, U. (2006) First-principles calculations of the thermodynamic mixing properties of arsenic incorporation into pyrite and marcasite. *Chemical Geology*, 225(3-4), 278-290.
- Segall, M.D., Lindan, P.J.D., Probert, M.J., Pickard, C.J., Hasnip, P.J., Clark, S.J., and Payne, M.C. (2002) First-principles simulation: ideas, illustrations and the CASTEP code. *Journal of Physics-Condensed Matter*, 14(11), 2717-2744.
- Shuller, L.C., Ewing, R.C., and Becker, U. (2010a) Np-incorporation into uranyl phases: A quantum-mechanical evaluation. Submitted to *Journal of Nuclear Materials Special Issue: Spent Nuclear Fuel*.
- (2010b) Thermodynamic properties of Th<sub>x</sub>U<sub>1-x</sub>O<sub>2</sub> (0 < x < 1) based on quantum-mechanical calculations and Monte-Carlo simulations. Submitted to *Journal of Nuclear Materials*.
- Subbarao, E.C. (1981) Science and Technology of Zirconia. In A.H. Heuer, and L.W. Hobbs, Eds. *Advances in Ceramics*, 3, p. 1-24. American Ceramic Society, Westerville, OH.
- Teufer, G. (1962) Crystal structure of tetragonal ZrO<sub>2</sub>. *Acta Crystallographica*, 15(Nov), 1187-&.

- Vlaic, G., Di Monte, R., Fornasiero, P., Fonda, E., Kaspar, J., and Graziani, M. (1998) The CeO<sub>2</sub>-ZrO<sub>2</sub> system: Redox properties and structural relationships. *Catalysis and Automotive Pollution Control Iv*, 116, 185-195.
- (1999) Redox property-local structure relationships in the Rh-loaded CeO<sub>2</sub>-ZrO<sub>2</sub> mixed oxides. *Journal of Catalysis*, 182(2), 378-389.
- Yashima, M., Arashi, H., Kakihana, M., and Yoshimura, M. (1994) Raman-scattering study of cubic-tetragonal phase-transition in Zr<sub>1-x</sub>Ce<sub>x</sub>O<sub>2</sub> solid-solution. *Journal of the American Ceramic Society*, 77(4), 1067-1071.
- Yashima, M., Kakihana, M., and Yoshimura, M. (1996) Metastable-stable phase diagrams in the zirconia-containing systems utilized in solid-oxide fuel cell application. *Solid State Ionics*, 86-8, 1131-1149.

## **Chapter 4**

### **Quantum-mechanical evaluation of Np-incorporation into studtite**

#### **Abstract**

Radionuclide incorporation into the alteration products of corroded UO<sub>2</sub> in used nuclear fuel may control the release and mobility of key radionuclides, such as the very long-lived minor actinide, <sup>237</sup>Np ( $\tau_{1/2} = 2.1$  my). Studtite, [UO<sub>2</sub>(O<sub>2</sub>)(H<sub>2</sub>O)<sub>2</sub>](H<sub>2</sub>O)<sub>2</sub>, may form in the presence of peroxide produced by radiolysis of water in contact with the spent fuel. Experiments have indicated that the studtite structure can incorporate Np; however, due to the low concentrations in the solid, the incorporation mechanism could not be determined. In this study, density functional theory is used to calculate an optimized structure, determine the electronic density of states, and calculate the energetics of the incorporation of Np<sup>6+</sup> vs. Np<sup>5+</sup> + H<sup>+</sup> into the studtite structure. The definition of the source/sink phase (reference phase) for the cations involved in the incorporation process greatly affects the final incorporation energy. The incorporation energy of Np into studtite based on the 4+ oxide reference phases (e.g., source/sink = NpO<sub>2</sub>/UO<sub>2</sub>) results in lower incorporation energies (-0.07 eV and 0.63 eV for Np<sup>6+</sup> and Np<sup>5+</sup> incorporation,

respectively) than the incorporation energy calculated using higher-oxide reference phases (*e.g.*,  $\text{Np}_2\text{O}_5/\text{UO}_3$ ), where the incorporation energies for  $\text{Np}^{6+}$  and  $\text{Np}^{5+}$  into studtite are 0.42 eV and 1.12 eV, respectively. In addition,  $\text{Np}^{6+}$ -incorporation into studtite is energetically more favorable than  $\text{Np}^{5+}$ -incorporation as assessed from the lower incorporation energy. Estimates of the solid-solution behavior from a combination of quantum-mechanical calculations and Monte-Carlo simulations indicate that the  $\text{Np}^{6+}$ - and  $\text{U}^{6+}$ -studtite solid solution is completely miscible at room temperature with respect to a hypothetical  $\text{Np}^{6+}$ -studtite structure. The Np-studtite structure was calculated to be stable with respect to the corresponding oxides, but its formation may be kinetically hindered. Knowledge of the electronic structure provides insight into Np-bonding in the studtite structure. The Np 5f orbitals are within the band gap of studtite, which results in the narrow band gap of Np-incorporated studtite (1.09 eV), as compared with the band gap of studtite alone (2.29 eV).

## Introduction

Used nuclear fuel (UNF) is composed of 95-99% uranium dioxide ( $\text{UO}_2$ ) and 1-5% fission products (*e.g.*,  $^{137}\text{Cs}$ ,  $^{90}\text{Sr}$ ,  $^{99}\text{Tc}$ ) and transuranium elements, *e.g.*,  $^{239}\text{Pu}$ ,  $^{237}\text{Np}$ ,  $^{241}\text{Am}$  (Barner, 1985; Bruno and Ewing, 2006). The oxidation and corrosion of the  $\text{UO}_2$  matrix causes the oxidation and release of fission products and transuranium elements. Specific radionuclides, such as  $^{99}\text{Tc}$  or  $^{237}\text{Np}$ , are of concern due to their mobility and long half-lives. For example, Np is mobile as an aqueous  $\text{Np}^{5+}$ -complex, and  $^{237}\text{Np}$  has a half-life of 2.1 million years. Experimental corrosion studies of synthetic  $\text{UO}_2$  and natural uraninite ( $\text{UO}_{2+\chi}$ ) show a similar U-alteration paragenesis – beginning with uranyl

oxyhydroxides, followed by uranyl silicates (Finch and Ewing, 1992; Wronkiewicz et al., 1992, 1995). More recent UNF corrosion studies show the precipitation of studtite  $[\text{UO}_2(\text{O}_2)(\text{H}_2\text{O})_2(\text{H}_2\text{O})_2]$  and meta-studtite  $[\text{UO}_2(\text{O}_2)(\text{H}_2\text{O})_2]$  (Hanson et al., 2005; McNamara et al., 2005), which are the only stable uranyl peroxide minerals (Kubatko et al., 2003) and, to the authors' knowledge, the only stable peroxide minerals. Studtite has also been observed as a major alteration phase of UNF at the K East Basins of the Hanford site in Washington, United States (Abrefah et al., 1998). Studtite forms by the incorporation of peroxide (Amme, 2002), which oxidizes some of the  $\text{U}^{4+}$  to  $\text{U}^{6+}$ . The peroxide is formed due to radiolysis of water at the surface of highly radioactive UNF.

Studtite was first identified by Walenta (1973) and later the structure was determined by Burns and Hughes (2003). Studtite ( $C2/c$ ) is composed of chains of distorted uranyl hexagonal bipyramids with interstitial water (Figure 4.1). The six uranyl equatorial bonds include two unique equatorial  $\text{H}_2\text{O}$  and two symmetrically equivalent equatorial peroxide  $(\text{O}_2)^{2-}$  groups. The peroxide forms the equatorial edges that polymerize the uranyl polyhedra into chains parallel to [001].  $\text{U}^{6+}$  is also strongly bonded to axial  $\text{O}^{2-}$ , forming the linear uranyl complex. Chains of the distorted uranyl hexagonal bipyramids are weakly linked by hydrogen bonding via the interstitial water. Here, the chemical formula for studtite is written  $[(\text{UO}_2)\text{O}_2(\text{H}_2\text{O})_2](\text{H}_2\text{O})_2$ , where the  $\text{UO}_2$  signifies the uranyl molecule, the  $\text{O}_2$  is the equatorial peroxide molecule, the  $\text{H}_2\text{O}$  inside the square bracket is the equatorial water molecule, and the other  $\text{H}_2\text{O}$  is the interstitial water molecule.

While other uranyl peroxide phases have been synthesized in laboratory experiments focused on uranium(VI)-peroxide chemistry in alkaline conditions (Burns et al., 2005;

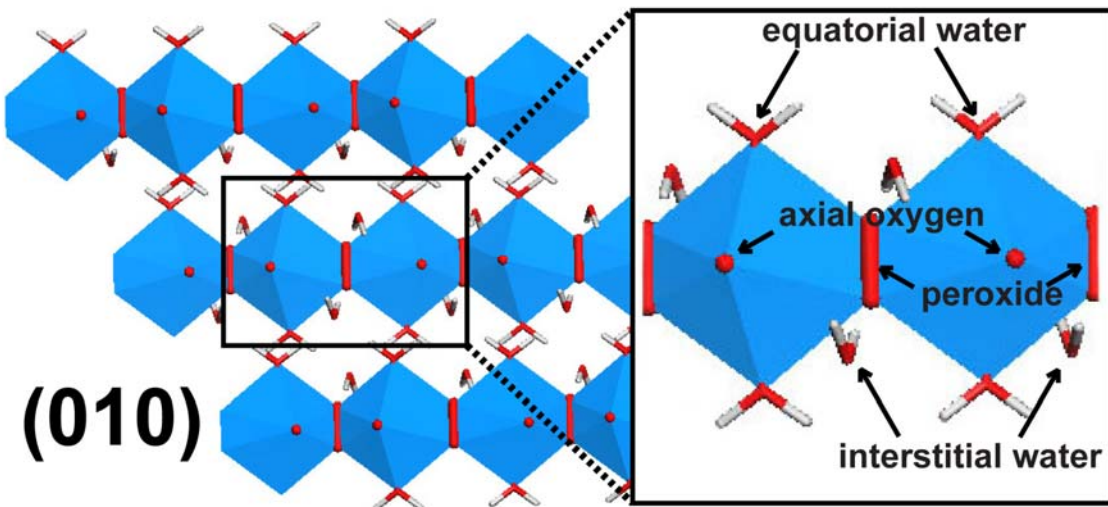


Figure 4.1. Studtite projected on the (010) showing chains of uranyl polyhedra bonded by peroxide molecules, where the unique oxygen atoms are labeled in the detailed inset of two adjacent uranyl polyhedra. U atoms = blue; O atoms = red; H atoms = white.

Kubatko and Burns, 2006; Kubatko et al., 2007), stadtite and meta-stadtite are known to be thermodynamically stable under repository conditions (Kubatko et al., 2003). These two minerals may be the first alteration phases to form in both oxidizing and reducing repository environments due to the near-surface oxidizing conditions and presence of hydrogen peroxide created by radiolysis (Amme, 2002; Cejka et al., 1996; Debets, 1963). Thus, stadtite and meta-stadtite are potentially important phases for radionuclide incorporation and retention.

The transport of radionuclides, such as Np, may be limited by incorporation into U-alteration phases (Burns et al., 1997). Electron energy loss spectroscopy (EELS) analysis shows about 500 ppm Np incorporated into the uranyl oxyhydroxide phase of dehydrated schoepite ( $\text{UO}_3(\text{H}_2\text{O})_{0.8}$ ) (Buck et al., 1997). However, EELS analysis at the Np M<sub>v</sub> energy peak is of limited value for studies of  $\text{Np}^{5+}$  because of a plural-scattering event that generates an erroneous peak at this energy (Fortner et al., 2004). Synchrotron X-ray absorption spectroscopy has been used to determine the incorporation limit of Np into uranyl oxyhydroxides and showed that there was a significantly lower concentration of Np incorporated into dehydrated schoepite (200 ppm) than the previous EELS analysis indicated (Fortner et al., 2004). Inductively coupled plasma-mass spectroscopy (ICP-MS) has also been used to study Np-incorporation into meta-schoepite ( $\text{UO}_3 \cdot 2\text{H}_2\text{O}$ ), Na-compreignacite ( $\text{Na}_2[(\text{UO}_2)_3\text{O}_2(\text{OH})_3]_2(\text{H}_2\text{O})_7$ ), uranophane ( $\text{Ca}(\text{UO}_2)_2(\text{SiO}_3\text{OH})_2(\text{H}_2\text{O})_5$ ), and  $\beta$ -( $\text{UO}_2$ )(OH)<sub>2</sub> (Burns et al., 2004). Uranyl structures with interlayer cations, such as uranophane, incorporated more Np (~400 ppm) than structures without interlayer cations, such as meta-schoepite (a few ppm). Most recently, laser ablation (LA) ICP-MS analysis has shown that Na-substituted meta-schoepite has a greater affinity for Np than meta-

schoepite (Klingensmith et al., 2007). Another experiment showed that Np has a greater affinity for studtite than for schoepite (Douglas et al., 2005a, 2005b). The oxidation state of the Np in the studtite is expected to be 5+ (Kaszuba and Runde, 1999); however, there is some speculation that  $\text{Np}^{6+}$  could be incorporated (Douglas et al., 2005a). There is also evidence that  $\text{Np}^{5+}$  and  $\text{Np}^{6+}$  can be reduced by hydrogen peroxide forming  $\text{Np}^{4+}$  (Malkova et al., 1986; Shilov et al., 1998); however, this reduction is observed in highly concentrated acid solutions and is not expected in near-neutral solutions such as those associated with geologic repository environments.

The knowledge of the crystal and electronic structure of studtite determined using quantum-mechanical calculations provides the framework for understanding potential incorporation mechanisms. This first-principles study presents a detailed description of the crystal and electronic structure of studtite and Np-substituted studtite and an analysis of the energetics of different Np-substitution mechanisms. The electronic structure of studtite is compared with the electronic structure of Np-modified studtite. Additionally, the incorporation of  $\text{Np}^{6+}$  vs.  $\text{Np}^{5+}$  into studtite is compared, and the charge-balanced incorporation mechanism of  $\text{Np}^{5+}$  into studtite is evaluated.

## Methods

### *Quantum-mechanical calculations*

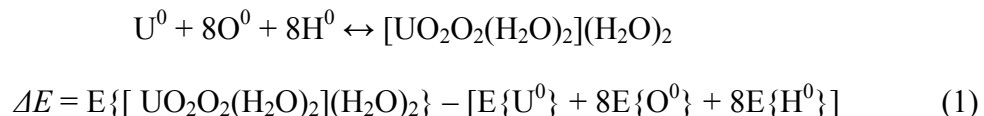
The quantum-mechanical program CASTEP (CAmbridge Serial Total Energy Package; Payne et al., 1992; Segall et al., 2002) was used to optimize the geometry of studtite and Np-substituted studtite and calculate the total energy and electronic structure of both phases. CASTEP is a density functional theory-based code that uses a planewave

approach (*i.e.*, the wavefunctions of the valence electrons are composed of a series of sinusoidal functions with different wavelengths) with periodic boundary conditions to approximate solutions to the Schrödinger equation. The total energy of a periodic system is based on the ground state of the valence electrons. Ultra-soft pseudopotentials are used to approximate the influence of the core and inner valence electrons on the outer valence electrons. Outer valence electrons (U  $5f^36s^26p^66d^17s^2$ , Np  $5f^46s^26p^66d^17s^2$ , O  $2s^22p^4$ , and H  $1s^1$ ) are treated explicitly in the Hamiltonian of the Schrödinger equation. Changing the planewave energy cut-off from 500 eV to 800 eV changed the final energy of the studtite structure by 0.99 eV and the Np<sup>6+</sup>-substituted studtite structure by 1.95 eV. Further changing the planewave energy cut-off from 800 eV to 1000 eV changed the final energy of the studtite structure by only 0.10 eV. A k-point spacing of  $0.07 \text{ \AA}^{-1}$  was used. No significant changes in energy have been found for increased k-point density; thus, this k-point grid is appropriate for this type of calculation due to the relatively large size of the unit cell. The generalized gradient approximation (GGA) with the Perdew-Burke-Ernzerhof (PBE) functional (Perdew et al., 1996) was used to approximate electron exchange and correlation. GGA has shown greater structural agreement for UO<sub>2</sub> geometry optimizations than localized density approximation (LDA) (Skomurski et al., 2006). Conventional DFT calculations predict a metallic band structure for UO<sub>2</sub>, even though UO<sub>2</sub> is a weak semi-conductor. Density functional theory approximations beyond GGA, such as the use of a Hubbard U correctional term (Anisimov, et al. 1997; Gupta et al., 2007), may be used to more accurately model the strongly correlated 5f electrons for electronic structure calculations. In the current study, GGA is used to optimize the geometry of studtite and Np-substituted studtite and qualitatively compare the

corresponding electronic structures. A spin-polarized approach is used for systems that contain  $\text{Np}^{5+}$  or  $\text{Np}^{6+}$  atoms in order to allow the unpaired electron spins in the 5f orbitals to adopt the lowest-energy configuration.

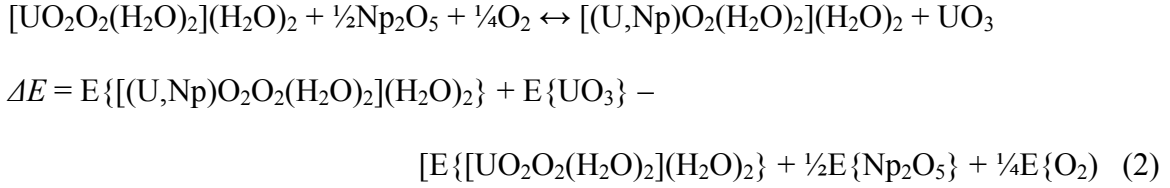
### ***Calculation of incorporation energies***

Final energies, calculated using CASTEP, are defined as the energy gained by forming a crystal from zero-valent atoms in vacuum. For example, the final energy of studtite is defined by the reaction given by Equation 1:



The energy required for the formation of studtite and  $\text{Np}^{6+}$ -substituted studtite from their respective zero-valent atoms (*e.g.*, Equation 1), indicates that studtite is more thermodynamically stable than  $\text{Np}^{6+}$ -substituted studtite by about 3.55 eV, where the energies for the zero-valent atoms were calculated for the atoms in a  $10\times 10\times 10$  Å box. The change in enthalpy describing the energy needed to form the mineral from the atoms in a gas phase is used only to compare studtite and  $\text{Np}^{6+}$ -substituted studtite – not the incorporation energy of  $\text{Np}^{6+}$  into studtite.

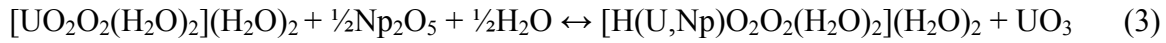
The energy required for the substitution of Np into a U site in studtite can be derived as the energy of a stoichiometric chemical reaction as shown in Equation 2, where the source for Np is  $\text{Np}_2\text{O}_5$  and the sink for U is  $\text{UO}_3$ . The incorporation energy is the difference between the sum of the reactant energies and the sum of the product energies.



The incorporation energy of Np into the unit cell of studtite, as calculated using Equation 2, depends on the reference phases (*i.e.*, source for Np and sink for U) selected. The incorporation energy is specific to a given incorporation mechanism. For example,  $\text{Np}_2\text{O}_5$ , which is the Np oxide with the highest oxidation state of Np, was selected as the source for Np in the above equation with  $\text{UO}_3$  as the uranium sink; however, the incorporation energy is different for different source and sink couples (*e.g.*,  $\frac{1}{2}\text{NpO}_2 + \frac{1}{4}\text{O}_2$  and  $\text{UO}_2$  *versus*  $\text{NpF}_6$  and  $\text{UF}_6$ ). The different reference phases were chosen to evaluate the effect of changing the cation oxidation state between the reference phase and subject phase. For example, the hexafluorides are used for  $\text{Np}^{6+}$  incorporation so that the incorporation equation can be written without changing the oxidation state of any species. This study focuses on using solid crystalline phases (oxides and fluorides) as sources and sinks for Np and U. The incorporation energies for different Np-incorporation mechanisms are used to determine the trends of favorable incorporation mechanisms.

The substitution of  $\text{Np}^{5+}$  for  $\text{U}^{6+}$  results in a charge imbalance; thus, a charge-balancing mechanism is necessary. For example, one charge-balancing mechanism is the substitution of  $\text{Np}^{5+} + \text{H}^+ \leftrightarrow \text{U}^{6+}$ , which is equivalent to the coupled substitution of  $\text{Np}^{5+} + \text{OH}^- \leftrightarrow \text{U}^{6+} + \text{O}^{2-}$ . The location of the additional  $\text{H}^+$  within the structure is very important to the outcome of the energy calculations. Due to the computational expense of evaluating all of the different substitution mechanisms in a relatively large unit cell, coarse computational parameters (planewave energy cut-off of 500 eV and  $\Gamma$  k-point)

were used in the evaluation of different H<sup>+</sup> positions within the modified studtite structure. The positions analyzed include H<sup>+</sup> bonded to the axial oxygen, the peroxide oxygen, and the interstitial water. Equation 3 shows the stoichiometric reaction that describes the coupled substitution of Np<sup>5+</sup> and H<sup>+</sup> into the studtite structure.



The incorporation energy for Np<sup>5+</sup> and H<sup>+</sup> into studtite is the difference of the sums of the products and reactants of Equation 3. The incorporation energy depends on both the reference phases and the H<sup>+</sup> position in the modified studtite structure.

#### ***Calculations of the thermodynamic properties of the (U<sup>6+</sup>,Np<sup>6+</sup>)-studtite solid solution***

The thermodynamic mixing properties for the (U<sup>6+</sup>,Np<sup>6+</sup>)-studtite solid solution are estimated from a series of quantum-mechanical calculations in which the uranium end-member is pure studtite and the neptunium end-member is a theoretical Np-studtite structure with Np<sup>6+</sup> replacing all U<sup>6+</sup> atoms. Due to the limited number of cations in the unit cell (4, limited by the computational expense of these calculations) the minimum amount of Np incorporated into the model structure is 25% of the actinyl sites. Note, the concentrations of Np in experimental studies are on the order of a few hundreds of ppm (Burns et al., 2004; Douglas et al., 2005a, 2005b; Klingensmith et al., 2007). However, quantum-mechanical calculations using lower concentrations of Np are more computationally expensive in terms of both time and memory because lower concentrations require larger unit cells. The computational time increases with number of electrons in a system cubed and is, thus, already prohibitive for a 2×1×1 supercell (which would be equivalent to a substitution of 12.5% Np into the actinyl sites). To scale up the

system, *i.e.* exploring millions of different configurations at different temperatures and compositions in a unit cell with several thousand cations, it is necessary to describe the total energy as a function of the relative positions of only the cations. The energy of the system is fit with a 2-parameter ( $W_1$  and  $W_2$ ) Margules function (Eq. 4), where  $E_0$  describes the energy of the system as a function of the concentration,  $x$ , and accounts for the asymmetry of the system (Ferriss et al., 2009). Deviations from the Margules curve are accounted for with an exchange parameter  $J$ , which describes the energy associated with the  $A$ - $B$  cation exchange (Eq. 5). Both the Margules parameters and exchange parameters are fit to the enthalpy of mixing from the quantum-mechanical calculations (Eq. 6) and used in a Monte-Carlo simulation (Becker et al., 2000; Bosenick et al., 2001; Becker and Pollock, 2002).

$$E_0 = x(1-x)[W_1x + W_2(1-x)] \quad (4)$$

$$J_{A-B}^i = E_{A-B}^i - \frac{1}{2}(E_{A-A}^i + E_{B-B}^i) \quad (5)$$

$$E_m = E_0 + \sum n_{A-B}^i J_{A-B}^i \quad (6)$$

The Monte-Carlo simulation is designed to accept a new configuration with a probability of 1 if the change in energy between the new configuration and the previous configuration is negative. Otherwise, if the exchange increases the energy ( $\Delta E$ ) of the system, the new configuration is accepted with a probability according to a Boltzmann distribution, *i.e.*, the swap is accepted if the Boltzmann factor [ $\exp(-\Delta E/RT)$ ] at a given temperature  $T$  is greater than a random number between 0 and 1 (Reich and Becker, 2006). The Monte-Carlo simulations allow for calculations using larger supercells (such

as an  $8 \times 8 \times 8$  supercell containing 2048 exchangeable cation sites). Subsequent Bogoliubov thermodynamic integration was used to calculate the temperature-dependent free energy and entropy of mixing (Yeomans, 1992; Ferriss et al., 2008).

## Results and Discussion

### *Refined crystal structure*

Quantum-mechanical calculations involve the positions of *all* of the atoms in a structure. The crystal structure of studtite has been determined using X-ray diffraction techniques, but the positions of the hydrogen atoms in studtite cannot be determined using traditional X-ray diffraction methods. Therefore, the hydrogen positions available in crystallographic databases are estimated from the O-H bond lengths (0.98 Å) combined with some consideration of bond valence constraints (Burns and Hughes, 2003). No neutron-diffraction refinements are available for the determination of the H positions; thus, in this study, energy-optimized hydrogen positions were determined using quantum-mechanical optimizations of the structure. Table 4.1 shows the experimental studtite unit cell parameters (Burns and Hughes, 2003) *versus* the optimized unit cell parameters. The optimized unit cell parameters are within ~1% of the experimentally determined unit cell parameters, with the exception of the *b* parameter, which is within ~2%. The quantum-mechanically optimized studtite unit cell volume is in close agreement (0.03%) with other the density-functional theory calculations (Ostanin and Zeller, 2007), which uses slightly different computational parameters (*e.g.*, k-point mesh,

Table 4.1. Comparison of measured unit-cell parameters and optimized unit-cell parameters of the conventional unit cell of studtite,  $(\text{Np}^{6+}_{0.25}\text{U}^{6+}_{0.75})$ -studtite, and  $(\text{Np}^{5+}_{0.25}\text{U}^{6+}_{0.75})$ -studtite.

	Experimental	Computational	Difference (%)	$(\text{Np}^{6+}_{0.25}\text{U}^{6+}_{0.75})$ - studtite	$(\text{Np}^{5+}_{0.25}\text{U}^{6+}_{0.75})$ - studtite
<i>a</i>	14.07	13.96	-0.78	13.97	13.93
<i>b</i>	6.72	6.88	2.38	6.88	6.98
<i>c</i>	8.43	8.53	1.19	8.53	8.49
$\alpha$	90.00	90.00	0.00	90.01	90.01
$\beta$	123.36	122.55	-0.66	122.40	121.92
$\gamma$	90.00	90.00	0.00	90.04	89.65
Vol.	665.7(3)	689.88	3.63	692.54	700.73

*Note:* The difference column highlights the comparison of the computed studtite parameters with those published by Burns and Hughes (2003).

planewave energy cut-off). The quantum-mechanical optimization results in the alignment of the H atoms of the equatorial water parallel to the (010) plane. Figure 4.2 shows the orientation of the water molecules pre- and post-optimization, where the alignment of the H<sup>+</sup> atoms is apparent along with a change in the dihedral angle between the planes parallel to the U-O equatorial bonds (from 12.3° to 1.2°). The quantum-mechanical calculations are static ground-state (0 K) calculations; therefore, the dynamic behavior of the water molecules at room temperature is not captured. Table 4.2 shows the quantum-mechanically optimized atomic positions and bond lengths for studtite, which have not been previously reported. The total energy difference between the initial structure, using the estimated H positions proposed by Burns and Hughes (2003), and the optimized structure is -129.8 kJ/mol formula unit, where the formula unit is [(UO<sub>2</sub>)(O<sub>2</sub>)(H<sub>2</sub>O)<sub>2</sub>](H<sub>2</sub>O)<sub>2</sub>. The significant decrease in total energy of the optimized primitive cell with respect to the initial primitive cell is evidence that the optimized H positions are energetically favored. Additionally, the enthalpy of formation of studtite from UO<sub>3</sub> + H<sub>2</sub>O<sub>2</sub> + 3 H<sub>2</sub>O yields ΔE = -74.2 kJ/mol, which is in close agreement with the measured enthalpy of formation (-75.7 kJ/mol, Kubatko et al., 2003).

The Np<sup>6+</sup>-substituted structure is isostructural with studtite and was constructed by substituting Np<sup>6+</sup> for U<sup>6+</sup> in one of the four actinyl polyhedra (25 atomic % Np). The (Np<sup>6+</sup><sub>0.25</sub>U<sup>6+</sup><sub>0.75</sub>)-studtite is optimized using *P1* symmetry in order to avoid symmetry restrictions in the relaxation process. The optimized unit cell volume is 692.54 Å<sup>3</sup> (optimized studtite volume = 689.88 Å<sup>3</sup>). The optimized unit cell parameters of

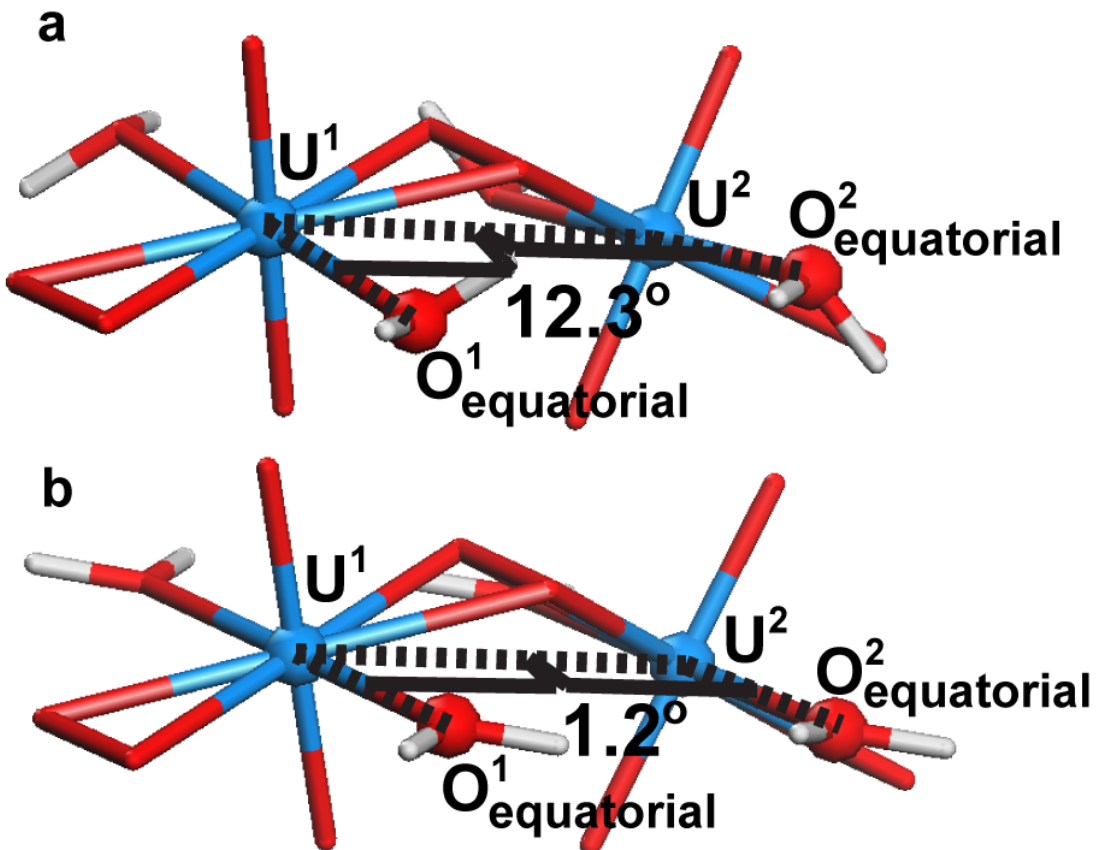


Figure 4.2. The pre- (a) and post- (b) optimized uranyl polyhedra show the alignment of the  $H^+$  parallel to the (010) plane and the change in the dihedral angle between the planes parallel to the  $U^i$ - $O^i_{\text{equatorial}}$  bonds (traced with dotted lines). Calculations are performed with ground-state (0 K) static conditions; therefore, vibrations of the water molecules at room temperature are not observed. U atoms = blue; O atoms = red; H atoms = white.

Table 4.2. Optimized unit-cell parameters, fractional atomic coordinates, and bond distances and angles for studtite.

studtite $[(\text{UO}_2)\text{O}_2(\text{H}_2\text{O})_2](\text{H}_2\text{O})_2$				
$a (\text{\AA}) = 13.96; b (\text{\AA}) = 6.88; c (\text{\AA}) = 8.53; \beta (\text{\\circ}) = 122.55$				
Vol. ( $\text{\AA}^3$ ) = 689.88; space group = $C2/c$				
Element	Atom no.	x	y	z
U	1	0.000	0.000	0.000
O <sub>uranyl (ur)</sub>	2	-0.004	-0.247	0.072
O <sub>peroxide (per)</sub>	3	0.062	0.121	0.305
O <sub>equatorial (eq)</sub>	4	0.205	0.004	0.181
O <sub>interstitial (int)</sub>	5	-0.159	-0.523	0.052
H <sup>1</sup> <sub>equatorial</sub>	6	0.256	0.005	0.132
H <sup>2</sup> <sub>equatorial</sub>	7	0.254	0.018	0.320
H <sup>1</sup> <sub>interstitial</sub>	8	-0.119	-0.648	0.104
H <sup>2</sup> <sub>interstitial</sub>	9	-0.102	-0.423	0.076
Bond distances ( $\text{\AA}$ ) and angles ( $\text{\\circ}$ )				
U-O <sub>ur</sub>	1.818	O <sub>ur</sub> -U-O <sub>ur</sub>	180	
U-O <sup>1</sup> <sub>per</sub>	2.400	O <sup>1</sup> <sub>per</sub> -O <sup>2</sup> <sub>per</sub>	1.459	
U-O <sup>2</sup> <sub>per</sub>	2.406			
U-O <sub>eq</sub>	2.412			
O <sub>eq</sub> -H <sup>1</sup> <sub>eq</sub>	1.005	H <sup>1</sup> <sub>eq</sub> ...O <sub>int</sub>	1.668	O <sub>eq</sub> -H <sup>1</sup> <sub>eq</sub> ...O <sub>int</sub>
O <sub>eq</sub> -H <sup>2</sup> <sub>eq</sub>	1.001	H <sup>2</sup> <sub>eq</sub> ...O <sub>int</sub>	1.675	O <sub>eq</sub> -H <sup>2</sup> <sub>eq</sub> ...O <sub>int</sub>
H <sup>1</sup> <sub>eq</sub> -O <sub>eq</sub> -H <sup>2</sup> <sub>eq</sub>	108			173
O <sub>int</sub> -H <sup>1</sup> <sub>int</sub>	0.991	H <sup>1</sup> <sub>int</sub> ...O <sub>per</sub>	1.760	O <sub>int</sub> -H <sup>1</sup> <sub>int</sub> ...O <sub>per</sub>
O <sub>int</sub> -H <sup>2</sup> <sub>int</sub>	0.986	H <sup>2</sup> <sub>int</sub> ...O <sub>ur</sub>	1.841	O <sub>int</sub> -H <sup>2</sup> <sub>int</sub> ...O <sub>ur</sub>
H <sup>1</sup> <sub>int</sub> -O <sub>int</sub> -H <sup>2</sup> <sub>int</sub>	108			168

$(\text{Np}^{6+}_{0.25}\text{U}^{6+}_{0.75})$ -substituted studtite are listed in Table 4.1. A CIF file for the optimized atomic positions of  $(\text{Np}^{6+}_{0.25}\text{U}^{6+}_{0.75})$ -studtite is located in Appendix 1. This shows that the unit cell parameters are not more than 0.01 Å different from those of pure U-studtite.

The unit cell parameters of  $[(\text{Np}^{5+}\text{H}^+)_{0.25}\text{U}^{6+}_{0.75}]$ -structure diverge by not more than 0.1 Å from studtite. The substituted  $\text{Np}^{5+}$  is slightly displaced from the original  $\text{U}^{6+}$  position due to the coupled substitution of an  $\text{H}^+$  ion for charge-balance. Different locations for the  $\text{H}^+$  were considered – *i.e.*, bonded to the axial oxygen, to the peroxide oxygen, and to the interstitial water molecule. The most thermodynamically stable position occurs for  $\text{H}^+$  is bonded to the axial  $\text{O}^{2-}$ , which is energetically more favorable than the other positions by 0.8-1.3 eV. The unit cell volume for  $[(\text{Np}^{5+}\text{H}^+)_{0.25}\text{U}^{6+}_{0.75}]$ -structure is 700.73 Å<sup>3</sup>, which is 1.6% larger than studtite and 1.2% larger than  $[\text{Np}^{6+}_{0.25}\text{U}^{6+}_{0.75}]$ -structure. The optimized unit cell parameters of  $[(\text{Np}^{5+}\text{H}^+)_{0.25}\text{U}^{6+}_{0.75}]$ -structure are listed in Table 4.1. The quantum-mechanically optimized atomic positions for  $[(\text{Np}^{5+}\text{H}^+)_{0.25}\text{U}^{6+}_{0.75}]$ -structure are available as a CIF file in Appendix 2.

### ***Electronic structure of studtite***

The electronic-structure analysis of studtite can be described using the partial density of states (PDOS) and orbital projections. The DOS of the valence electrons for studtite are shown for electron binding energies from -30 eV to +10 eV in Figure 4.3. The inner valence band (from about -24 eV to -10 eV) has electron density contributions from the axial O 2s, peroxide O 2s, equatorial water O 2s, and U 6p orbitals. Each peak in this inner valence band (interval A) is labeled in Figure 4.3.

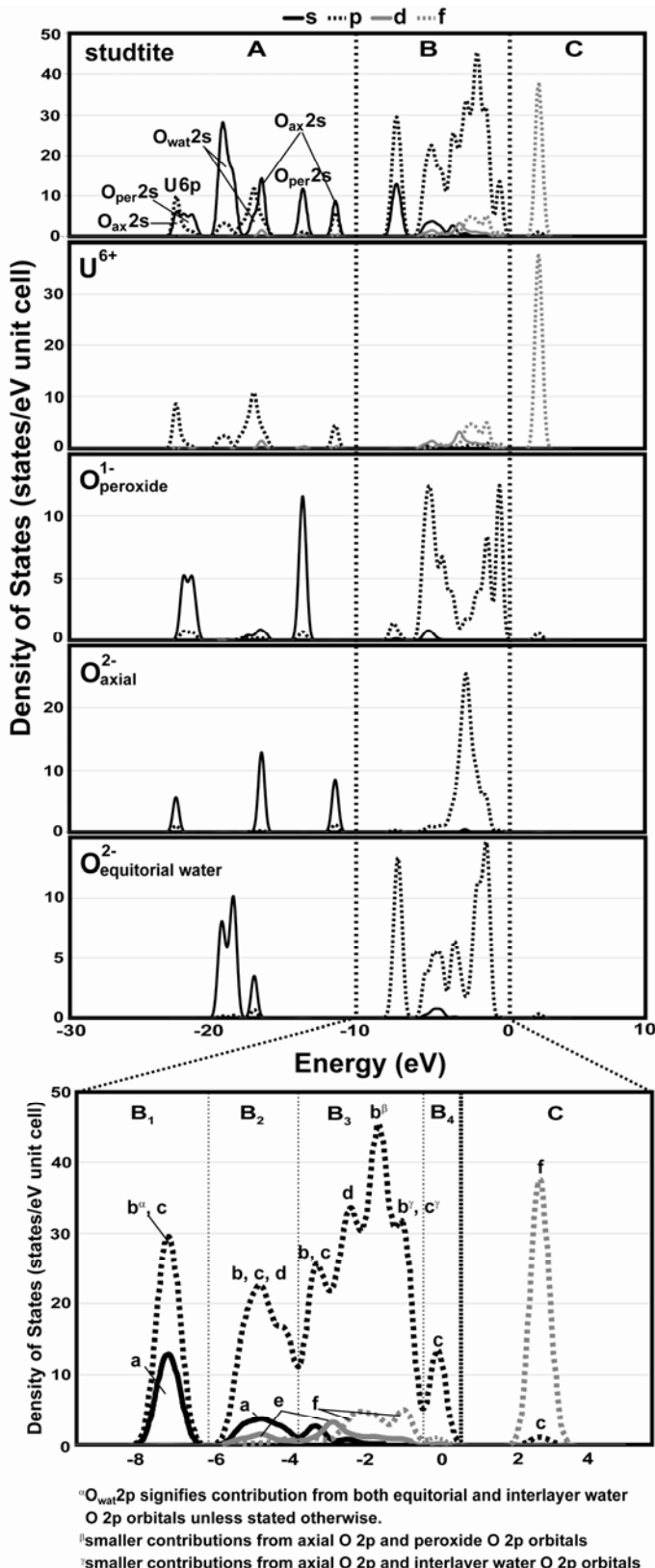


Figure 4.3. Partial density of states spectra of studtite over the entire calculated energy range, where interval A designates the inner valence band, interval B the outer valence band and interval C the conduction band. The peaks in interval A of the full studtite PDOS are labeled according to the contributing molecular orbitals. The peak character of the outer valence band and conduction band are detailed in the inset, which is divided into intervals B<sub>1</sub>, B<sub>2</sub>, B<sub>3</sub>, B<sub>4</sub>, and C. These intervals are discussed in detail in the text. a = H<sub>wat</sub> 1s; b = O<sub>wat</sub> 2p; c = O<sub>per</sub> 2p; d = O<sub>ax</sub> 2p; e = U 6d; f = U 5f.

The outer valence band of the studtite electronic structure (from about -10 eV to 0 eV; interval B Figure 4.3) is divided into 4 intervals (interval B<sub>1</sub>-B<sub>4</sub> in inset of Figure 4.3). The lowest interval has contributions from the interstitial water O 2p, equatorial water O 2p, and the peroxide O 2p. The bonding orbitals within the water molecules, as well as hydrogen bonding between the interstitial water molecules and the uranyl polyhedra chains via the peroxide O 2p orbitals, are shown in the electron density orbital projection in this energy range (Figure 4.4). The next interval, -6 eV to -4 eV, has some contribution from all of the unique oxygen 2p orbitals. The U 6d is strongly correlated with both the equatorial water O 2p and peroxide O 2p orbitals.

The interval from -4 eV to -1 eV has 4 major peaks and shows the strongest correlation between the U 6d and 5f orbitals and the peroxide O 2p, axial O 2p, and equatorial water O 2p orbitals. The -3.5 eV peak is comprised of the interstitial water O 2p, equatorial water O 2p, and the peroxide O 2p orbitals. The -2.5 eV peak is comprised primarily of the axial O 2p orbital. The -2 eV peak is comprised primarily of both the water O 2p orbitals, with smaller contributions from the axial and peroxide O 2p orbitals. Finally, the -1 eV peak is comprised primarily of the peroxide O 2p and the equatorial water O 2p peak, with smaller contributions from the axial O 2p and interstitial water O 2p orbitals. The top of the valence band and just past the Fermi level, from -0.5 eV to 0.5 eV, has contributions solely from the peroxide O 2p orbital. Thus, the highest occupied molecular orbital (HOMO) is composed of electron density contributions from the peroxide O 2p orbital, which may play a role in processes, such as actinide incorporation into the uranyl structure and possible oxidation reactions in the environment. The peroxide O 2p electron density contribution at the HOMO level of the studtite electronic

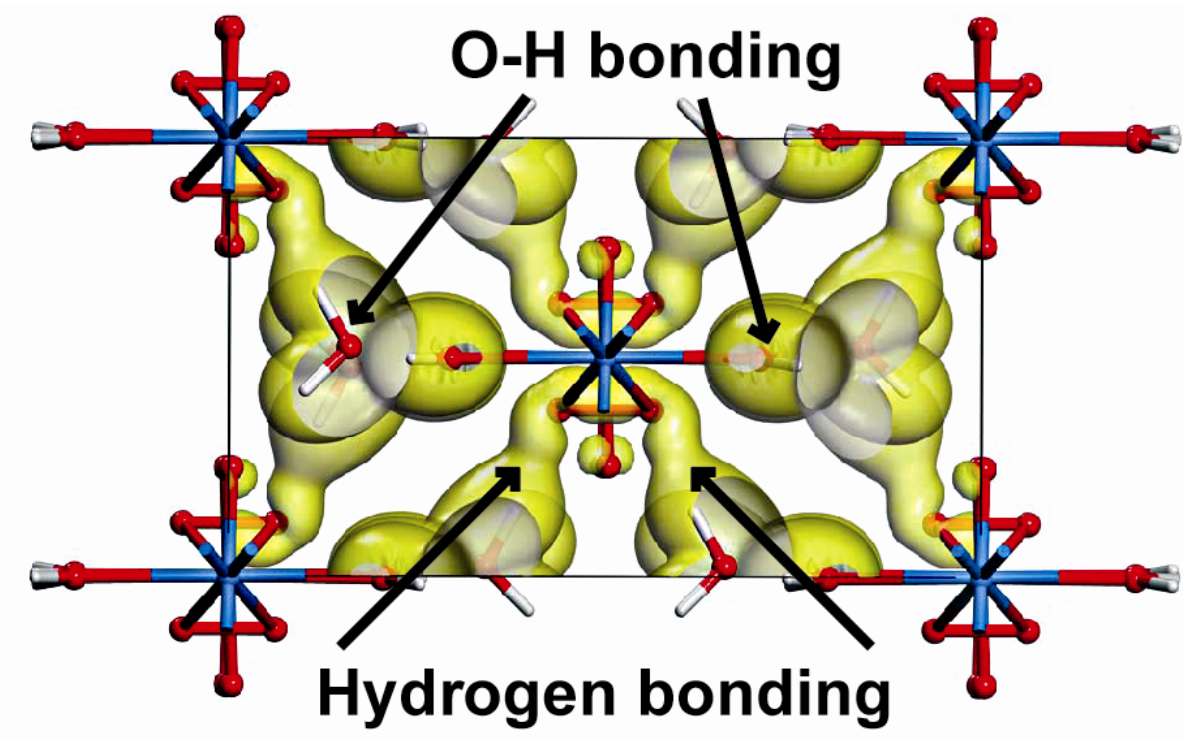


Figure 4.4. Electron density orbital projection between -8 and -6 eV showing O-H bonding in water molecules as well as hydrogen bonding between the water molecules and uranyl polyhedra.

structure is unique to studtite, as studtite is the only thermodynamically stable uranyl peroxide mineral (Kubatko et al., 2003).

As compared with the valence band, the lower conduction band (no higher empty conduction bands are considered in these calculations because they change neither the geometry nor the energetics of the system significantly) is much simpler. The unoccupied U 5f orbitals are the major contribution to the density of states in this region with an admixture of peroxide O 2p and minimal contribution from the axial O 2p orbitals (Figure 4.3).

The significant peaks, in particular the peroxide contribution to electron density in the HOMO and the U 5f contribution to the electron density in the LUMO, are comparable to the studtite electronic structure calculation by Ostanin and Zeller (2007). The calculated band gap is 2.29 eV, which compares to the band gap calculated by Ostanin and Zeller (2.3 eV). This lowest-energy HOMO-LUMO transition occurs at the F k-point (0, 0.5, 0) in the studtite *P1* Brillouin zone.

### ***Electronic structure of $(\text{Np}^{6+}_{0.25}\text{U}^{6+}_{0.75})$ -studtite***

The  $(\text{Np}^{6+}_{0.25}\text{U}^{6+}_{0.75})$ -studtite electronic structure is also described using the density of states and electron density projections, along with the band structure. The DOS for the  $(\text{Np}^{6+}_{0.25}\text{U}^{6+}_{0.75})$ -studtite is similar to that of studtite (Figure 4.5); however, there are additional unique types of atom/position combinations that must be considered. In studtite, four different oxygen types are unique: peroxide, axial (or uranyl), equatorial (U-bonded) water, and interstitial water; while in  $(\text{Np}^{6+}_{0.25}\text{U}^{6+}_{0.75})$ -studtite, seven different oxygen types are unique: Np-bonded peroxide, U-bonded peroxide, neptunyl, uranyl,

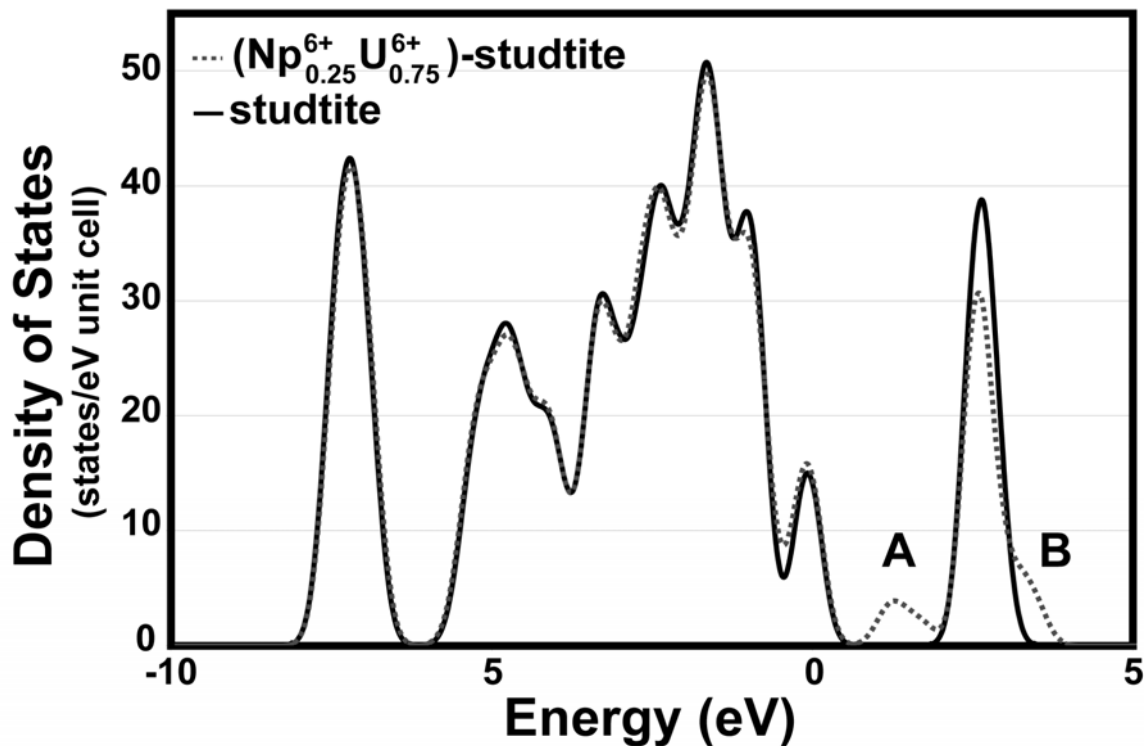


Figure 4.5. Comparison of the total DOS for studtite (solid curve) and  $(\text{Np}^{6+}_{0.25}\text{U}^{6+}_{0.75})$ -studtite (dotted curve). Peak A has electron density contribution from the Np 5f orbital of the  $(\text{Np}^{6+}_{0.25}\text{U}^{6+}_{0.75})$ -studtite and is located within the energy region of the studtite band gap. The tail on the highest energy peak (B) is due to the split Np 5f peaks from the  $(\text{Np}^{6+}_{0.25}\text{U}^{6+}_{0.75})$ -studtite.

Np-bonded equatorial water, U-bonded equatorial water, and interstitial water. The increase in the number of unique O types is due to the change in the bonding environment for an O bonded to a U atom *versus* an Np atom, which is primarily due to Np<sup>6+</sup> having an extra unpaired 5f electron, while U has no 5f electrons.

From the PDOS, two main differences are observed between studtite and (Np<sup>6+</sup><sub>0.25</sub>U<sup>6+</sup><sub>0.75</sub>)-studtite (labeled in Figure 4.5). Note that the difference in peak intensity between the spectra is not major, because the intensity is based on the number of electrons explicitly included in the calculation. The (Np<sup>6+</sup><sub>0.25</sub>U<sup>6+</sup><sub>0.75</sub>)-studtite unit cell has one more valence electron than the studtite unit cell from the substitution of Np (Z = 93) for U (Z = 92), which increases the number of valence electrons explicitly included in the calculation from 280 to 281 total valence electrons in the unit cell. One major difference between the PDOS of studtite and (Np<sup>6+</sup><sub>0.25</sub>U<sup>6+</sup><sub>0.75</sub>)-studtite is the width of the band gap. While the smallest width of the band gap for (Np<sup>6+</sup><sub>0.25</sub>U<sup>6+</sup><sub>0.75</sub>)-studtite is at the same point within Brillouin zone as for studtite (F k-point), the magnitude is smaller (1.09 eV) (Figure 4.6). The electron contributions that occupy the energy states within the studtite band gap are from unoccupied Np 5f orbitals. Another major difference between studtite and (Np<sup>6+</sup><sub>0.25</sub>U<sup>6+</sup><sub>0.75</sub>)-studtite is the presence of a tail on the highest energy peak in the (Np<sup>6+</sup><sub>0.25</sub>U<sup>6+</sup><sub>0.75</sub>)-studtite PDOS due to the extra empty bands used in the (Np<sup>6+</sup><sub>0.25</sub>U<sup>6+</sup><sub>0.75</sub>)-studtite calculation for the spin optimization of the unpaired Np 5f electron (Figure 4.5).

The subtle differences of the electronic structure caused by the incorporation of Np into the studtite structure are better understood through the comparison of the electron density contribution from Np, Np-neighboring U, and U-neighboring U, as well as the Np-bonded peroxide O and U-bonded peroxide O in the (Np<sup>6+</sup><sub>0.25</sub>U<sup>6+</sup><sub>0.75</sub>)-studtite

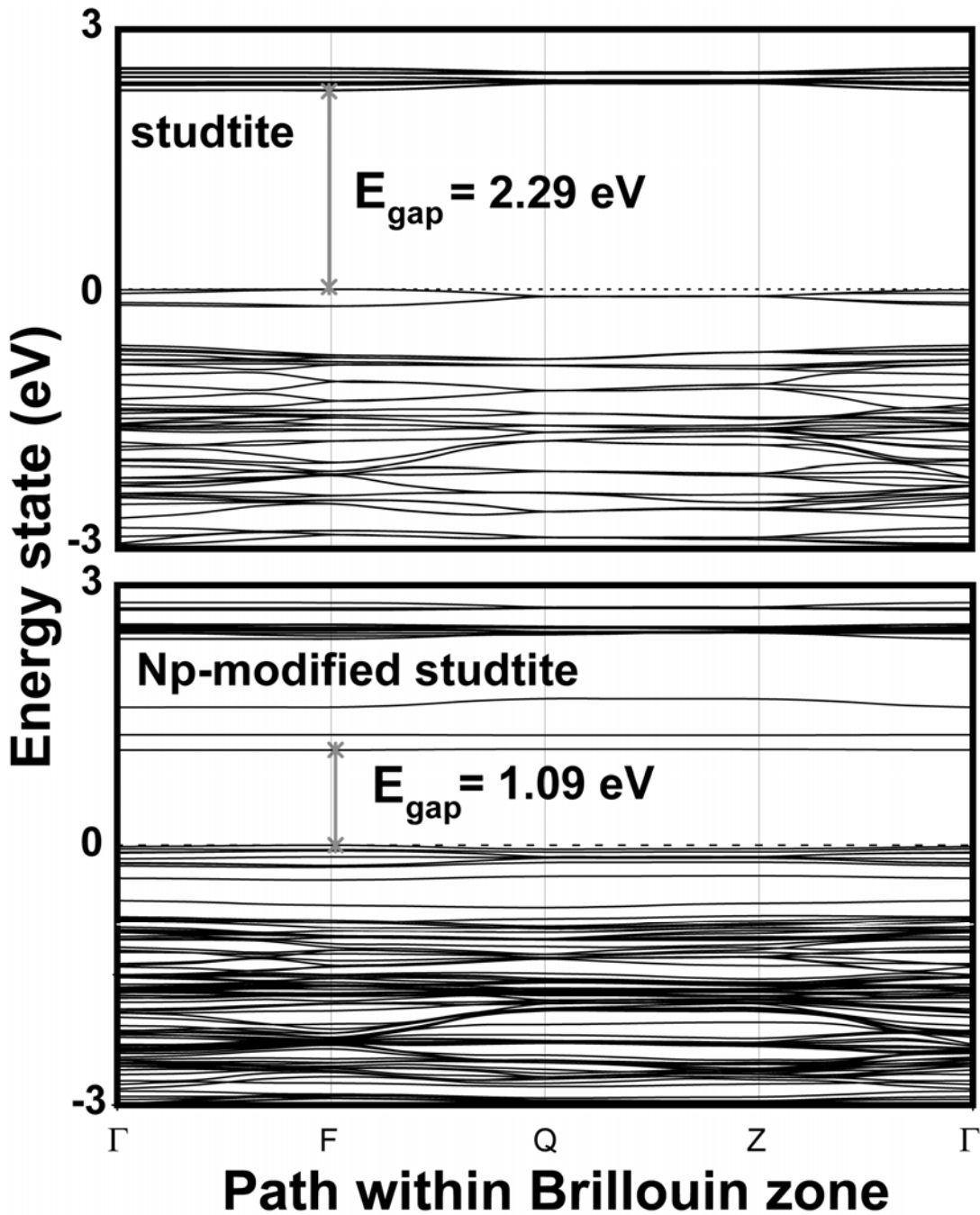


Figure 4.6. Band structure showing the band gap of studtite ( $E_{gap} = 2.29 \text{ eV}$ ) and  $(\text{Np}^{6+}_{0.25}\text{U}^{6+}_{0.75})$ -studtite ( $E_{gap} = 1.09 \text{ eV}$ ), where the letters (k-points) on the x-axis signify a point within the Brillouin zone,  $\Gamma$  (0, 0, 0); F (0, 0.5, 0); Q (0, 0.5, 0.5); Z (0, 0, 0.5).

structure (Figure 4.7 and Figure 4.8, respectively). The different contribution to the DOS in this region are best explained by considering the energy states between -10 eV and 5 eV, as the regions closest to the HOMO and LUMO levels are involved in electron transfer.

The main differences in the valence and conduction band are associated with the electron density contribution from the U and Np 5f orbitals. The differences in peak intensity are attributed to the number of total U and Np valence electrons.

(Np<sup>6+</sup><sub>0.25</sub>U<sup>6+</sup><sub>0.75</sub>)-studtite contains 3 U and 1 Np, which means that 42 U electrons and 15 Np valence electrons are calculated explicitly. Therefore, an energy state with equal contributions from Np and U orbitals will appear to have a greater contribution from the U (both Np-neighboring and U-neighboring) by a ratio of 14:5. In the conduction band (0.5 and 2.0 eV), as well as in the top of the valence band (~0.5 eV), the major contributor to the electron density is the Np 5f orbital, which is the most significant difference between the Np<sup>6+</sup> and U<sup>6+</sup> electron density in the (Np<sup>6+</sup><sub>0.25</sub>U<sup>6+</sup><sub>0.75</sub>)-studtite bonding environment. Between 2 and 4 eV, the U-neighboring U and Np-neighboring U 5f orbital has most of the density contribution, as evidenced from the single strong PDOS peak. In the same range, additional Np f-orbital peaks are observed due to the inclusion of more empty energy bands in the calculation. The extra empty bands were included to allow for the spin optimization due to the unpaired 5f electron of the Np<sup>6+</sup> in the modified studtite structure.

The density contributions from the U-bonded O and the Np-bonded O are similar at lower energy states, but show different behaviors in the conduction band. Between 0.5 and 2 eV, only the peroxide O linking the Np- and U-polyhedra contribute to the electron

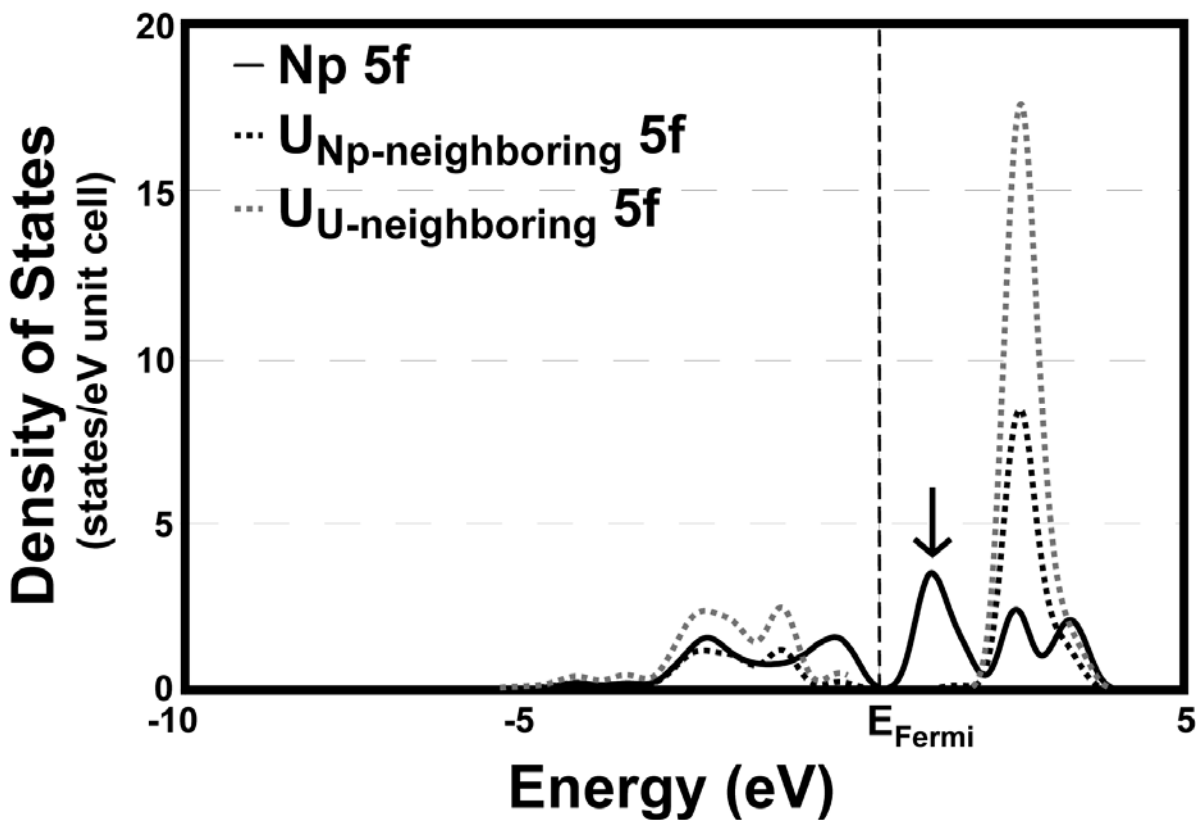


Figure 4.7. PDOS of  $(\text{Np}^{6+}_{0.25}\text{U}^{6+}_{0.75})$ -studtite highlighting the 5f orbital contribution from the Np in the peroxide chain, Np-neighboring U in the peroxide chain, and U-neighboring U in the peroxide chain, where the arrow points to the unoccupied Np 5f orbital that is in the studtite band gap.

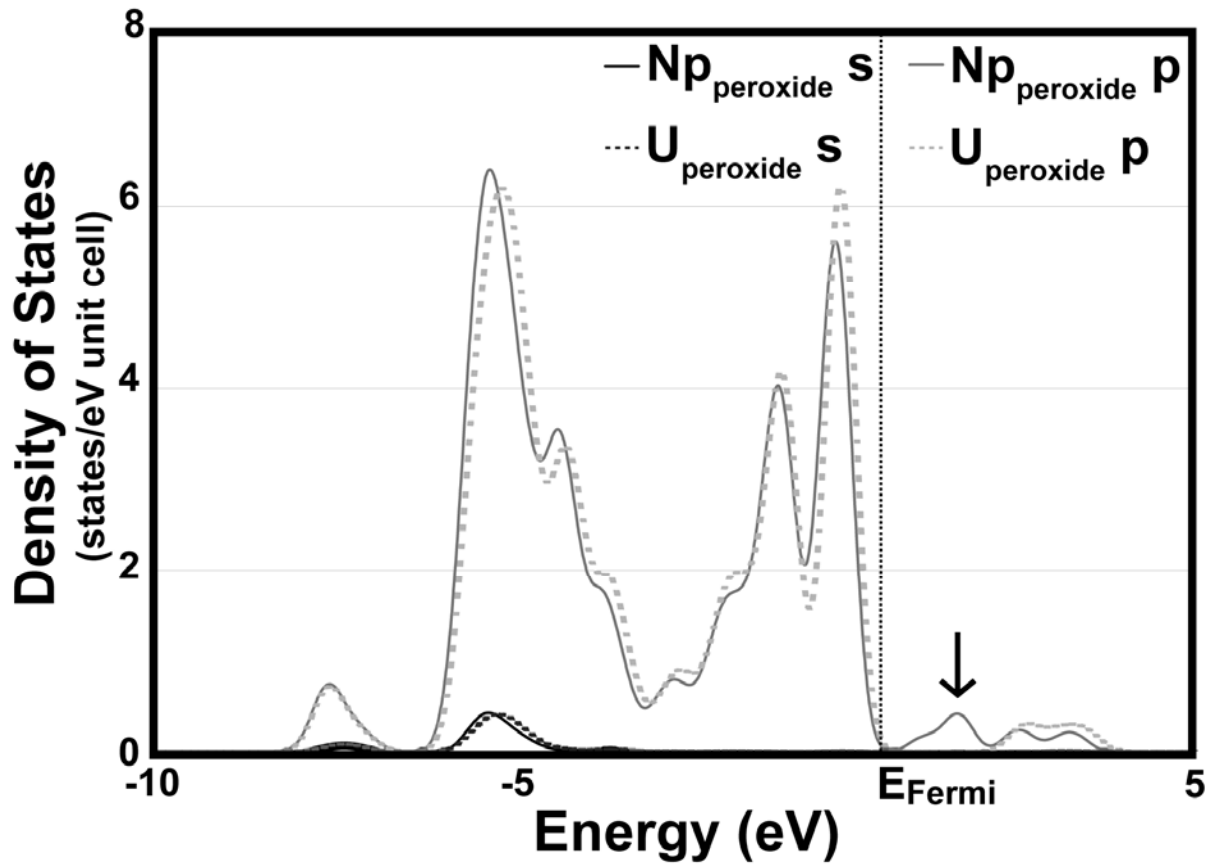


Figure 4.8. PDOS of  $(\text{Np}^{6+}_{0.25}\text{U}^{6+}_{0.75})$ -studtite highlighting the 2s and 2p orbital contribution from the Np-bonded and U-bonded peroxide oxygen, where the arrow points to the Np-bonded peroxide 2p contribution that is in the studtite band gap.

density, while the peroxide O linking two U-polyhedra do not (Figure 4.8). This is the same energy state mentioned in the previous section, where the Np 5f orbital contributes to the partial density of states, while the U 5f orbital does not. The peroxide could be important for the control of the oxidation state of incorporated species. For example, the amount of Np incorporated into studtite has been experimentally determined; however, the oxidation state of the Np (5+ vs. 6+) was not determined (Douglas et al., 2005a). The oxidation of Np from 5+ to 6+ during incorporation into the studtite structure may be facilitated by the peroxide. The smaller band gap of  $(\text{Np}^{6+}_{0.25}\text{U}^{6+}_{0.75})$ -studtite as compared with studtite, as evidenced from the Np-studtite DOS, indicates that less energy is needed to excite an electron from the valence band to the conduction band for Np-doped studtite, as compared with studtite. Thus,  $(\text{Np}^{6+}_{0.25}\text{U}^{6+}_{0.75})$ -studtite may be more sensitive to redox conditions during bulk dissolution.

### ***Thermodynamics of Np-incorporation into studtite***

The incorporation energy for the substitution of one  $\text{Np}^{6+}$  for one  $\text{U}^{6+}$  or one  $\text{Np}^{5+}$  and  $\text{H}^+$  for one  $\text{U}^{6+}$  in studtite is the difference between the sum of the final enthalpies of the products minus the sum of the final enthalpies of the reactants from a stoichiometric reaction describing the incorporation mechanism (*e.g.*, Equation 2). The source for Np and sink for U are strategically chosen, as shown by the comparison using binary-oxide reference phases and hexafluoride reference phases (*e.g.*, Table 4.3 Equations 1 and 5, respectively). The oxide reference phase sources for Np are  $\text{NpO}_2$  and  $\text{Np}_2\text{O}_5$ , while the sinks for U are  $\text{UO}_2$  and  $\text{UO}_3$ , where Np is in the 4+ and 5+ oxidation state and U is in the 4+ and 6+ oxidation state. Incorporation reactions are balanced using appropriate

Table 4.3. Incorporation equations and energies for  $\text{Np}^{6+}$  in studtite with various reference phases.

Reactants	$\rightleftharpoons$	Products	E (eV)
1 studtite + $\frac{1}{2}\text{Np}_2\text{O}_5 + \frac{1}{4}\text{O}_2$	$\rightleftharpoons$	(studtite - $\text{U}^{6+} + \text{Np}^{6+}$ ) + $\text{UO}_3$	0.42
2 studtite + $\frac{1}{2}\text{Np}_2\text{O}_5$	$\rightleftharpoons$	(studtite - $\text{U}^{6+} + \text{Np}^{6+}$ ) + $\text{UO}_2 + \frac{1}{4}\text{O}_2$	2.28
3 studtite + $\text{NpO}_2 + \frac{1}{2}\text{O}_2$	$\rightleftharpoons$	(studtite - $\text{U}^{6+} + \text{Np}^{6+}$ ) + $\text{UO}_3$	-0.07
4 studtite + $\text{NpO}_2$	$\rightleftharpoons$	(studtite - $\text{U}^{6+} + \text{Np}^{6+}$ ) + $\text{UO}_2$	1.79
5 studtite + $\text{NpF}_6$	$\rightleftharpoons$	(studtite - $\text{U}^{6+} + \text{Np}^{6+}$ ) + $\text{UF}_6$	-0.10

amounts of O<sub>2</sub> and, in the case of Np<sup>5+</sup> incorporation, H<sub>2</sub>O. The difference between Np-incorporation energies for the cases in which the U sink is UO<sub>3</sub> and the Np source is either NpO<sub>2</sub> or Np<sub>2</sub>O<sub>5</sub> (*i.e.*, the difference between reactions 3 and 1 in Table 4.3) is equal to the enthalpy of formation of Np<sub>2</sub>O<sub>5</sub> via the following reaction: NpO<sub>2</sub> + O<sub>2</sub> → ½Np<sub>2</sub>O<sub>5</sub> (-0.49 eV). The formation of ½Np<sub>2</sub>O<sub>5</sub> is favorable with respect to NpO<sub>2</sub> and ½O<sub>2</sub>, which is supported by the synthesis of Np<sub>2</sub>O<sub>5</sub> at low temperature from aqueous NpO<sub>2</sub><sup>+</sup> on calcite crystals in O<sub>2</sub>-saturated solutions (Forbes et al., 2007), as well as the formation of Np<sub>2</sub>O<sub>5</sub> on NpO<sub>2</sub> films reacted with atomic oxygen (Seibert et al., 2009). In addition, the experimentally measured enthalpy of formation of Np<sub>2</sub>O<sub>5</sub> is -2162.7 kJ/mol (-22.4 eV), which is significantly lower in energy than that of NpO<sub>2</sub> (-1074.0 kJ/mol; -11.1 eV) (Guillaumont et al., 2003). The measured enthalpy of formation of ½Np<sub>2</sub>O<sub>5</sub> from NpO<sub>2</sub> and ½O<sub>2</sub> is -7.4 kJ/mol (Robie and Hemingway, 1995), which is very different from the calculated results (-47.4 kJ/mol). The consideration of a few possible sources of error brings the values into better agreement. First, the enthalpy of formation of O<sub>2</sub> is 0; however, computationally, some enthalpy contributes to the formation equation described above because the energy of O<sub>2</sub> in a box is that of O<sup>0</sup> + O<sup>0</sup> → O<sub>2</sub>. Thus, a PdV term for the O<sub>2</sub> (2.2 kJ/mol) can be added to the experimental value. In addition, Np<sub>2</sub>O<sub>5</sub> was calculated with an antiferromagnetic spin configuration, which was 10.6 kJ/mol more energetically favorable than the ferromagnetic spin configuration. Magnetic susceptibility data for polycrystalline Np<sub>2</sub>O<sub>5</sub> indicates a transition from antiferromagnetic to ferromagnetic coupling of the Np moments at ~22 K and a subsequent transition from ferromagnetic to paramagnetic above 50 K. Thus, the Np<sub>2</sub>O<sub>5</sub> spin configuration would have been paramagnetic for the experimental enthalpy measurement. Finally, the Np<sub>2</sub>O<sub>5</sub>

used for enthalpy measurements may not have had high crystallinity (Lemire et al., 2001), which could account for other differences between the computational and experimental enthalpy of formation.

Similarly, the difference between incorporation energies for the cases in which the Np source is  $\text{Np}_2\text{O}_5$  and the U sink is either  $\text{UO}_2$  or  $\text{UO}_3$  is equal to the enthalpy of formation of the following reaction:  $\text{UO}_2 + \frac{1}{2}\text{O}_2 \rightarrow \text{UO}_3$ . The measured enthalpy of formation of  $\text{UO}_3$  from  $\text{UO}_2$  and  $\frac{1}{2}\text{O}_2$  is -138.9 kJ/mol (Robie and Hemingway, 1995), which is in relatively good agreement with the calculated results (-179.9 kJ/mol).

The hexafluoride reference phase used for  $\text{Np}^{6+}$  is  $\text{NpF}_6$ , while the corresponding sink for  $\text{U}^{6+}$  is  $\text{UF}_6$ , which is commonly used to manufacture nuclear fuel. Both  $\text{UF}_6$  and  $\text{NpF}_6$  are orthorhombic (*Pnma*), with slightly varying unit-cell parameters, thus the chemistry and bonding environment for both phases are similar; therefore, the energy difference between the two is primarily due to the additional 5f electron of Np. The hexafluoride phases, however, are molecular crystals, and quantum-mechanical density functional theory calculations do not capture the van der Waals bonding in molecular crystals very accurately. The optimized unit cell parameters of the bulk hexafluoride structures are ~10% greater than the experimentally determined unit cell parameters.

The relative stability of the cation reference phases (*i.e.*, source for Np and sink for U) affects the final incorporation energy significantly. The lowest incorporation energy is observed for the balanced equation in which the actinide source phase is the least stable with respect to other possible reference phases. For example, the incorporation energy calculated with  $\text{NpO}_2$  is lower than the incorporation energy calculated with  $\text{Np}_2\text{O}_5$  because  $\text{NpO}_2$  (and  $\text{O}_2$ ) is less stable with respect to  $\text{Np}_2\text{O}_5$ ; thus, it is easier to

incorporate the Np from  $\text{NpO}_2$  into studtite. Similarly, the incorporation energy calculated with  $\text{UO}_3$  is lower than the incorporation energy calculated with  $\text{UO}_2$  because  $\text{UO}_3$  is stable with respect to  $\text{UO}_2$  and is included in the right side of the incorporation equation; thus,  $\text{UO}_3$  as a sink for U is favored.

The incorporation energy of  $\text{Np}^{6+}$  into the studtite structure, based on the hexafluoride reference phases, is -0.10 eV (-9.65 kJ/mol; Table 4.3, Eq. 5), while the incorporation energy of  $\text{Np}^{6+}$  into the studtite structure based on the binary oxide reference phases is -0.07 eV (-6.75 kJ/mol; Table 4.3, Eq. 1). The more negative incorporation energy associated with the hexafluoride reference phases is in part due to the instability of  $\text{NpF}_6$  in comparison to  $\text{UF}_6$ . The standard enthalpy of formation for  $\text{NpF}_6$  (-1970 kJ/mol) is less negative than that of  $\text{UF}_6$  (-2317 kJ/mol), indicating that more energy is necessary for the formation of  $\text{NpF}_6$  (Lemire et al., 2001). The instability of  $\text{NpF}_6$  as compared to  $\text{UF}_6$  drives the incorporation equation, resulting in a more negative incorporation energy for Np in studtite using the hexafluoride reference phases; however, the presence of such hexafluoride reference phases in a geologic repository is unlikely.

Most of the incorporation energies for the binary oxide and hexafluoride reference phases are outside the range of the other common substitution processes where charge and ionic radius are comparable. For example, the exchange energetics for Cs/K exchange in muscovite ranges from -5.3 kJ/mol to 15.4 kJ/mol, depending on the mechanism for cation exchange (Rosso et al., 2001). However, the  $\text{NpO}_2/\text{UO}_3$  reference phase case results in a reasonably negative incorporation energy (-0.07 eV; -6.89 kJ/mol).

The same reference phases were used to determine the energy needed to incorporate  $\text{Np}^{5+}$  into studtite (Table 4.4). The charge-balancing mechanism was the coupled

Table 4.4. Incorporation equations and energies for  $\text{Np}^{5+}$  in studtite with various reference phases.

Reactants	$\rightleftharpoons$	Products	E (eV)
1 studtite + $\frac{1}{2}\text{Np}_2\text{O}_5 + \frac{1}{2}\text{H}_2\text{O}$	$\rightleftharpoons$	(studtite - $\text{U}^{6+} + \text{Np}^{5+} + \text{H}^+$ ) + $\text{UO}_3$	1.12
2 studtite + $\frac{1}{2}\text{Np}_2\text{O}_5 + \frac{1}{2}\text{H}_2\text{O}$	$\rightleftharpoons$	(studtite - $\text{U}^{6+} + \text{Np}^{5+} + \text{H}^+$ ) + $\text{UO}_2 + \frac{1}{2}\text{O}_2$	2.98
3 studtite + $\text{NpO}_2 + \frac{1}{4}\text{O}_2 + \frac{1}{2}\text{H}_2\text{O}$	$\rightleftharpoons$	(studtite - $\text{U}^{6+} + \text{Np}^{5+} + \text{H}^+$ ) + $\text{UO}_3$	0.63
4 studtite + $\text{NpO}_2 + \frac{1}{2}\text{H}_2\text{O}$	$\rightleftharpoons$	(studtite - $\text{U}^{6+} + \text{Np}^{5+} + \text{H}^+$ ) + $\text{UO}_2 + \frac{1}{4}\text{O}_2$	2.49
5 studtite + $\text{NpF}_6 + \frac{1}{2}\text{H}_2\text{O}$	$\rightleftharpoons$	(studtite - $\text{U}^{6+} + \text{Np}^{5+} + \text{H}^+$ ) + $\text{UF}_6 + \frac{1}{4}\text{O}_2$	0.60

substitution of  $\text{Np}^{5+}$  and  $\text{OH}^-$  for  $\text{U}^{6+}$  and  $\text{O}^{2-}$ . The substitution of  $\text{OH}^-$  for  $\text{O}^{2-}$  is achieved by adding an  $\text{H}^+$  atom bonded to an  $\text{O}^{2-}$  within the studtite structure. As previously detailed, the thermodynamically favorable position for the additional  $\text{H}^+$  atom is bonded to the axial  $\text{O}^{2-}$ . The same energy trends between the different reference phase cases are observed for  $\text{Np}^{5+}$  incorporation as for  $\text{Np}^{6+}$  incorporation. The incorporation energy of  $\text{Np}^{5+}$  into the studtite structure, based on the hexafluoride reference phases, is 0.60 eV (57.43 kJ/mol; Table 4.4, Eq. 5), and the incorporation energy of  $\text{Np}^{5+}$  into the studtite structure based on the binary oxide reference phases (*i.e.*,  $\text{NpO}_2$  and  $\text{UO}_3$ ) is 0.63 eV (60.79 kJ/mol; Table 4.4, Eq. 1). The difference between incorporation energy for the  $\text{Np}^{5+}$  and  $\text{Np}^{6+}$  cases is 0.70 eV (67.54 kJ/mol). Thus,  $\text{Np}^{6+}$  incorporation is favored over  $\text{Np}^{5+}$  in studtite.

### ***Thermodynamic properties of the (U,Np)-studtite solid solution***

Thermodynamic properties of the (U,Np)-studtite solid solution are calculated to estimate incorporation limits as a function of incorporation temperature. Enthalpies of mixing are based on the relative energy of different cation compositions and configurations with the U and Np-studtite phases as reference points. Different enthalpies of mixing for the same composition are due to different structural arrangements of the cations. For example, the relative enthalpies of mixing for 50:50 compositions range from -0.18 kJ/(mol exchangeable cation) to 0.68 kJ/(mol exchangeable cation), where the negative enthalpies of mixing correspond to configurations in which the exchanged cations are in the same actinyl chain along the [001] zone axis. The positive enthalpies of mixing correspond to configurations in which the cation exchange occurs along the [110]

and [111] zone axes. The interaction parameters and Margules parameters are fit to all configurations and compositions from the quantum-mechanical calculations. The Margules parameters for this system are  $W_1 = 2.75$  kJ/(mol exchangeable cation) and  $W_2 = -0.65$  kJ/(mol exchangeable cation). The interaction parameters are  $J_1 = 0.0486$  kJ/(mol U-Np interaction),  $J_2 = 0.0004$  kJ/(mol U-Np interaction), and  $J_3 = -0.0253$  kJ/(mol U-Np interaction), where  $J_1$  describes nearest neighbor interactions along the [001],  $J_2$  along the [110], and  $J_3$  along the [111]. Positive  $J$  values indicate that homocationic interactions are favored, while negative  $J$  values indicate that heterocationic interactions are favored. Thus, the  $(\text{Np}^{6+}, \text{U}^{6+})$ -studtite solid solution favors the same cations along the [001] and different cations along the [111]. The Margules and interaction parameters are on the same order of magnitude as the  $(\text{Hf}, \text{Zr})\text{SiO}_4$  series, which is a complete solid solution (Ferriss et al., 2009). The absolute value of the enthalpy of mixing for any composition or configuration of this solid solution is similar to the enthalpies of mixing for the complete  $(\text{Hf}, \text{Zr})\text{SiO}_4$  solid solution, but small relative to other incomplete solid solutions, such as  $(\text{U}, \text{Zr})\text{SiO}_4$  solid solution (Ferriss et al., 2009). The contribution of the excess enthalpy of mixing to the free energy of mixing is small as compared with the contribution of –temperature ( $-T$ ) times the configurational entropy for all temperatures calculated (333 K – 3000 K); thus, the free energy of mixing is negative for all compositions of the solid solution (Figure 4.9), indicating complete solid solution.

Although the incorporation energy of  $\text{Np}^{6+}$  into studtite is positive for the oxide reference phases, the thermodynamically stable limit of  $\text{Np}^{6+}$ -incorporation into studtite based on the full solid-solution analysis indicates that  $\text{Np}^{6+}$  is completely miscible in

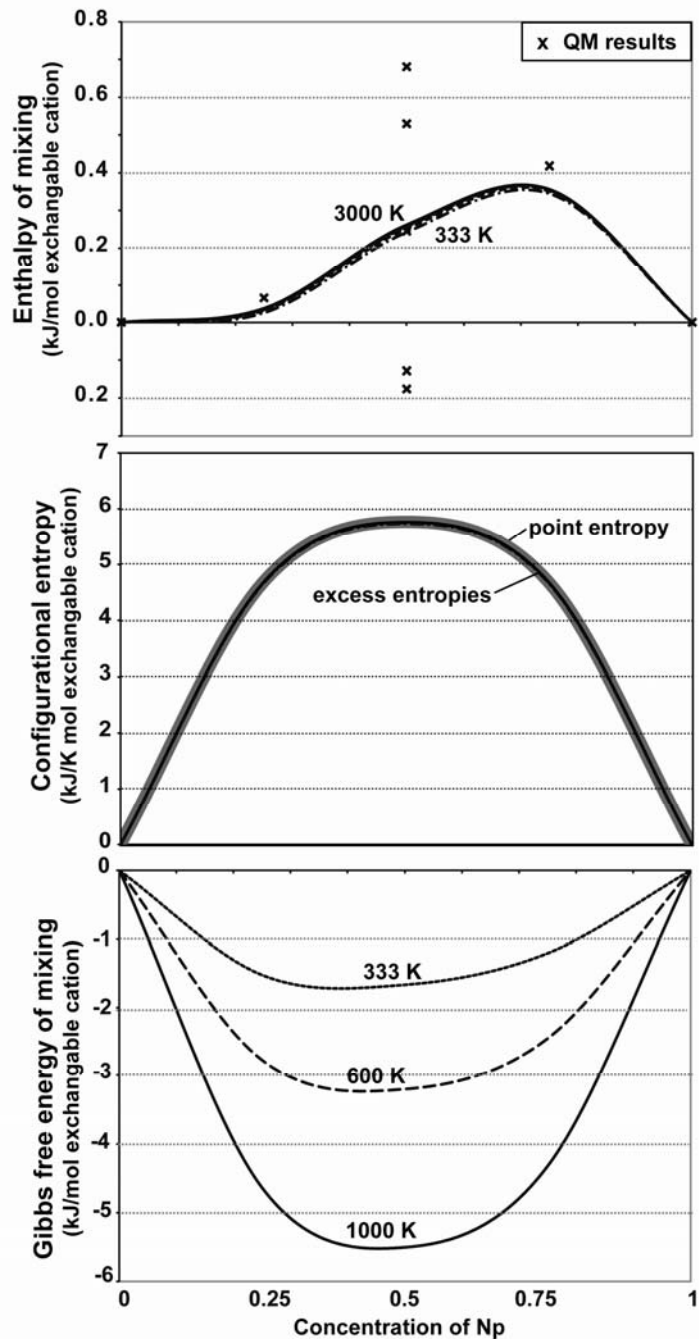


Figure 4.9. Enthalpy of mixing (kJ/mol exchangeable cation), configurational entropy of mixing (kJ/K mol exchangeable cation), and Gibbs free energy of mixing (kJ/mol exchangeable cation) vs. concentration of Np for  $(\text{Np}^{6+}_{0.25}\text{U}^{6+}_{0.75})$ -stutdtite solid solution. The quantum-mechanical and Monte-Carlo results are overlaid for the enthalpy of mixing. The configurational entropy of mixing is close to the point entropy, which indicates that the system does not order.

studtite, assuming that there is a fully-substituted studtite ( $\text{Np}^{6+}$ -studtite) that is isostructural with the  $\text{U}^{6+}$ -studtite. Both studtite and  $\text{Np}^{6+}$ -studtite are stable with respect to their oxide components (Table 4.5). The components used for this analysis include crystalline hydrogen peroxide (Abrahams et al., 1951), cubic ice,  $\text{O}_2$  molecule in a  $10 \times 10 \times 10 \text{ \AA}$  box,  $\text{UO}_3$  (Loopstra et al., 1977), and  $\text{Np}_2\text{O}_5$  (Forbes et al., 2007). The negative formation energy for  $\text{Np}^{6+}$ -studtite indicates the possibility for mineral formation; however, there are potential kinetic hindrances for the formation of  $\text{Np}^{6+}$ -studtite. The formation of  $\text{Np}^{6+}$ -studtite requires the oxidation of Np either in solution or in the solid-state. The oxidation of aqueous  $\text{Np}^{5+}$ , which is the dominate oxidation state in solution, to  $\text{Np}^{6+}$  requires highly oxidizing conditions (Silva and Nitsche, 1995; Kaszuba and Runde, 1999; Choppin 2007).

The formation energies of  $\text{Np}_2\text{O}_5$  and  $\text{NpO}_3$  were compared to understand possible kinetic hindrances in the solid state. While  $\text{Np}_2\text{O}_5$  is the oxide with the highest Np oxidation state (Forbes et al., 2007; Seibert et al., 2009), the formation energy of  $\text{NpO}_3$  with the  $\text{UO}_3$  (*Fddd*) structure was calculated for comparison. From the  $\text{Np}^{4+}$ -oxide ( $\text{NpO}_2$ ) and oxygen, the formation of  $\text{NpO}_3$  is energetically favored, while from the  $\text{Np}^{5+}$ -oxide ( $\text{Np}_2\text{O}_5$ ) and oxygen, the formation of  $\text{NpO}_3$  is not energetically favorable. The formation  $\text{Np}_2\text{O}_5$  from  $\text{NpO}_2$  and oxygen is more thermodynamically favorable than the formation of  $\text{NpO}_3$  from the same reactants (Table 4.5). Thus, an energy barrier exists to oxidizing  $\text{NpO}_2$  to  $\text{NpO}_3$  via  $\text{Np}_2\text{O}_5$ . This energy barrier may be the reason that  $\text{Np}^{6+}$ -studtite has not been synthesized. Thus, the complete miscibility of  $\text{Np}^{6+}$  in studtite is wholly based on the assumption of the formation of an  $\text{Np}^{6+}$ -studtite end-member, which is probably kinetically hindered.

Table 4.5. Enthalpy of formation from the oxide components for studtite,  $\text{Np}^{6+}$ -studtite,  $\text{UO}_3$ ,  $\text{NpO}_3$ , where the formation of  $\text{NpO}_3$  from  $\text{NpO}_2$  is compared with the formation from  $\text{Np}_2\text{O}_5$ .

Reactants	$\rightleftharpoons$	Products	$\Delta H_f(\text{eV})$
$\text{UO}_3 + \text{H}_2\text{O}_2 + 3\text{H}_2\text{O}$	$\rightleftharpoons$	studtite	-0.77
$\frac{1}{2}\text{Np}_2\text{O}_5 + \text{H}_2\text{O}_2 + 3\text{H}_2\text{O} + \frac{1}{4}\text{O}_2$	$\rightleftharpoons$	$\text{Np}^{6+}$ -studtite	-0.35
$\text{UO}_2 + \frac{1}{2}\text{O}_2$	$\rightleftharpoons$	$\text{UO}_3$	-1.86
$\text{NpO}_2 + \frac{1}{2}\text{O}_2$	$\rightleftharpoons$	$\text{NpO}_3$	-0.19
$\frac{1}{2}\text{Np}_2\text{O}_5 + \frac{1}{4}\text{O}_2$	$\rightleftharpoons$	$\text{NpO}_3$	0.30
$\text{NpO}_2 + \frac{1}{4}\text{O}_2$	$\rightleftharpoons$	$\frac{1}{2}\text{Np}_2\text{O}_5$	-0.49

Notes: The formation of  $\text{Np}_2\text{O}_5$  from  $\text{NpO}_2$  is also listed for comparison. Hydrogen peroxide and water were calculated in their solid crystalline state.  $\text{NpO}_3$  was constructed using the *Fddd*  $\text{UO}_3$  structure. Gaseous  $\text{O}_2$  is necessary to oxidize the  $\text{Np}^{5+}$  in the formation of  $\text{Np}^{6+}$ -studtite.

## Concluding Remarks

In summary, quantum-mechanical methods were used to refine the structure, determine the electronic structure, and calculate the incorporation energy of  $\text{Np}^{5+,6+}$  into studtite. The incorporation energy of  $\text{Np}^{6+}$  into studtite is lower than that of  $\text{Np}^{5+}$  in studtite for all reference phases considered; therefore,  $\text{Np}^{6+}$  is more likely, based purely on thermodynamics, to substitute for  $\text{U}^{6+}$  in the studtite structure. The solid-solution calculations indicate that  $\text{Np}^{6+}$  is completely miscible in studtite if a pure  $(\text{Np}^{6+})_{0.25}\text{U}^{6+}_{0.75}$ -studtite phase exists. However, the formation of  $(\text{Np}^{6+})_{0.25}\text{U}^{6+}_{0.75}$ -studtite is likely to be kinetically hindered. In addition, the electronic structure provides insight into possible incorporation mechanisms (*i.e.*, the involvement of peroxide in bonding). The band gap of the  $(\text{Np}^{6+}_{0.25}\text{U}^{6+}_{0.75})$ -studtite is less than the band gap of studtite by about 1.2 eV, due to the Np 5f and peroxide O 2p contribution at energy states within the studtite band gap. Specifically, the HOMO level of studtite and  $(\text{Np}^{6+}_{0.25}\text{U}^{6+}_{0.75})$ -studtite is populated by electron density associated with the peroxide O 2p orbitals, which are unique to the uranyl peroxide structure. Electrons in the valence band, especially the upper valence band, are often involved in incorporation and redox processes; thus, the peroxide within these structures probably plays a critical role in the Np incorporation.

## Appendix 1: $\text{Np}^{6+}$ -modified studtite

```
data_studNp6
_cell_length_a    13.9663
_cell_length_b    6.8828
_cell_length_c    8.5326
_cell_angle_alpha 90.0131
_cell_angle_beta  122.3995
_cell_angle_gamma 90.0439
```

```

loop_
_atom_site_label
_atom_site_fract_x
_atom_site_fract_y
_atom_site_fract_z
H    0.881071    0.352145    0.104309
H    0.898338    0.576446    0.076154
H    0.256283    0.004887    0.132327
H    0.253931    0.017868    0.319186
H    0.381096    0.852083    0.104490
H    0.398402    1.076556    0.076165
H    0.756237    0.504901    0.132328
H    0.753951    0.517782    0.319210
H    0.118926    0.352108    0.395647
H    0.101659    0.576427    0.423803
H    -0.256268   0.004915    0.367666
H    -0.253969   0.017876    0.180714
H    0.618893    0.852009    0.395893
H    0.601668    1.076550    0.423775
H    0.243964    0.505032    0.367600
H    0.246131    0.517714    0.180889
H    0.118929    0.647855    0.895692
H    0.101662    0.423554    0.923846
H    -0.256283   -0.004887   0.867673
H    -0.253931   -0.017868   0.680814
H    0.618904    0.147917    0.895510
H    0.601598    -0.076555   0.923835
H    0.243764    0.495099    0.867672
H    0.246049    0.482218    0.680789
H    0.881074    0.647892    0.604353
H    0.898341    0.423573    0.576197
H    0.256268   -0.004915   0.632334
H    0.253969   -0.017876   0.819286
H    0.381107    0.147991    0.604107
H    0.398332   -0.076550   0.576225
H    0.756036    0.494968    0.632400
H    0.753869    0.482286    0.819112
O    0.840696    0.477331    0.051744
O    0.205204    0.003984    0.181199
O    -0.003647   -0.246513   0.071543
O    0.061436    0.121325    0.305207
O    0.340717    0.977332    0.051547
O    0.705185    0.504049    0.181221
O    0.496326    0.253353    0.071547
O    0.560608    0.621504    0.305177
O    0.159336    0.477383    0.448697

```

O	-0.205246	0.003948	0.318717
O	0.003622	-0.246580	0.428418
O	-0.061437	0.121292	0.194873
O	0.659265	0.977365	0.448409
O	0.294860	0.504060	0.318659
O	0.503561	0.253586	0.428523
O	0.438583	0.622796	0.192977
O	0.159304	0.522669	0.948256
O	-0.205204	-0.003984	0.818801
O	0.003647	0.246513	0.928457
O	-0.061436	-0.121325	0.694793
O	0.659283	0.022668	0.948453
O	0.294815	0.495951	0.818779
O	0.503675	0.746647	0.928453
O	0.439392	0.378496	0.694823
O	0.840664	0.522617	0.551303
O	0.205246	-0.003948	0.681283
O	-0.003622	0.246580	0.571582
O	0.061437	-0.121292	0.805127
O	0.340735	0.022635	0.551591
O	0.705140	0.495940	0.681341
O	0.496439	0.746414	0.571477
O	0.561417	0.377204	0.807023
U	0.000000	0.000000	0.000000
U	0.500000	0.500000	0.000000
U	0.000000	0.000000	0.500000
Np	0.500000	0.500000	0.500000

## Appendix 2: Np<sup>5+</sup>-modified studtite

```

data_studNp5_new
_cell_length_a    13.9258
_cell_length_b    6.9812
_cell_length_c    8.4917
_cell_angle_alpha 90.0052
_cell_angle_beta  121.9168
_cell_angle_gamma 89.6499

loop_
_atom_site_label
_atom_site_fract_x
_atom_site_fract_y
_atom_site_fract_z
H      0.883578    0.353850    0.106699
H      0.900529    0.575787    0.078742

```

H	0.256564	0.004766	0.132866
H	0.254016	0.019387	0.320270
H	0.382983	0.853465	0.105147
H	0.396541	1.072639	0.065430
H	0.756897	0.506734	0.131870
H	0.753639	0.519837	0.318347
H	0.118299	0.356113	0.397803
H	0.100241	0.577306	0.426169
H	-0.255715	0.000878	0.372228
H	-0.254640	0.018963	0.183195
H	0.623271	0.838248	0.403807
H	0.608675	1.054734	0.452165
H	0.245219	0.507435	0.370212
H	0.246605	0.517676	0.182257
H	0.117371	0.646031	0.895873
H	0.100903	0.424251	0.925038
H	-0.254561	-0.002824	0.871996
H	-0.249058	-0.034312	0.688317
H	0.618137	0.148667	0.896143
H	0.600402	-0.073696	0.919479
H	0.244100	0.495249	0.870191
H	0.246869	0.482333	0.683076
H	0.882469	0.644779	0.604302
H	0.900202	0.423390	0.576294
H	0.256721	-0.005302	0.630497
H	0.252773	-0.020623	0.816723
H	0.381502	0.147221	0.604449
H	0.399670	-0.074161	0.572635
H	0.756308	0.499894	0.634585
H	0.754225	0.491825	0.821778
H	0.504190	0.244457	0.284677
O	0.843360	0.477956	0.054408
O	0.205676	0.003796	0.182490
O	-0.002340	-0.242669	0.074614
O	0.061458	0.123310	0.305606
O	0.340942	0.975679	0.048982
O	0.705072	0.508209	0.180287
O	0.496199	0.262937	0.082099
O	0.561578	0.624257	0.299904
O	0.158088	0.479088	0.450614
O	-0.205506	0.007789	0.321077
O	0.003966	-0.242396	0.428053
O	-0.061042	0.124045	0.196562
O	0.664838	0.958905	0.461803
O	0.295773	0.503055	0.319843
O	0.513597	0.237963	0.409747

O	0.438899	0.628947	0.192252
O	0.157919	0.522400	0.948978
O	-0.202647	-0.004161	0.824084
O	0.004581	0.243066	0.928734
O	-0.060458	-0.122387	0.696876
O	0.658179	0.024698	0.949412
O	0.295520	0.495256	0.821020
O	0.502509	0.746808	0.923609
O	0.440044	0.378353	0.699535
O	0.842489	0.521991	0.551471
O	0.204961	-0.006183	0.679053
O	-0.003503	0.243136	0.573540
O	0.062084	-0.123401	0.805300
O	0.341810	0.024525	0.551189
O	0.705780	0.510721	0.684585
O	0.492139	0.756568	0.574006
O	0.562570	0.377790	0.808251
U	0.000881	0.000174	0.001449
U	0.500089	0.505166	-0.001513
U	0.000061	0.000454	0.500474
Np	0.500336	0.509207	0.501120

## References

- Abrahams, S.C., Collin, R.L., and Lipscomb, W.N. (1951) The crystal structure of hydrogen peroxide. *Acta Crystallographia*, 4, 15-19.
- Abrefah, J., Marschmann, S., and Jenson, E.D. (1998) Examination of the surface coatings removed from K-East Basin fuel elements. Pacific Northwest National Laboratory Report. Pacific Northwest National Laboratory, Richland.
- Amme, M. (2002) Contrary effects of the water radiolysis product H<sub>2</sub>O<sub>2</sub> upon the dissolution of nuclear fuel in natural ground water and deionized water. *Radiochimica Acta*, 90(7), 399-406.
- Anisimov, V.I., Aryasetiawan, F., and Lichtenstein, A.I. (1997) First-principles calculations of the electronic structure and spectra of strongly correlated systems: The LDA+U method. *Journal of Physics-Condensed Matter*, 9(4), 767-808.
- Barner, J.O. (1985). Pacific Northwest National Laboratory Report. Pacific Northwest National Laboratory.

- Becker, U., Fernandez-Gonzalez, A., Prieto, M., Harrison, R., and Putnis, A. (2000) Direct calculation of thermodynamic properties of the barite/celestite solid solution from molecular principles. *Physical Chemical Mineralogy*, 27, 291-300.
- Becker, U. and Pollok, K. (2002) Molecular simulations of interfacial and thermodynamic mixing properties of grossular-andradite garnets. *Physics and Chemistry of Minerals*, 29, 52-64.
- Bosenick, A., Dove, M.T., Myers, E.R., Palin, E.J., Sainz-Diaz, C.I., Guiton, B.S., Warren, M.C., Craig, M.S., Redfern, S.A.T. (2001) Computational methods for the study of energies of cation distribution: applications to cation-ordering phase transitions and solid solutions. *Mineralogy Magazine*, 65, 193-219.
- Bruno, J. and Ewing, R.C. (2006) Spent nuclear fuel. *Elements*, 2(6), 343-349.
- Buck, E.C., Finch, R.J., Finn, P.A., and Bates, J.K. (1997) Retention of neptunium in uranyl alteration phases formed during spent fuel corrosion. In I.G. McKinley, and C. McCombie, Eds. 21st International Symposium on the Scientific Basis for Nuclear Waste Management, p. 87-94. Materials Research Society, Davos, Switzerland.
- Burns, P.C., Deely, K.M., and Skanthakumar, S. (2004) Neptunium incorporation into uranyl compounds that form as alteration products of spent nuclear fuel: Implications for geologic repository performance. *Radiochimica Acta*, 92(3), 151-159.
- Burns, P.C., Ewing, R.C., and Hawthorne, F.C. (1997) The crystal chemistry of hexavalent uranium: Polyhedron geometries, bond-valence parameters, and polymerization of polyhedra. *Canadian Mineralogist*, 35, 1551-1570.
- Burns, P.C. and Hughes, K.A. (2003) Studtite,  $[(\text{UO}_2)(\text{O}_2)(\text{H}_2\text{O})_2](\text{H}_2\text{O})_2$ : The first structure of a peroxide mineral. *American Mineralogist*, 88(7), 1165-1168.
- Burns, P.C., Kubatko, K.A., Sigmon, G., Fryer, B.J., Gagnon, J.E., Antonio, M.R., and Soderholm, L. (2005) Actinyl peroxide nanospheres. *Angewandte Chemie International Edition*, 44, 2135-2139.

- Cejka, J., Sejkora, J., and Deliens, M. (1996) New data on studtite,  $\text{UO}_4 \cdot 4\text{H}_2\text{O}$ , from Shinkolobwe, Shaba, Zaire. *Neues Jahrbuch Fur Mineralogie-Monatshefte*(3), 125-134.
- Choppin, G.R. (2007) Actinide speciation in the environment. *Journal of Radioanalytical and Nuclear Chemistry*, 273, 695-703.
- Debets, P.C. (1963) X-ray diffraction data on hydrated uranium peroxide. *Journal of Inorganic & Nuclear Chemistry*, 25(6), 727-730.
- Douglas, M., Clark, S.B., Friese, J.I., Arey, B.W., Buck, E.C., and Hanson, B.D. (2005a) Neptunium(V) partitioning to uranium(VI) oxide and peroxide solids. *Environmental Science & Technology*, 39(11), 4117-4124.
- Douglas, M., Clark, S.B., Friese, J.I., Arey, B.W., Buck, E.C., Hanson, B.D., Utsunomiya, S., and Ewing, R.C. (2005b) Microscale characterization of uranium(VI) silicate solids and associated neptunium(V). *Radiochimica Acta*, 93(5), 265-272.
- Ferriss, E.D.A., Essene, E.J., and Becker, U. (2008) Computational study of the effect of pressure on the Ti-in-zircon geothermometer. *European Journal of Mineralogy*, 20(5), 745-755.
- Ferriss, E.D.A., Ewing, R.C., and Becker, U. (2009) Simulation of thermodynamic mixing properties of actinide-containing zircon solid solutions. *American Mineralogist*, in press.
- Finch, R.J. and Ewing, R.C. (1992) The corrosion of uraninite under oxidizing conditions. *Journal of Nuclear Materials*, 190, 133-156.
- Forbes, T.Z., Burns, P.C., Skanthakumar, S., and Soderholm, L. (2007) Synthesis, structure, and magnetism of  $\text{Np}_2\text{O}_5$ . *Journal of the American Chemical Society*, 129(10), 2760-2761.
- Fortner, J.A., Finch, R.J., Kropf, A.J., and Cunnane, J.C. (2004) Re-evaluating neptunium in uranyl phases derived from corroded spent fuel. *Nuclear Technology*, 148(2), 174-180.

- Guillaumont, R., Fanghanel, T., Fuger, J., Grenthe, I., Neck, V., Palmer, D.A., and Rand, M.H. (2003) Update on Chemical Thermodynamics of Uranium, Neptunium, Plutonium, Americium, and Technetium, Elsevier, Amsterdam.
- Gupta, F., Brillant, G., and Pasturel, A. (2007) Correlation effects and energetics of point defects in uranium dioxide: a first principle investigation. *Philosophical Magazine*, 87, 2561-2569.
- Hanson, B., McNamara, B., Buck, E., Friese, J., Jenson, E., Krupka, K., and Arey, B. (2005) Corrosion of commercial spent nuclear fuel. 1. Formation of studtite and metastudtite. *Radiochimica Acta*, 93(3), 159-168.
- Kaszuba, J.P. and Runde, W.H. (1999) The aqueous geochemistry of neptunium: Dynamic control of soluble concentrations with applications to nuclear waste disposal. *Environmental Science & Technology*, 33(24), 4427-4433.
- Klingensmith, A.L., Deely, K.M., Kinman, W.S., Kelly, V., and Burns, P.C. (2007) Neptunium incorporation in sodium-substituted metaschoepite. *American Mineralogist*, 92(4), 662-669.
- Kubatko, K.A. and Burns, P.C. (2006) Expanding the crystal chemistry of actinyl peroxides: Open sheets of uranyl polyhedra in  $\text{Na}_5[(\text{UO}_2)_3(\text{O}_2)_4(\text{OH})_3](\text{H}_2\text{O})_{13}$ . *Inorganic Chemistry*, 45(16), 6096-6098.
- Kubatko, K.A., Forbes, T.Z., Klingensmith, A.L., and Burns, P.C. (2007) Expanding the crystal chemistry of uranyl peroxides: Synthesis and structures of Di- and triperoxodioxouranium(VI) complexes. *Inorganic Chemistry*, 46(9), 3657-3662.
- Kubatko, K.A.H., Helean, K.B., Navrotsky, A., and Burns, P.C. (2003) Stability of peroxide-containing uranyl minerals. *Science*, 302(5648), 1191-1193.
- Lemire, R.J., Fuger, J., Nitsche, H., Potter, P.E., Rand, M.H., Rydberg, J., Spahiu, K., Sullivan, J.C., Ullman, W.J., Vitorge, P., and Wanner, H. (2001) Chemical thermodynamics of neptunium and plutonium, vol. 4, Elsevier, Amsterdam.
- Loopstra, B.O., Taylor, J.C., and Waugh, A.B. (1977) Neutron powder profile studies of the gamma uranium trioxide phases. *Journal of Solid State Chemistry*, 20, 9-19.

- Malkova, N.N. Matyukha, V.A., Afanaseva, T.V., and Krot, N.N. (1986) Reduction of Np(V) by hydrogen-peroxide in the presence of oxalic-acid. Soviet Radiochemistry, 28, 294-300.
- McNamara, B., Hanson, B., Buck, E., and Soderquist, C. (2005) Corrosion of commercial spent nuclear fuel. 2. Radiochemical analyses of metastudtite and leachates. Radiochimica Acta, 93(3), 169-175.
- Ostanin, S. and Zeller, P. (2007) Ab initio study of uranyl peroxides: Electronic factors behind the phase stability. Physical Review B, 75(7), 073101.
- Payne, M.C., Teter, M.P., Allan, D.C., Arias, T.A., and Joannopoulos, J.D. (1992) Iterative minimization techniques for abinitio total-energy calculations - Molecular-dynamics and conjugate gradients. Reviews of Modern Physics, 64(4), 1045-1097.
- Perdew, J.P., Burke, K., and Ernzerhof, M. (1996) Generalized gradient approximation made simple. Physical Review Letters, 77(18), 3865-3868.
- Reich, M. and Becker, U. (2006) First-principles claculations of the thermodynamic mixing properties of arsenic incorporation into pyrite and marcasite. Chemical Geology, 225, 278-290.
- Robie and Hemingway (1995) Thermodynamic properties of minerals and related substances at 298.15 K and 1 Bar (105 Pascals) pressure and at higher temperatures. U.S. Geological Survey Bulletin No. 2131, Washington, D.C.
- Rosso, K.M., Rustad, J.R., and Bylaska, E.J. (2001) The Cs/K exchange in muscovite interlayers: An ab initio treatment. Clays and Clay Minerals, 49(6), 500-513.
- Segall, M.D., Lindan, P.J.D., Probert, M.J., Pickard, C.J., Hasnip, P.J., Clark, S.J., and Payne, M.C. (2002) First-principles simulation: ideas, illustrations and the CASTEP code. Journal of Physics-Condensed Matter, 14(11), 2717-2744.
- Seibert, A., Gouder, T., and Huber, F. (2009) Reaction of neptunium with molecular and atomic oxygen: Formation and stability of surface oxides. Journal of Nuclear Materials, 389, 470-478.

- Shilov, V.P., Gogolev, A.V., and Pikaev, A.E. (1998) The formation of neptunium peroxy complexes upon reduction of neptunium(VI) by hydrogen peroxide in concentrated solutions of alkalis. Mendeleev Communications, 6, 220-222.
- Silva, R.J. and Nitsche, H. (1995) Actinide environmental chemistry. Radiochimica Acta, 70-71, 377-396.
- Skomurski, F.N., Ewing, R.C., Rohl, A.L., Gale, J.D., and Becker, U. (2006) Quantum mechanical *vs.* empirical potential modeling of uranium dioxide ( $\text{UO}_2$ ) surfaces: (111), (110), and (100). American Mineralogist, 91(11-12), 1761-1772.
- Walenta, K. (1973) Studtite and its composition. American Mineralogist, 59(1-2), 166-171.
- Wronkiewicz, D.J., Bates, J.K., Gerding, T.J., Veleckis, E., and Tani, B.S. (1992) Uranium release and secondary phase formation during unsaturated testing of  $\text{UO}_2$  at 90-degrees-C. Journal of Nuclear Materials, 190, 107-127.
- Wronkiewicz, D.J., Bates, J.K., Wolf, S.F., and Buck, E.C. (1995) Ten-year results from unsaturated drip tests with  $\text{UO}_2$  at 90 degrees C: Implications for the corrosion of spent nuclear fuel. Proceedings of the Spent Fuel Workshop, p. 78-95. Elsevier Science Bv, Überlingen, Germany.
- Yeomans, J.M. (1992) Statistical mechanics of phase transitions, Oxford Science Publications, Clarendon Press, Oxford, 164 p.

## **Chapter 5**

# **Np-incorporation into uranyl phases: A quantum-mechanical evaluation**

### **Abstract**

The release and mobility of key radionuclides, such as long-lived minor actinides (*e.g.*,  $^{237}\text{Np}$ ;  $\tau_{1/2} = 2.1$  my), may be controlled by incorporation into the alteration phases of corroded  $\text{UO}_2$  in used nuclear fuel. Experimental results suggest that uranyl structures with charged interlayer cations have a greater ability to incorporate  $\text{Np}^{5+}$  than uranyl structures that do not contain interlayer cations; however, the mechanism of incorporation has not yet been determined. Density functional theory calculations are used to compare mechanisms of charge-balanced  $\text{Np}^{5+}$ -incorporation into boltwoodite [ $\text{K}(\text{UO}_2)(\text{SiO}_3\text{OH})(\text{H}_2\text{O})_{1.5}$ ]. The charge-balancing mechanisms considered include: *i*)  $\text{H}^+$  addition ( $\text{Np}^{5+} + \text{H}^+ \leftrightarrow \text{U}^{6+}$ ), *ii*) interlayer substitution ( $\text{Np}^{5+} + \text{Ca}^{2+}/\text{Mg}^{2+} \leftrightarrow \text{U}^{6+} + \text{K}^+$ ), and *iii*) intra-layer substitution ( $\text{Np}^{5+} + \text{P}^{5+} \leftrightarrow \text{U}^{6+} + \text{Si}^{4+}$ ). The choice of the source and sink phases, the reference phases, for the cations involved in the incorporation reaction greatly affects the final calculated incorporation energy. The incorporation energies using oxide ( $\Delta E_{oxide} = 2.4$  eV) and silicate ( $\Delta E_{silicate} = 1.2$  eV) reference phases

are compared for the interlayer substitution mechanism. Since both the source of Np in environmental systems and the cations released are typically aqueous complexes, combinations of cluster and periodic simulations were employed to model exchange with aqueous complexes. For the H<sup>+</sup> addition mechanism, incorporation from oxides reference phases ( $\Delta E_{incorporation} = 0.79$  eV) is less favorable than from aqueous ( $\Delta E_{incorporation} = 0.66$  eV) reference species. Estimates of the solid-solution behavior of Np<sup>5+</sup>/P<sup>5+</sup>- and U<sup>6+</sup>/Si<sup>4+</sup>-boltwoodite solid solutions are used to predict the limit of Np-incorporation into boltwoodite, where the incorporation energy of 0.86 eV results in a maximum amount of incorporation of 585 ppm at 300 °C.

## **Introduction**

The behavior of actinide contaminants in the near-surface geosphere and biosphere is a serious environmental and human health issue. Actinides may be released into the environment by the breach of a nuclear waste package in a geologic repository, by the contact of groundwater with uranium deposits, or during a nuclear reactor accident. The mobility of released actinides in the environment depends on many factors, but one important process is the incorporation of the actinide into newly formed phases, such as the corrosion products on used nuclear fuel. For example, actinide incorporation into mineral structures could significantly limit the mobility of actinides in geologic settings. Under oxidizing conditions, uranium dioxide (UO<sub>2+x</sub>), the primary uranium mineral in ore deposits, as well as the most commonly used nuclear fuel matrix, oxidizes to a sequence of uranium(VI) phases, depending on the composition of the groundwater that is in contact with the UO<sub>2</sub>. The general paragenesis of uranyl alteration is from uranyl

oxyhydroxides to silicates/phosphates to more soluble phases such as carbonates, depending on the solution chemistry (Finch and Ewing, 1992; Finch and Murakami, 1999). Burns et al. (1997) first suggested Np(V)-incorporation into uranium alteration phases based on similarities in the Np(V) and U(VI) chemistries, most notably the because of the similarities in neptunyl and uranyl molecules.

Several experimental studies have been conducted over the past couple of decades to quantify the amount of Np that can be incorporated in different uranyl phases (Buck et al., 1998; Fortner et al., 2004; Buck et al., 2004; Burns et al., 2004; Friese et al., 2004; Douglas et al., 2005; Burns and Klingensmith, 2006; Klingensmith and Burns, 2007; Klingensmith et al., 2007). The analytical methods used to examine the Np-doped crystals have evolved over the years. Initially, standard transmission electron microscopy and synchrotron techniques such as electron energy loss spectroscopy (EELS) and X-ray adsorption spectroscopy (XAS) were used (Buck et al., 1998; Fortner et al., 2004) to quantify the amount of Np incorporated into uranyl oxyhydroxides, specifically dehydrated schoepite [ $\text{UO}_3 \cdot 0.8\text{H}_2\text{O}$ ]. EELS data indicated that 550 ppm Np were incorporated into dehydrated schoepite during the corrosion of spent nuclear fuel (SNF) exposed to water vapor and held at 90 °C for up to 4.1 years. Later, synchrotron XAS data indicated little to no Np incorporation in the dehydrated schoepite, which formed during similar hydration-corroded SNF experiments. These contradicting results led to the explanation that a superfluous peak in EELS measurements due to a plural-scattering event may have contributed to the enhanced appearance of the Np M<sub>5</sub> energy peak (Fortner et al., 2004). The weaker Np M<sub>4</sub> energy peak is not subject to such interference from the plural scattering event of the U M<sub>4</sub> edge; therefore, later studies, continue the

use of EELS measurements to quantify Np-incorporation into uranyl phases (Buck et al., 2004).

A series of systematic crystal-chemistry experiments on  $\text{Np}^{5+}$ -incorporation into uranyl phases continued in order to develop an understanding about the charge-balancing mechanism of Np-incorporation into uranyl phases (Burns et al., 2004; Burns and Klingensmith, 2006; Klingensmith and Burns, 2007; Klingensmith et al., 2007). Initially, inductively coupled plasma-mass spectroscopy (ICP-MS) was used to quantify the amount of Np incorporated into synthetic uranyl phases, indicating that Np was incorporated into phases with charged sheet structures and interlayer cations (*i.e.*, uranophane and Na-compreignacite) in the hundreds of ppm range. In contrast, much lower amounts of Np (5-36 ppm) were incorporated into uranyl phases that contain only water in their interlayer (meta-schoepite and  $\beta$ -( $\text{UO}_2$ )(OH)<sub>2</sub>) (Burns et al., 2004). The results for meta-schoepite are in agreement with those measured by Friese et al. (2004) for incorporation of Np at below-neutral pH. Douglas et al. (2005) characterized uranyl silicate phases precipitated in the presence of aqueous  $\text{NpO}_2^+$  using added  $\text{Na}^+$  in solution as a possible charge-balancing cation, where the coupled-substitution mechanism involves the substitution of  $\text{NpO}_2^+$  and  $\text{Na}^+$  for  $\text{UO}_2^{2+}$  and  $\text{H}_2\text{O}$ . Gamma spectroscopy was used to measure the significant concentration of Np (780-15,800  $\mu\text{g/g}$ ) in the solid phase, and TEM/EELS indicated that the Np was associated with the uranyl crystals. While previous studies using traditional ICP-MS indicated an association between Np and specific uranyl phases, incorporation into the phases could not be confirmed. Laser-ablation (LA)-ICP-MS was used most recently to verify that  $\text{Np}^{5+}$  had been incorporated into the solid Na-substituted metaschoepite (Klingensmith et al., 2007).

All of these experimental results are interpreted as being due to a charge-balancing, coupled substitution mechanism; however, the resolution of the analytical techniques used in previous studies does not provide information on the atomic-scale substitution mechanism. Observations or simulations at the atomic and electronic scale are required in order to understand changes in the Np-bonding environment and provide insight into possible charge-balancing, coupled substitution mechanisms. In this study, quantum-mechanical calculations are used in order to compare the ground state incorporation energy of a variety of mechanisms for  $\text{Np}^{5+}$ -incorporation into boltwoodite.

### Boltwoodite: Occurrence and structure

Boltwoodite is a naturally occurring uranium(VI) silicate that occurs as an alteration product of uraninite,  $\text{UO}_{2+x}$ , at uranium deposits: Pick's Delta mine, Emery County, Utah (Frondel and Ito, 1956), Pena Blanca, Chihuahua, Mexico (Wong et al., 1999), and Upper Jurassic Morrison Formation in the Grants uranium region, New Mexico (Deditius et al., 2008). In addition, boltwoodite is observed as an alteration product in laboratory corrosion studies of  $\text{UO}_2$  and SNF (Finn et al., 1996; Wronkiewicz et al., 1996). The pale yellow to amber mineral forms aggregates of needle-like crystals (Figure 5.1).

Boltwoodite is a uranyl silicate ( $P2_1/m$ ) composed of sheets of edge- and corner-sharing uranyl pentagonal bipyramids and silicon tetrahedra (Burns, 1998; Stohl and Smith, 1981), which follow the  $\alpha$ -uranophane anion topology (Burns, 2005; Burns et al., 1997). The polyhedron geometries in the uranyl sheets are typical of uranyl structures, where the U(VI) is strongly bonded to two oxygen forming the linear uranyl molecule ( $\text{UO}_2^{2+}$ ). The uranyl is equatorially coordinated by five oxygen atoms forming a



Figure 5.1. This pale yellow to amber specimen from Rossing Mine, Arandis, Swakopmund District, Erongo Region, Namibia shows the needle-like habit and aggregation is common for boltwoodite (Photo by: Rob Lavinsky, rob@irocks.com).

pentagonal bipyramid. The Si cations are tetrahedrally coordinated by oxygen and an OH<sup>-</sup>, forming an SiO<sub>3</sub>OH group (Vochten et al., 1997). The sheets have a net negative charge and stack with cations in the interlayer for charge compensation. The interlayer is composed of water and either K<sup>+</sup> or a combination of K<sup>+</sup> and Na<sup>+</sup>, forming the K/Na-boltwoodite solid-solution (Burns, 1998). For computational simplicity, the boltwoodite interlayer in this study is composed of water and K<sup>+</sup> (Figure 5.2).

### Computational Methodology

Periodic density functional theory calculations as implemented in the program CASTEP (CAmbridge Serial Total Energy Package, (Segall et al., 2002)) were used to optimize the geometry and calculate the ground state total energy of the structures involved in the incorporation reactions. A planewave basis set within the periodic boundary conditions is used to take advantage of Bloch's theorem, which enables implementation of a simplified version of the Kohn-Sham equation. Ultra-soft pseudopotentials are used to describe the behavior of the core electrons and their interactions with the valence electrons (Vanderbilt, 1990). The remaining valence electrons (*e.g.*, U valence configuration = [Xe]6s<sup>2</sup>6p<sup>6</sup>6d<sup>1</sup>5f<sup>3</sup>7s<sup>2</sup>) are treated explicitly. The generalized gradient approximation (GGA) with the Perdew-Burke-Ernzerhof (PBE) functional is used to approximate electron exchange and correlation (Perdew et al., 1996). In addition, a spin-polarized approach was taken to account for the two unpaired 5f electrons of Np<sup>5+</sup>. The kinetic energy cut-off for the planewaves was chosen to be 800 eV, and the k-point spacing was 0.07 Å<sup>-1</sup>. The total energy convergence tolerance was 1·10<sup>-5</sup> eV/atom, and the geometry convergence tolerance was 2·10<sup>-5</sup> eV/atom.

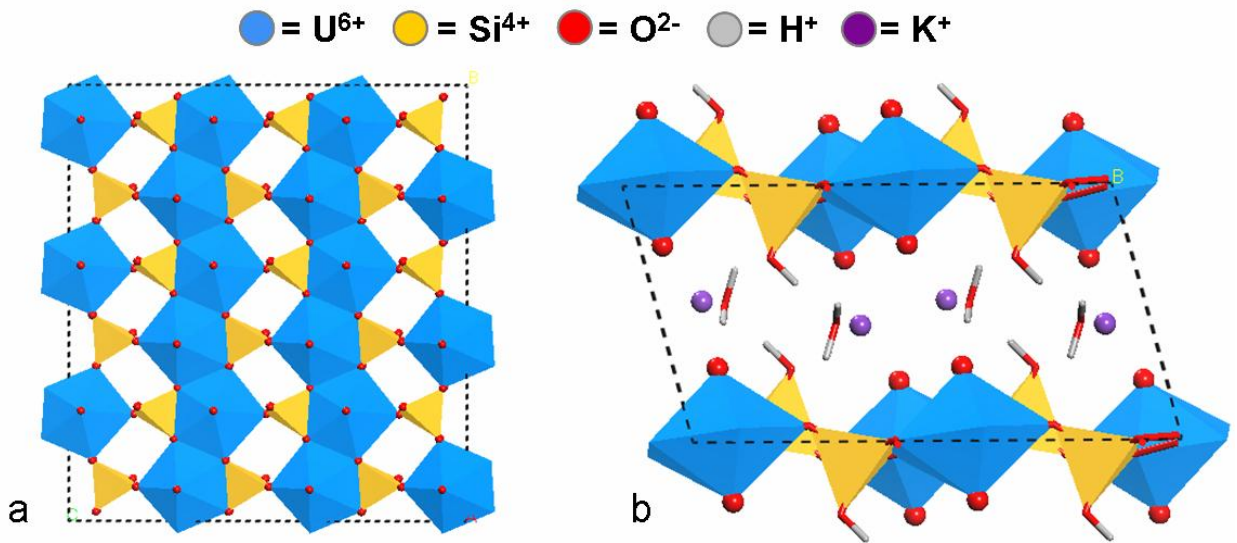


Figure 5.2. Boltwoodite sheet structure shown from two directions: (a) uranyl sheet in which chains of edge-sharing uranyl polyhedra are connected by edge- and corner-sharing silica tetrahedral and (b) interlayer between the uranyl sheets, which contains K<sup>+</sup> and H<sub>2</sub>O.

### ***What is the meaning of the CASTEP energy?***

Atomic-level calculations provide insight into processes not observed through analytical or experimental means; however, quantitative results (*e.g.*, final enthalpies, incorporation energies) must be compared with analytical and/or experimental results to verify the accuracy of the calculations. Experimentally, the enthalpy or energy of formation is measured for many solid phases; however, the quantum-mechanically determined energy of the same phase is not the energy of formation. Depending on the computational method, the calculated energy for a solid phase is the lattice energy (*e.g.*, GULP calculations using empirical force fields) or the reaction energy of zero-valent gas-phase elements (*e.g.*, CASTEP calculations). The flowchart in Figure 5.3 shows three chemical reactions describing the formation of UO<sub>2</sub> from (a) natural zero-valent phases, (b) gaseous zero-valent elements, and (c) ions, where the energies of the resulting UO<sub>2</sub> are the (a) formation energy, (b) CASTEP energy, and (c) lattice energy, respectively.

The formation energy can be calculated in CASTEP by taking the energy difference between UO<sub>2</sub> and the reactants (U<sub>metal</sub> and gaseous O<sub>2</sub>), where gaseous O<sub>2</sub> is calculated as an O<sub>2</sub> molecule in a 10×10×10 Å box. The lattice energy for UO<sub>2</sub> can also be calculated, primarily in CASTEP, by adding the ionization energy (U<sup>0</sup> → U<sup>4+</sup>) and the electron affinity (O<sup>0</sup> → O<sup>2-</sup>) to the energy for the zero-valent elements. The values for the ionization energy and electron affinity can be calculated using a quantum-mechanical cluster approach in a program such as Gaussian or taken from experimental measurements. For example, the lattice energy for UO<sub>2</sub> as calculated in GULP is -103.7 eV using the empirical potential set described in Catlow et al. (1987), while the lattice

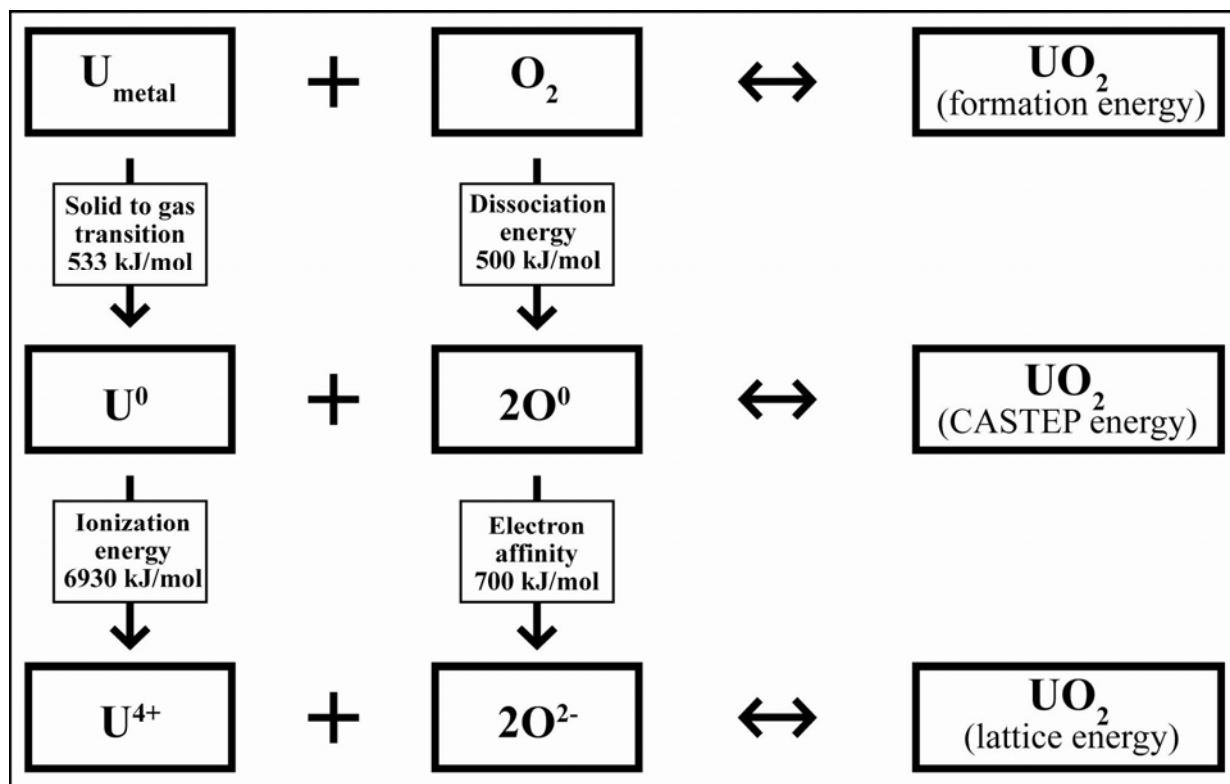


Figure 5.3. Flowchart describing the relationship between formation energy, CASTEP energy, and lattice energy for  $\text{UO}_2$ .

energy for  $\text{UO}_2$  as calculated in CASTEP with (a) computationally determined ionization energy and electron affinity added is -104.2 eV and (b) experimentally determined ionization energy and electron affinity added is -98.1 eV. Here, the zero-valent oxygen was calculated with a spin multiplicity of 3 (equivalent to two unpaired spins). The lattice energy for  $\text{UO}_2$  as calculated in CASTEP with (a) computationally determined IE and EA and (b) experimentally determined IE and EA, where the zero-valent oxygen has a spin multiplicity of 1, equals -100.3 eV and -99.7 eV, respectively. Table 5.1 lists the lattice energies determined using GULP and CASTEP. The CASTEP lattice energies are calculated based on Equation 1, where IE and EA are either experimentally or computationally (Gaussian) determined.

$$E_{lattice} = E^{CASTEP}(\text{UO}_2) - [(E^{CASTEP}(\text{U}^0) + \text{IE}) + 2 * (E^{CASTEP}(\text{O}^0) + \text{EA})] \quad (1)$$

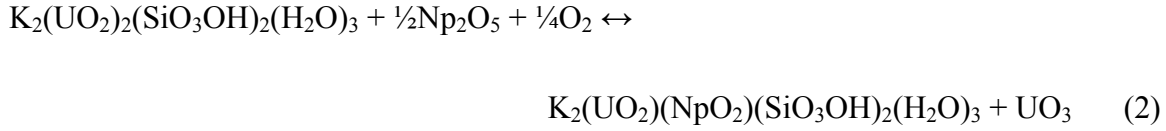
### ***Calculating incorporation energies***

To understand the energy associated with the substitution of neptunium for uranium in boltwoodite, the incorporation energy is calculated. The incorporation energy is the change in energy of a stoichiometric reaction describing the incorporation. For example, Reaction 2 describes the incorporation of  $\text{Np}^{6+}$  for  $\text{U}^{6+}$  in boltwoodite, where the source for Np is  $\text{Np}_2\text{O}_5$ , the sink for U is  $\text{UO}_3$ , and  $\frac{1}{4}\text{O}_2$  accounts for the oxidation of  $\text{Np}^{5+}$  in  $\text{Np}_2\text{O}_5$  to  $\text{Np}^{6+}$  that is substituted for  $\text{U}^{6+}$ . The incorporation energy is the difference between the energy of the products (modified-boltwoodite and  $\text{UO}_3$ ) and reactants (boltwoodite,  $\frac{1}{2}\text{Np}_2\text{O}_5$ , and  $\frac{1}{4}\text{O}_2$ ). The energies used in the calculation of incorporation energy can come from CASTEP energies, energies of formation, or lattice energies, as long as the same type of energy is used for each compound in the reaction. Using either

Table 5.1. Lattice energy (eV) for  $\text{UO}_2$  as calculated from various combinations of methods.

<b>Method</b>	<b><math>E_{\text{lattice}}</math> (eV)</b>
CASTEP + Gaussian ( $\text{O}^0_{\text{singlet}}$ )	-104.21
CASTEP + Gaussian ( $\text{O}^0_{\text{triplet}}$ )	-100.27
CASTEP + Experimental ( $\text{O}^0_{\text{singlet}}$ )	-98.12
CASTEP + Experimental ( $\text{O}^0_{\text{triplet}}$ )	-99.69
GULP	-103.65

energies of formation or lattice energies for calculating the incorporation energy also provides information with respect to the source/sink phases. However, unless the modified structure is well characterized, including the atomic positions of the H<sup>+</sup> atoms, *e.g.*, using neutron diffraction data, CASTEP calculations are necessary in order to gain insight into the incorporation mechanism and corresponding energy as a function of the location of the substituted cations in the modified structure. Even if all atomic positions were available from experiments, a quantum-mechanical approach is still necessary to account for energy contributions from electronic relaxations and spin-spin interactions. Thus, all incorporation energies are calculated from the CASTEP energies of the reactants and products. One possible incorporation reaction (here, with the incorporation of Np as Np<sup>6+</sup>) can be written as in Reaction 2:



Neptunium(V) is the most common aqueous neptunium oxidation state for a wide range of geochemistries (Kaszuba and Runde, 1999); therefore, incorporation energies are better calculated for the substitution of Np<sup>5+</sup> for U<sup>6+</sup> in boltwoodite, in contrast to Reaction 2. The substitution of a hexavalent cation for a pentavalent cation results in an overall negative charge; therefore, a charge-balancing coupled-substitution mechanism is necessary in order to maintain charge neutrality. Three such charge-balancing coupled-substitution mechanisms are considered here: *i*) addition of an H<sup>+</sup> atom, *ii*) interlayer substitution, and *iii*) intra-layer substitution. For the coupled substitution of Np<sup>5+</sup> and H<sup>+</sup> for U<sup>6+</sup>, several locations for the H<sup>+</sup> atom are compared. Similarly, for the coupled-

substitution of  $\text{Np}^{5+}$  and a divalent interlayer cation ( $\text{Ca}^{2+}$  or  $\text{Mg}^{2+}$ ) for  $\text{U}^{6+}$  and  $\text{K}^+$ , respectively, both interlayer  $\text{K}^+$  sites in the unit cell are compared. The intra-layer coupled-substitution mechanism involves the substitution of  $\text{P}^{5+}$  for  $\text{Si}^{4+}$  in the tetrahedral site.

The incorporation energy depends on the mechanism of incorporation (*e.g.*,  $\text{H}^+$  addition *vs.* interlayer substitution), placement of substituted ions (*e.g.*, the location of additional  $\text{H}^+$ ), and the reference phases (sources and sinks) for the ions involved in the substitution reaction. The mechanism of incorporation and placement of substituted ions are addressed by the comparison of different charge-balancing mechanisms. The impact of reference phases is considered in detail. Oxide reference phases and aqueous ion reference species are compared for the  $\text{H}^+$  incorporation mechanisms, while oxide and silicate reference phases are compared for the different interlayer substitution mechanism.

### ***Estimating the limit of Np-incorporation***

Validating computational results with experimental measurements is essential; however, experiments do not measure the energy required to incorporate Np into uranyl phases as described in the previous section. Instead, the limit of Np incorporation is measured; therefore, a computationally-determined limit of Np-incorporation is useful for the comparison of the calculated results with actual measurements.

The limit of incorporation can be determined based on the Gibbs free energy of mixing for a complete solid solution, where a tangent connecting the minima of the Gibbs free energy curve indicates the limit,  $x$ , of incorporation. However, for some solid

solutions, like the Np-U-boltwoodite discussed below, the minima of the Gibbs free energy of mixing cannot be resolved graphically due to the small limit of the concentrations calculated. Ferriss et al. (2008, 2010) approximated the limit of substitution for a variety of elements in zircon based on the assumption that the free energy of mixing is essentially linear at concentrations near the *minima* (Equation 3).

$$x_{inc} = \frac{e^{\left(\frac{-\Delta H_1}{X_1}\right)\left(\frac{1}{RT}\right)}}{1 + e^{\left(\frac{-\Delta H_1}{X_1}\right)\left(\frac{1}{RT}\right)}} \quad (3)$$

The smallest concentration for which the enthalpy of mixing was calculated and that was used to establish the linear dependence of  $\Delta H_{mix}$  was  $x = 0.03$  in the zircon study. However, due to the complexity of the boltwoodite structure, the smallest intermediate composition for Np-incorporation used here is  $x = 0.5$ . Thus, the free energy of mixing is *not* linear between the minimum concentration tested ( $x = 0.5$ ) and the *minima* of the Gibbs free energy.

More rigorously, the Gibbs free energy of mixing [ $\Delta G_{mix}$ , where  $\Delta G_{mix}(x) = \Delta H_{mix}(x) - T\Delta S_{mix}(x)$ ] is determined from the enthalpy of mixing ( $\Delta H_{mix}$ ) and the configurational entropy without ordering,  $\Delta S_{mix}(x) = -R[x \ln x + (1-x) \ln(1-x)]$ . The  $\Delta H_{mix}$  is then fit to a symmetric one-parameter Margules function,  $\Delta H_{mix}(x) = A x (1-x)$ , where  $A$  is calculated using the enthalpy of mixing at 50% incorporation. The minimum of the  $\Delta G_{mix}$  occurs when the first derivative of  $\Delta G_{mix}$  with respect to  $x$  equals zero (Equation 4), which has to be resolved numerically (Equation 5). Equation 5 is solved numerically using the Banach fixed point theorem.

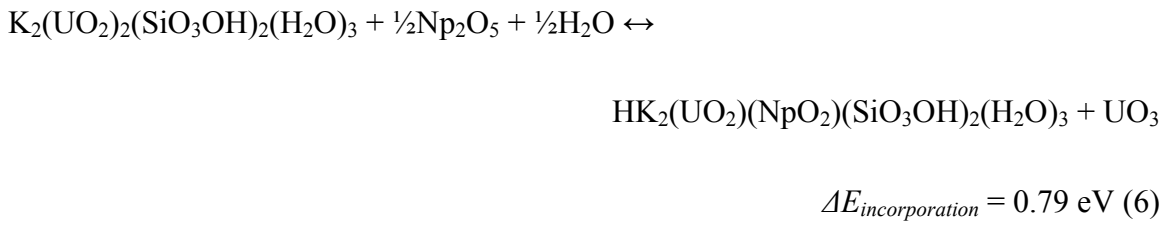
$$\frac{\partial}{\partial x} [Ax(1-x) + RT(x \ln x + (1-x) \ln(1-x))] = 0 \quad (4)$$

$$(1-x) \exp\left(\frac{-A[1-2x]}{RT}\right) = x \quad (5)$$

## Results

### **Substitution mechanism I: $\text{Np}^{5+} + \text{H}^+ \leftrightarrow \text{U}^{6+}$**

In the coupled substitution of  $\text{Np}^{5+}$  and  $\text{H}^+$  for  $\text{U}^{6+}$ , the energetically-favored position of the  $\text{H}^+$  was calculated. Four locations were examined, which include an  $\text{H}^+$  bonded to *i*) the bridging oxygen between the silica tetrahedron and uranyl polyhedron, *ii*) the apical oxygen on the silica tetrahedron, *iii*) the interlayer water molecule forming hydronium, and *iv*) the neptunyl oxygen (Figure 5.4). Reaction 6 describes the incorporation of  $\text{Np}^{5+}$  and  $\text{H}^+$  into the boltwoodite structure, where the source for  $\text{Np}^{5+}$  is  $\text{Np}_2\text{O}_5$ , the source for  $\text{H}^+$  is  $\text{H}_2\text{O}$ , and the sink for  $\text{U}^{6+}$  is  $\text{UO}_3$ .



Based on the calculated incorporation energies (inset of Figure 5.4), the most energetically-favored position for the additional  $\text{H}^+$  in the modified boltwoodite structure is bonded to the neptunyl oxygen, which results in an incorporation energy of 0.79 eV (76.2 kJ/mol).

According to the bond-valence calculations, the bonds within the uranyl ion are nearly satisfied; therefore, the uranyl oxygen is rarely involved in additional bonding.

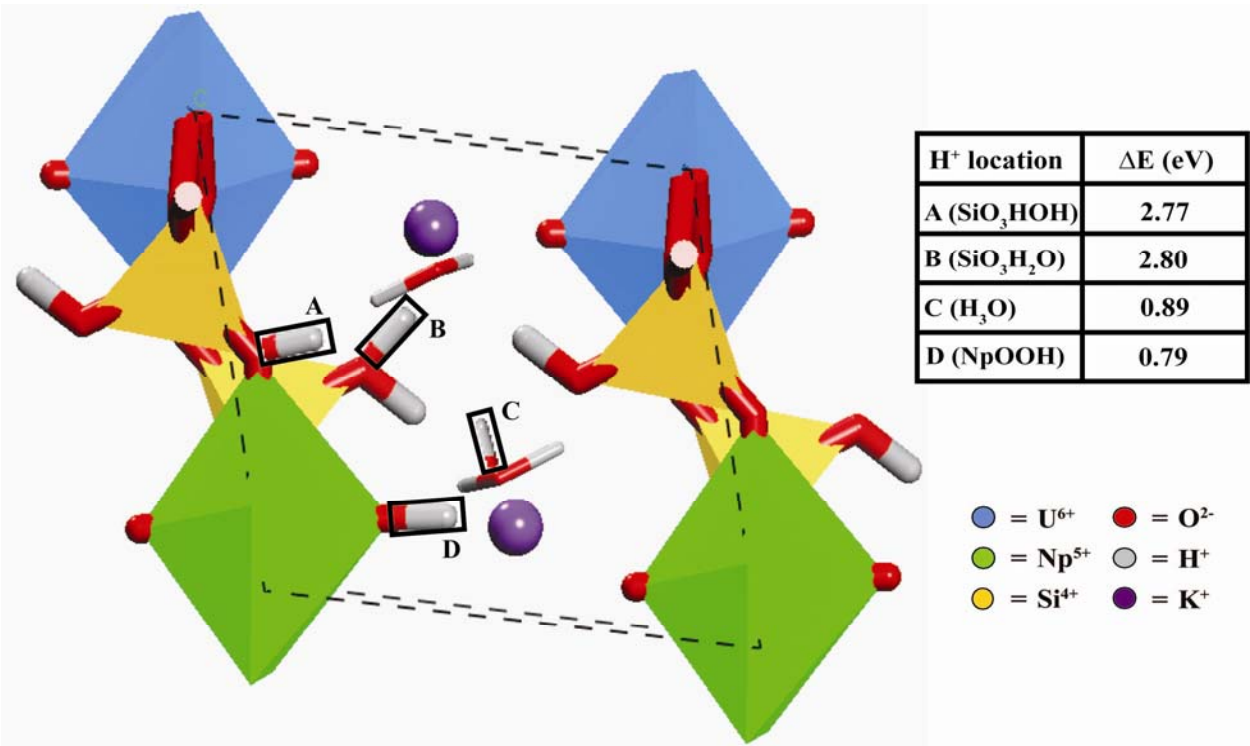


Figure 5.4. Boltwoodite unit cell showing possible locations for the charge-balancing H<sup>+</sup>. The table inset shows the Np-incorporation energy based for each H<sup>+</sup> location.

Since the bond strength (bond valence) of a  $\text{Np}^{5+}$  neptunyl ion is less than that of a  $\text{U}^{6+}$  uranyl ion, the neptunyl bond length is generally shorter (1.84 Å), and the neptunyl oxygen may be involved in additional bonding. For example, cation-cation interactions are often observed in  $\text{Np}^{5+}$ -bearing phases, whereas the oxygen of one neptunyl polyhedron is the equatorial ligand of the neighboring neptunyl polyhedron (Forbes et al., 2008; Sullivan et al., 1961). While an additional  $\text{H}^+$  ion bonded to the neptunyl oxygen may cause the oxygen to be overbonded, an extension of the  $\text{Np}-\text{O}$  bond length and the influence of the secondary bonding between the interlayer and the additional  $\text{H}^+$  ion may be enough to allow this coupled substitution to occur. The quantum-mechanically optimized  $\text{OH}^--\text{Np}^{5+}$  bond distance is 2.10 Å, while the other neptunyl  $\text{Np}-\text{O}$  bond distance is 1.88 Å. The 0.22 Å bond-length extension for the  $\text{OH}^--\text{Np}^{5+}$  bond distance is necessary in order to compensate for the overbonding of the  $\text{O}^{2-}$ .

***Substitution mechanism II:  $\text{Np}^{5+} + \text{Ca}(\text{Mg})^{2+} \leftrightarrow \text{U}^{6+} + \text{K}^+$***

For the coupled substitution of  $\text{Np}^{5+}$  and a divalent cation for  $\text{U}^{6+}$  and  $\text{K}^+$ , two divalent cations,  $\text{Ca}^{2+}$  and  $\text{Mg}^{2+}$ , were compared (Table 5.2) with two possible co-substitution sites in the interlayer (Figure 5.5). The distances between the substituted  $\text{Np}^{5+}$  polyhedron and sites A and B are 4.07 Å and 4.46 Å, respectively. Site A, the site closer to the substituted  $\text{Np}^{5+}$  polyhedron, is more energetically favored than site B by 2.1 eV (203 kJ/mol) and 1.3 eV (125 kJ/mol) for  $\text{Ca}^{2+}$  and  $\text{Mg}^{2+}$  substitution, respectively. Overall,  $\text{Ca}^{2+}$  substitution requires less energy than  $\text{Mg}^{2+}$  substitution at site A by 0.60 eV (63 kJ/mol), and the quantum-mechanically optimized distance between the  $\text{Ca}^{2+}$  and  $\text{Np}^{5+}$  is 3.80 Å.

Table 5.2. Incorporation energies for coupled substitution of  $\text{Np}^{5+}$  and  $\text{Ca}^{2+}$  or  $\text{Mg}^{2+}$  for  $\text{U}^{6+}$  and  $\text{K}^+$  in boltwoodite. Both interlayer sites are compared.

(units = eV)	$\text{Ca}^{2+}$ substitution	$\text{Mg}^{2+}$ substitution	Difference between cations
Site A	2.39	2.99	0.60
Site B	4.50	4.31	-0.19
Difference between Sites	2.11	1.32	--

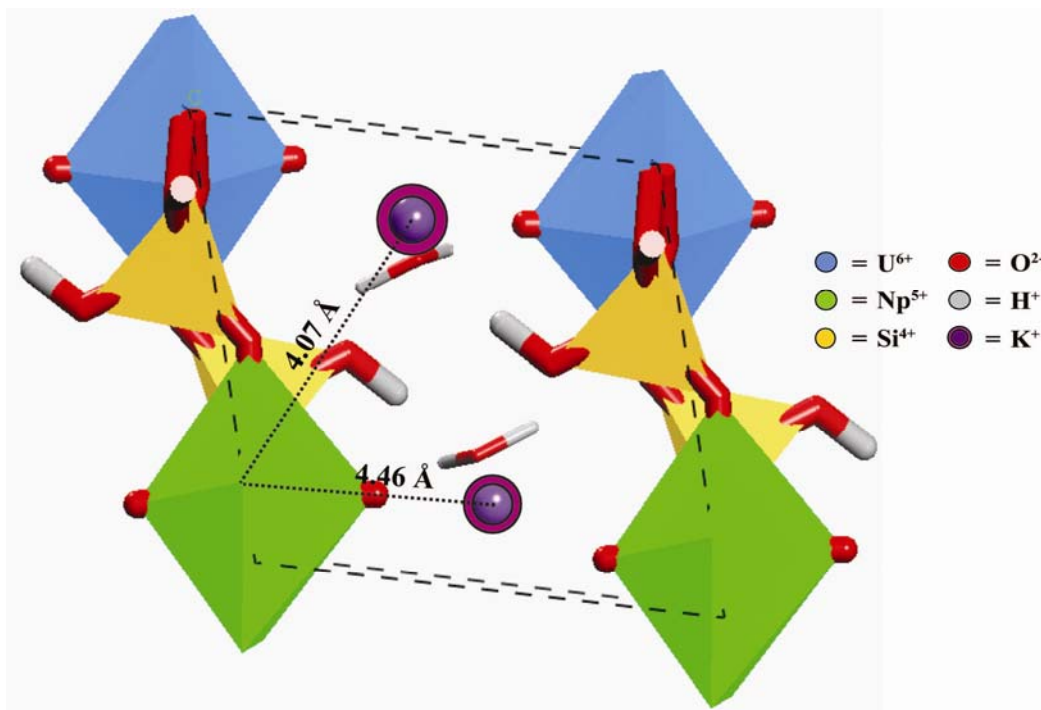


Figure 5.5. Boltwoodite unit cell indicating the distance between the two possible interlayer-cation substitution sites and the neptunium polyhedron.

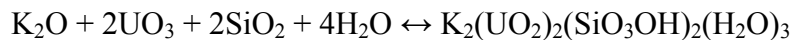
### ***Substitution mechanism III: $Np^{5+} + P^{5+} \leftrightarrow U^{6+} + Si^{4+}$***

The substitution of a  $P^{5+}$  for a  $Si^{4+}$  was compared for the two tetrahedral sites within a single boltwoodite unit cell. The uranyl chains, which polymerize in the [010] direction, are connected by edge- and corner-sharing Si-tetrahedra to form sheets (Figure 5.2a). For 50% Np substitution, which is the only concentration calculated due to the size of the unit cell, there are two unique tetrahedral sites: *i*) both edge- and corner-sharing with the substituted neptunyl and *ii*) only corner-sharing with the substituted neptunyl. The most energetically-favored site for the coupled-substitution of  $P^{5+}$  is the  $Si^{4+}$ -site that is both edge- and corner-sharing with the substituted neptunyl, which has a Np-P distance of 3.17 Å.

## **Discussion**

### ***Reference phase comparison***

A direct comparison of the total energies of boltwoodite and the Np-modified boltwoodite provides no information on the thermodynamics of incorporation because the two structures are not stoichiometrically equivalent. The energy of formation for the two phases may be compared based on the formation from the elements (*e.g.*, Ostanin and Zeller, 2007) or the oxides (*e.g.*, formation of boltwoodite in Reaction 7).



$$\Delta E_{formation} = 466.97 \text{ eV (7)}$$

To more accurately evaluate the energy required to substitute one  $Np^{5+}$  for one  $U^{6+}$ , the incorporation energy was evaluated and has been documented in the above results. The incorporation energy is calculated based on a stoichiometric chemical reaction that

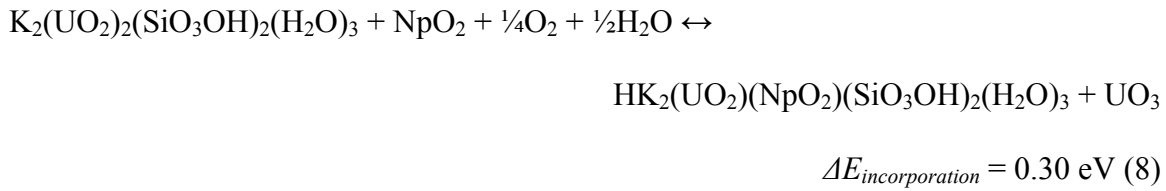
describes the incorporation (*e.g.*, Reaction 8), where the main mineral phase (boltwoodite) is the primary reactant and the modified mineral phase (Np-substituted boltwoodite) is the primary product. The sources and sinks for the cations involved in the reaction are referred to as reference phases. The choice of the reference phases greatly changes the final incorporation energy due the relative stability of the reference phases (Shuller et al., 2010). Several factors influence the choice of the reference phase for a particular calculation including the element for substitution, the oxidation state of the substituted element in the primary phase (either product or reactant), the environmental conditions that facilitate substitution, and limitations based on the chosen computational approach (*i.e.*, cluster *versus* periodic calculations).

The first two criteria are relatively straightforward. Obviously, if one is substituting Np for U, than the source and sink phases must contain those elements. Avoiding oxidation state change between the source phase and the primary product (*e.g.*, Np in source and Np in product) simplifies the reaction because no oxidant or reductant is needed; however, it is not necessary for the cations in question to have the same oxidation state in the source/sink phase and the primary product/reactant phase. For example, the oxide sources/sinks with different cation oxidation states were compared. Table 5.3 lists the incorporation reactions and incorporation energies calculated with different oxide reference phases (NpO<sub>2</sub>, Np<sub>2</sub>O<sub>5</sub>, UO<sub>2</sub>, and UO<sub>3</sub>) for Np<sup>5+</sup> and U<sup>6+</sup>. Gaseous oxygen (O<sub>2</sub>) is used as the oxidant or reduction product, and in the standard way of deriving redox reactions, H<sup>+</sup> and H<sub>2</sub>O are used to balance the charge and stoichiometry, respectively. For example, Reaction 8 describes the substitution of Np<sup>5+</sup> and H<sup>+</sup> for U<sup>6+</sup> in boltwoodite, where the source for Np is NpO<sub>2</sub> and the sink for U is

Table 5.3. Stoichiometric reactions describing the coupled-substitution of  $\text{Np}^{5+}$  and  $\text{H}^+$  for  $\text{U}^{6+}$  in boltwoodite comparing the Np-oxide sources and U-oxide sink phases.

<b>Reactants</b>	$\leftrightarrow$	<b>Products</b>	<b>E (eV)</b>
$\text{bolt} + \text{NpO}_2 + \frac{1}{4}\text{O}_2 + \frac{1}{2}\text{H}_2\text{O}$	$\leftrightarrow$	$(\text{bolt} - \text{U}^{6+} + \text{Np}^{5+} + \text{H}^+) + \text{UO}_3$	<b>0.30</b>
$\text{bolt} + \frac{1}{2}\text{Np}_2\text{O}_5 + \frac{1}{2}\text{H}_2\text{O}$	$\leftrightarrow$	$(\text{bolt} - \text{U}^{6+} + \text{Np}^{5+} + \text{H}^+) + \text{UO}_3$	<b>0.79</b>
$\text{bolt} + \text{NpO}_2 + \frac{1}{2}\text{H}_2\text{O}$	$\leftrightarrow$	$(\text{bolt} - \text{U}^{6+} + \text{Np}^{5+} + \text{H}^+) + \text{UO}_2 + \frac{1}{4}\text{O}_2$	<b>2.16</b>
$\text{bolt} + \frac{1}{2}\text{Np}_2\text{O}_5 + \frac{1}{2}\text{H}_2\text{O}$	$\leftrightarrow$	$(\text{bolt} - \text{U}^{6+} + \text{Np}^{5+} + \text{H}^+) + \text{UO}_2 + \frac{1}{2}\text{O}_2$	<b>2.65</b>

$\text{UO}_3$ .  $\text{O}_2$  is necessary to oxidize  $\text{Np}^{4+}$  to  $\text{Np}^{5+}$ , while  $\text{H}_2\text{O}$  is the source for  $\text{H}^+$  and to balance the stoichiometry.

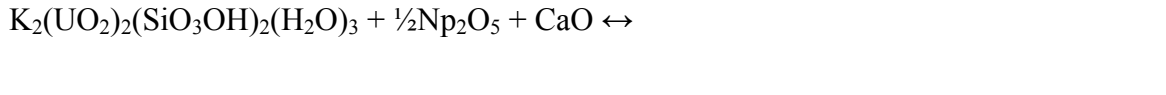


The lowest incorporation energy is achieved using  $\text{NpO}_2$  as the source for  $\text{Np}^{5+}$  and  $\text{UO}_3$  as the sink for  $\text{U}^{6+}$ . As detailed in Shuller et al. (2010), the  $\text{NpO}_2$  reference phase results in the lowest incorporation energy because  $2 \text{ NpO}_2 + \frac{1}{2} \text{ O}_2$  are less stable than  $\text{Np}_2\text{O}_5$ ; therefore, providing a larger driving force for the incorporation reaction.

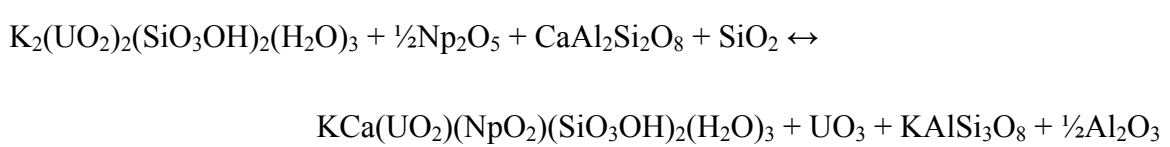
However, since  $\text{Np}_2\text{O}_5$  is the more stable phase under oxidizing conditions, the remaining comparisons using solid reference phases are completed with  $\text{Np}_2\text{O}_5$  as the source for  $\text{Np}$  and  $\text{UO}_3$  as the sink for  $\text{U}$ . In addition, this choice provides a reference phase in which the cations are in the same oxidation state as in the primary reactant/product.

While the simple binary oxide reference phases may be the logical crystalline reference phase choice for  $\text{Np}$  and  $\text{U}$ , binary oxides are not always the best choice for other cations involved in the coupled substitution. The incorporation mechanism that involves coupled substitution in the interlayer requires reference phases for the divalent ( $\text{Ca}^{2+}, \text{Mg}^{2+}$ ) and monovalent ( $\text{K}^+, \text{Na}^+$ ) interlayer cations involved in the substitution. The oxide source for  $\text{Ca}^{2+}$  and sink for  $\text{K}^+$  are chosen to be  $\text{CaO}$  and  $\text{K}_2\text{O}$ , respectively. These oxide reference phases have small unit cells, which is conducive for quantum-mechanical calculations; however, these oxides are not prevalent in nature, indicating that they are not stable with respect to other mineral phases in most geologic settings and, thus, not a likely cation source in the environment. Thus, oxide reference phases

(Reaction 9) were compared with silicate reference phases (Reaction 10) for the interlayer cation coupled-substitution mechanism. The silicate phases selected, feldspars, are ubiquitous in nature. The silicate source selected for  $\text{Ca}^{2+}$  is anorthite ( $\text{CaAl}_2\text{Si}_2\text{O}_8$ ), and the sink for  $\text{K}^+$  is K-feldspar ( $\text{KAlSi}_3\text{O}_8$ ) while  $\alpha$ -quartz ( $\text{SiO}_2$ ) and corundum ( $\text{Al}_2\text{O}_3$ ) are the sources for Si and sinks for Al, respectively.



$$\Delta E_{oxides} = 2.40 \text{ eV} \quad (9)$$



$$\Delta E_{silicates} = 1.20 \text{ eV} \quad (10)$$

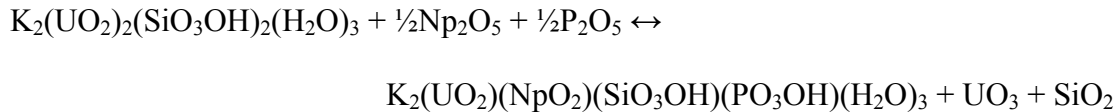
Experimental enthalpies of formation for the interlayer cation reference phases are taken from the literature (Robie and Hemingway, 1995). Thus, the change in enthalpy of Reaction 11 (1.2 eV) is the energy difference between the oxide reference phase scenario to the silicate reference phase scenario ( $\Delta E^{\text{Reaction } 4} - \Delta E^{\text{Reaction } 5}$ ).



$$\Delta E_{literature} = 1.20 \text{ eV} \quad (11)$$

The substitution of  $\text{Np}^{5+}$  and  $\text{Ca}^{2+}$  for  $\text{U}^{6+}$  and  $\text{K}^+$  in boltwoodite results in an incorporation energy of 1.2 eV (115.8 kJ/mol), based on silicate reference phases.

Similarly, for the intralayer substitution mechanism,  $\text{P}_2\text{O}_5$  was selected as the source for  $\text{P}^{5+}$  and  $\text{SiO}_2$  as the sink for  $\text{Si}^{4+}$  (Reaction 12).



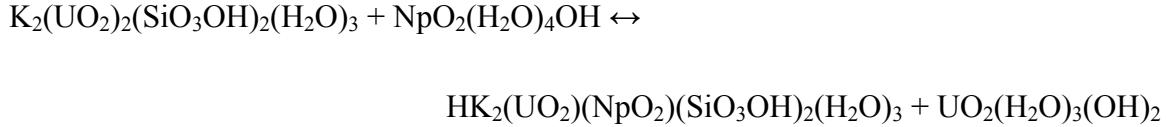
$$\Delta E_{oxides} = -1.10 \text{ eV (12)}$$

However, the resulting incorporation energy is -1.10 eV, which indicates an infinite amount of  $\text{Np}^{5+}$  can be incorporated into boltwoodite. The solid solution calculations below show that a limited amount of  $\text{Np}^{5+}$  can be incorporated into boltwoodite based on the intralayer substitution mechanism. Changing the choice of the source phase for  $\text{P}^{5+}$  to berlinitite ( $\text{AlPO}_4$ ), where the added sink for the Al is corundum ( $\text{Al}_2\text{O}_3$ ), results in an incorporation energy (0.86 eV) that more suitably reflects expected environmental conditions. Thus, a consideration of the probability that the reference phase is present in a specific environment is necessary for obtaining a more realistic estimate of the incorporation energy.

In reality, the source and sink phases for  $\text{Np}^{5+}$ ,  $\text{U}^{6+}$ , and other cations associated with the incorporation reaction are often *not* solid mineral phases, but rather aqueous complexes (even though the aqueous complex may stem from dissolution of a solid phase). This is especially true if the incorporation occurs via a co-precipitation of Np in boltwoodite or *via* a cation exchange mechanism. Typically, aqueous actinides form complexes with ligands available in groundwater. For example, aqueous actinides in groundwater containing small concentrations of dissolved carbonate will readily form actinyl-carbonate complexes (Choppin, 2007). For computational purposes, simple aqueous species, such as actinyl complexes (*e.g.*,  $\text{NpO}_2^{+ \text{aq}}$ ) were selected as sources and sinks to describe the incorporation reaction for the  $\text{H}^+$  incorporation mechanism.

In periodic quantum-mechanical calculations, the energy of charged species becomes awkward to handle, as part of a contribution to the overall energy of the system is caused by a non-physical interaction between the ion and a “smeared-out” charge-neutralizing background charge. Charged aqueous species can conveniently be calculated using cluster-type quantum-mechanical calculations; however, total energies for compounds within one reaction should typically be calculated using the same theory. Thus, it is important to ensure that the energy contributions to a reaction energy are independent of the method. One way around this problem is to compose an overall reaction equation that is composed of sub-reactions, each of which is calculated using a consistent approach, but different sub-reactions may be calculated using different approaches that are, respectively, most suitable to handle specific boundary conditions, *i.e.*, extended solids, or finite molecules that may carry a charge. Instead, the energy of neutral complexes are calculated using the periodic approach implemented in CASTEP (Reaction 13), and subsequently converted to the charged complexes using Dmol<sup>3</sup> calculations (Delley, 1990; Delley, 1991). Dmol<sup>3</sup> is a density functional theory code that uses atomistic basis sets to approximate the electron density for both periodic and cluster calculations. The hydration energy is estimated based on the COSMO implementation in Dmol<sup>3</sup>, which uses the interaction between a molecule and a dielectric fluid to approximate the hydration of a molecule.

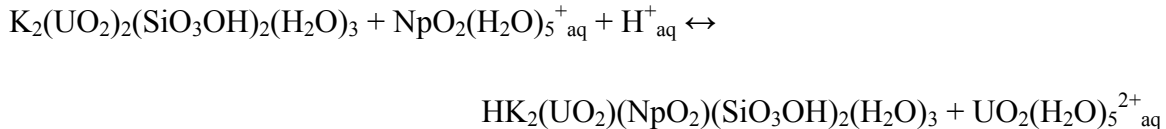
The reaction based on neutral complexes (Reaction 13) is converted to one based on charged aqueous complexes via Reaction 10a, where the difference between Reaction 13 and Reaction 14a describes Np-incorporation based on aqueous species, including H<sup>+</sup><sub>aq</sub> (Reaction 14b).



$$\Delta E_{incorporation} = 0.32 \text{ eV} \quad (13)$$



$$\Delta E = 5.33 \text{ eV} \quad (14a)$$

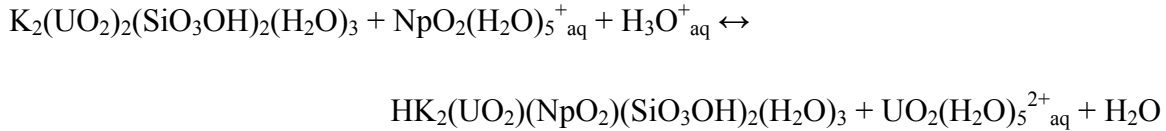


$$\Delta E_{incorporation} = -5.01 \text{ eV} \quad (14b)$$

The large negative  $\Delta E$  for aqueous reference species indicates that an infinite amount of Np would be incorporated into boltwoodite; however, solid solution calculations shown below indicate limited incorporation. Thus, the large negative  $\Delta E$  (Reaction 14b) is a result of the free  $\text{H}^+_{\text{aq}}$  as a H source, while the highly positive  $\Delta E$  in Eqn. 14a stems from  $\text{H}^+$  being the H sink. In natural solutions,  $\text{H}^+$  is not usually present as a free ion; rather,  $\text{H}^+$  is present in aqueous solutions as  $\text{H}_3\text{O}^+$ . The change in energy for the formation of  $\text{H}_3\text{O}^+$  from  $\text{H}_2\text{O}$  and  $\text{H}^+$  [ $\text{H}_2\text{O} + \text{H}^+ \leftrightarrow \text{H}_3\text{O}^+$ ] is -5.67 eV. Therefore, the charge distribution between the actinyl complexes becomes slightly favored (Reaction 15a), and the incorporation reaction for Np in boltwoodite with  $\text{H}_3\text{O}^+_{\text{aq}}$  as the source for  $\text{H}^+$  results in a slightly positive incorporation energy (Reaction 15b).



$$\Delta E = -0.34 \text{ eV} \quad (15a)$$



$$\Delta E_{incorporation} = 0.66 \text{ eV} \quad (15b)$$

To the authors' knowledge, this is the first time that this approach has been used for combining solid and aqueous components in quantum-mechanical calculations. Commonly, a pure cluster approach is used (*e.g.*, Becker et al., 1997); however, that was not possible due to the complexity of boltwoodite. Others have used programs (*e.g.*, CRYSTAL) that allow for the implementation of both periodic and cluster calculations using a consistent basis set (Civalleri et al., 2003; Skomurski et al., 2010). Using the method described above, not only the basis set, but the entire computational approach remains consistent throughout a total reaction involving finite charged and infinite neutral reactants/products, by summing over sub-reactions are each methodologically consistent.

### ***Limit of Np-incorporation***

The thermodynamically stable limit for Np-incorporation into the uranyl phases is estimated from these quantum-mechanical calculations by developing a theoretical solid-solution series. The coupled-substitution mechanisms in which  $\text{Np}^{5+}$  and  $\text{P}^{5+}$  replace  $\text{U}^{6+}$  and  $\text{Si}^{4+}$  were chosen as an example due to its low incorporation energy (0.86 eV) as compared with other coupled-substitution mechanisms. Additionally, the substitution occurs on established structural sites, therefore limiting the possibilities for different solid-solution configurations. The U-Si end-member for this solid solution series is boltwoodite, while the Np-P end-member is a boltwoodite with all of the  $\text{U}^{6+}$  replaced by  $\text{Np}^{5+}$  and  $\text{Si}^{4+}$  replaced with  $\text{P}^{5+}$ , *i.e.*,  $\text{K}_2(\text{NpO}_2)_2(\text{PO}_3\text{OH})_2(\text{H}_2\text{O})_3$ . Although this is Np-P-

boltwoodite phase has not been observed, it is used as a theoretical end-member in order to calculate the enthalpy of mixing for the intermediate composition. The boltwoodite unit cell has two unique  $\text{U}^{6+}$  sites and two unique  $\text{Si}^{4+}$  sites; therefore, the only intermediate composition calculated for a single unit cell has 50% of the polyhedra sites occupied by Np and 50% of the tetrahedral sites occupied by P, *i.e.*,  $\text{K}_2(\text{UO}_2)(\text{NpO}_2)(\text{SiO}_3\text{OH})(\text{PO}_3\text{OH})(\text{H}_2\text{O})_3$  (Figure 5.6).

The enthalpy of mixing across the compositional range ( $x$ ) is fit using a Margules function,  $\Delta H = Ax(1-x)$ , where the Margules parameter ( $A$ ) equals 35.5 kJ/(mol exchangeable cation). The resulting limit of Np-incorporation into boltwoodite with the  $\text{P}^{5+}$  charge-balanced mechanism is then predicted at a range of repository temperatures using the Gibbs free energy as approximated by the Margules function and the point entropy,  $\Delta S = -RT[x\ln x + (1-x)\ln(1-x)]$  (Table 5.4). At about 300 °C (573 K), the incorporation limit for Np in boltwoodite is  $\sim 585$  ppm, which is on the same order of magnitude (hundreds of ppm) as experimental results for Np-incorporation into uranyl structures with charged-interlayer cations (Burns et al., 2004; Burns and Klingensmith, 2006; Klingensmith and Burns, 2007; Klingensmith et al., 2007). The calculated incorporation limit is dependent on the enthalpy of mixing at the concentration used to calculate the Margules parameter. Only one configuration at 50% composition was calculated due to computational limitations; therefore, a precise error for the enthalpy of mixing cannot be determined. Assuming the error for the quantum-mechanical calculations is about 1%, the range for the incorporation limit at 300 °C is  $585 \pm 45$  ppm. Thus, an error of 1% in the enthalpy of mixing does not significantly change the incorporation limit. However, the incorporation limit is strongly affected by the

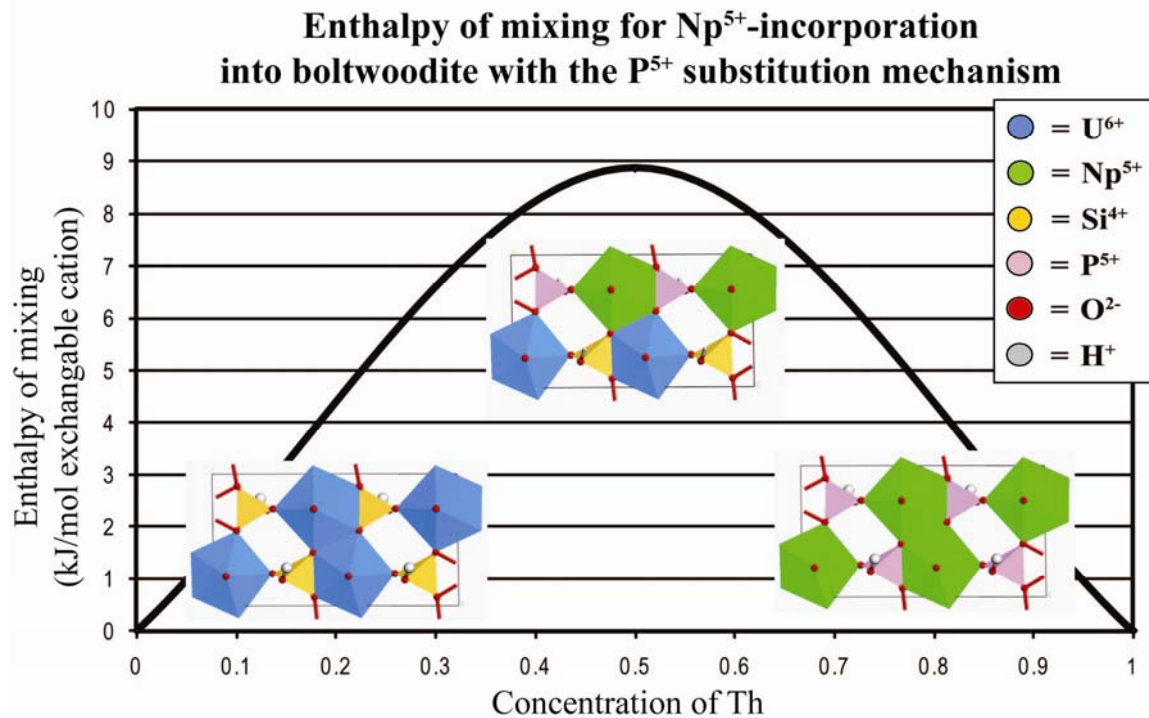


Figure 5.6. Enthalpy of mixing ( $\Delta H_{mix}$ ) *versus* composition for the solid-solution series based on the coupled substitution of  $\text{Np}^{5+}$  and  $\text{P}^{5+}$  for  $\text{U}^{6+}$  and  $\text{Si}^{4+}$ , where the end members are boltwoodite  $[\text{K}_2(\text{UO}_2)_2(\text{SiO}_3\text{OH})_2(\text{H}_2\text{O})_3]$  and a fully substituted boltwoodite  $[\text{K}_2(\text{NpO}_2)_2(\text{PO}_3\text{OH})_2(\text{H}_2\text{O})_3]$  and the calculated intermediate phase is a 50:50 composition  $[\text{K}_2(\text{UO}_2)(\text{NpO}_2)(\text{SiO}_3\text{OH})(\text{PO}_3\text{OH})(\text{H}_2\text{O})_3]$ .

Table 5.4. The estimated limit of Np-incorporation into boltwoodite for the coupled-substitution of  $\text{Np}^{5+}$  and  $\text{P}^{5+}$  for  $\text{U}^{6+}$  and  $\text{Si}^{4+}$  is tabulated as a function of temperature.

<b>Temperature (°C)</b>	<b>Estimated Np concentration [amount of Np/amount of (U+Np)]</b>	<b>Estimated Np concentration [ppm of total actinides (U+Np)]</b>
<b>100</b>	<b><math>1.07 \cdot 10^{-5}</math></b>	<b>10.7</b>
<b>150</b>	<b><math>4.13 \cdot 10^{-5}</math></b>	<b>41.3</b>
<b>200</b>	<b><math>1.20 \cdot 10^{-4}</math></b>	<b>120</b>
<b>300</b>	<b><math>5.85 \cdot 10^{-4}</math></b>	<b>585</b>

temperature of incorporation. While 585 ppm Np is incorporated into boltwoodite at 300 °C, only 10.7 ppm Np is incorporated at 100 °C. In reference to temperature, the calculations and experiments cannot be directly compared. The synthesis of boltwoodite occurs at 100 to 185 °C (Vochten et al., 1997; Wall et al., 2010); however, in natural environments different hydrothermal synthesis conditions may influence the formation of boltwoodite, and consequently, the incorporation of Np.

### ***Impact of boltwoodite chemistry on Np incorporation***

Ionic radii are often used as a first estimate for the thermodynamic stability of solid solutions, where, in this case, the coupled substitution of  $\text{Np}^{5+}$  and a divalent cation for  $\text{U}^{6+}$  and  $\text{K}^+$  would be considered a solid solution between  $\text{Np}^{5+}\text{Ca}^{2+}(\text{Mg}^{2+})$ -boltwoodite and  $\text{U}^{6+}\text{K}^+$ -boltwoodite. The coupled-substitution occurs in the interlayer either during the precipitation of the modified boltwoodite phase or via cation exchange. A comparison of the ionic radii of the interlayer cations (*i.e.*,  $\text{K}^+$ ,  $\text{Ca}^{2+}$ , and  $\text{Mg}^{2+}$ ) indicates that  $\text{Ca}^{2+}$  is more likely to substitute for  $\text{K}^+$  than  $\text{Mg}^{2+}$ , where the ionic radius for a  $\text{K}^+$  ion with a coordination number (CN) of VI is 1.38 Å, while the radii of  $\text{Ca}^{2+}$  and  $\text{Mg}^{2+}$  with the same coordination number are 1.00 Å and 0.72 Å, respectively (Shannon, 1976). As previously discussed, the computational results agree with the hypothesis that the divalent cation with an effective ionic radius that is more similar to the monovalent cation is more likely to substitute. Interestingly, the ionic radius of  $\text{Na}^+$  (CN = VI) is 1.02 Å, which indicates, based solely on ionic radii, that  $\text{Ca}^{2+}$  would even more readily substitute into the interlayer of  $\text{Na}^+$ -bearing boltwoodite. Synthetic boltwoodite has been shown to contain both  $\text{K}^+$  and  $\text{Na}^+$  in the interlayer, and it has been hypothesized that the complete

solid solution of  $\text{K}^+$ - $\text{Na}^+$ -boltwoodite is possible (Burns, 1998). Further calculations and experiments would be necessary to determine the effect of interlayer composition on  $\text{Np}^{5+}$ -incorporation energy and its incorporation limit.

### ***Feasibility of reaction mechanisms***

The feasibility of  $\text{Np}^{5+}$  incorporation into boltwoodite depends on more than just the incorporation energy, *i.e.*, the thermodynamics of incorporation, which is subject to the substitution mechanism and the source/sink phases chosen. In addition, the kinetics of incorporation and the availability of co-reactants are crucial to the feasibility of the final mixed  $\text{Np}$ -U phase.  $\text{Np}$  may be incorporated into boltwoodite via cation exchange after the boltwoodite has already precipitated or by coprecipitation of the mineral. Cation exchange is a common immobilization mechanism for groundwater contaminants and is often observed in cage-like or layered structures such as zeolites (Kesraouiouki et al., 1994; Shi et al., 2009) or clays (Rosso et al., 2001). Many uranyl minerals, including boltwoodite, form layered structures; thus, cation exchange between the interlayer of uranyl minerals and the groundwater is probable. One study of particular importance has shown  $\text{Cs}^+$ -exchange into the interlayer of boltwoodite, with the resulting structural formula  $\text{Cs}[(\text{UO}_2)(\text{SiO}_3\text{OH})]$  (Burns, 1999b). Thus, cation exchange in boltwoodite has been shown to occur experimentally and most likely occurs due to the stability of the structural sheets.

However, for  $\text{Np}^{5+}$ -incorporation into boltwoodite *via* cation exchange, the  $\text{Np}^{5+}$  and other charge-balancing cations need to not only go into the interlayer, but also diffuse into the structural sheets. For example, if  $\text{NpO}_2^+$  is meant to replace  $\text{UO}_2^{2+}$ , the  $\text{NpO}_2^+_{\text{aq}}$

must first exchange into the interlayer and then exchange from the interlayer into the sheet, replacing the  $\text{UO}_2^{2+}$ . A charge-balancing cation would need to go into the interlayer as well. Another incorporation mechanism that has not yet been explored is the exchange of  $\text{NpO}_2^+$  for  $\text{K}^+$  in the interlayer. However, the  $\text{NpO}_2^+$  is much larger than  $\text{K}^+$ . Boltwoodite has shown enough structural flexibility to cation-exchange the large  $\text{Cs}^+$  for the  $\text{K}^+$  in the interlayer; however, such cation-exchange required the loss of all interlayer water groups (Burns, 1999b). Thus, further flexibility of the structure may not be possible. Purely based on size and availability, the incorporation of a  $\text{H}^+$  may be more likely than the exchange of a divalent cation for a monovalent cation in the interlayer, and this appears to be a more likely kinetic path than the exchange of a phosphate for the silicate in the structural sheet. There, the main kinetic bottleneck may be the formation of an  $\text{H}^+$  from  $\text{H}_3\text{O}^+$ .

The incorporation of  $\text{Np}^{5+}$  and  $\text{P}^{5+}$  into boltwoodite during the initial precipitation, essentially coprecipitation, is more likely than cation exchange, but requires the availability of both  $\text{Np}^{5+}$  and  $\text{P}^{5+}$  during precipitation.  $\text{Np}^{5+}$ , as previously discussed, is expected to be available in oxidizing aqueous solutions near used nuclear fuel. Aqueous phosphate may also be present in the groundwater from common phosphate minerals in the soil or from anthropogenic sources. For example, phosphorus from fertilizers and TBP (tributyl phosphate), which was used in uranium processing, are concentrated in the contaminated soils at the Fernald site in Ohio (Buck et al., 1996). Natural and synthetic boltwoodite is well-documented (Burns, 1998; Deditius et al., 2008; Finch and Murakami, 1999; Frondel and Ito, 1956; Stohl and Smith, 1981; Wong et al., 1999); however, a  $\text{Np}^{5+}\text{P}^{5+}$ -boltwoodite has not been reported. A comparison of the polyhedral

geometries and anion topologies of neptunyl and uranyl compounds highlights similarities and differences between the structures and may indicate the feasibility of the formation of a  $\text{Np}^{5+}\text{P}^{5+}$ -boltwoodite.

Like the uranyl compounds, the neptunyl compounds can be categorized into hierarchical groups based on the connectivity of the neptunyl polyhedra (Forbes et al., 2008). Such groups include isolated and finite clusters, chains of polyhedra, sheets of polyhedra, and frameworks of polyhedra. The main difference between  $\text{Np}^{5+}$  and  $\text{U}^{6+}$  compounds is the overwhelming presence of cation-cation interactions (CCIs) in the neptunyl compounds. CCIs are defined as two cations bonded *via* an oxygen atom, where the oxygen is in equatorial relation to one cation, yet axial to the other. Thus, CCIs allow the cations to be closer to one another than if the bipyramids are bonded *via* shared equatorial oxygen atoms. Compared to the high number of neptunyl structures with CCIs (18 of 43 known inorganic  $\text{Np}^{5+}$  compounds), only less than two percent of uranyl structures contain CCIs. The limited occurrences of CCIs in uranyl structures is probably because the uranyl  $\text{U}^{6+}$ -O bond strength satisfies the bonding requirements of the O atom (Burns, 2005; Burns and Klingensmith, 2006; Forbes et al., 2008), whereas the neptunyl bond strength is weaker. Thus, the neptunyl O can bond to other  $\text{Np}^{5+}$  atoms at distances equal to that of a typical equatorial bond.

While most of the  $\text{Np}^{5+}$ -compounds that contain CCIs are framework-type structures, four compounds containing CCIs exist with sheet topologies. Additionally, of the 24  $\text{Np}^{5+}$ -compounds without CCIs, 12 polymerize into sheet structures, which are the most common type of polymerization for  $\text{U}^{6+}$ -compounds. More so, several  $\text{Np}^{5+}$  sheet compounds have similar anion topology to  $\text{U}^{6+}$  sheet compounds, indicating a structural

relationship. Several  $\text{U}^{6+}$ -silicates, including boltwoodite, have the  $\alpha$ -uranophane anion topology (Figure 5.7), for which chains of edge-sharing pentagons (typically uranyl polyhedra) are connected by alternating edge-sharing triangles (typically silica tetrahedra) and squares (Burns, 1999a). However, a comparison of  $\text{U}^{6+}$ - and  $\text{Np}^{5+}$ -silicate topology reveals no structure types with the same topology. None of the  $\text{Np}^{5+}$ -silicates that have been synthesized, thus far, have the  $\alpha$ -uranophane anion sheet topology (*e.g.*,  $\text{Li}_6(\text{NpO}_2)_4(\text{H}_2\text{Si}_2\text{O}_7)(\text{HSiO}_4)_2(\text{H}_2\text{O})_4$  has the  $\beta$ - $\text{U}_3\text{O}_8$  anion-topology) (Forbes and Burns, 2008). Direct comparisons between the anion topology of U and Np compounds have only been identified for the hexavalent cations. For example, the  $\text{Np}^{6+}$ -phosphates [ $\text{X}(\text{NpO}_2)(\text{PO}_4)(\text{H}_2\text{O})_3$ ;  $\text{X} = \text{K}^+, \text{Na}^+, \text{Rb}^+, \text{NH}_4^+$ ] adopt the anion topology of autunite, a  $\text{U}^{6+}$ -phosphate [ $\text{Ca}(\text{UO}_2)(\text{PO}_4)_2(\text{H}_2\text{O})_{11}$ ] (Forbes and Burns, 2007; Locock and Burns, 2003). While an  $\text{Np}^{6+}$ -silicate has not yet been synthesized, one might predict, based on the relation of the  $\text{Np}^{6+}$ - and  $\text{U}^{6+}$ -phosphates, that a  $\text{Np}^{6+}$ -silicate with the same chemistry as boltwoodite may form as a similar structure.

Interestingly, the  $\text{Np}^{5+}$ -phosphate [ $\text{Ba}(\text{NpO}_2)(\text{PO}_4)(\text{H}_2\text{O})$ ] adopts the same  $\alpha$ -uranophane anion topology as boltwoodite (Forbes and Burns, 2006). While the interlayer cation (Ba) is divalent, which differs from the monovalent  $\text{K}^+$  or  $\text{Na}^+$  of boltwoodite, the charge is balanced by the lack of extra  $\text{H}^+$ . The structural similarity between the  $\text{Np}^{5+}$ -phosphate and the  $\text{U}^{6+}$ -silicate may indicate the likelihood of the coupled-substitution of  $\text{Np}^{5+}$  and  $\text{P}^{5+}$  for  $\text{U}^{6+}$  and  $\text{Si}^{4+}$  in boltwoodite.

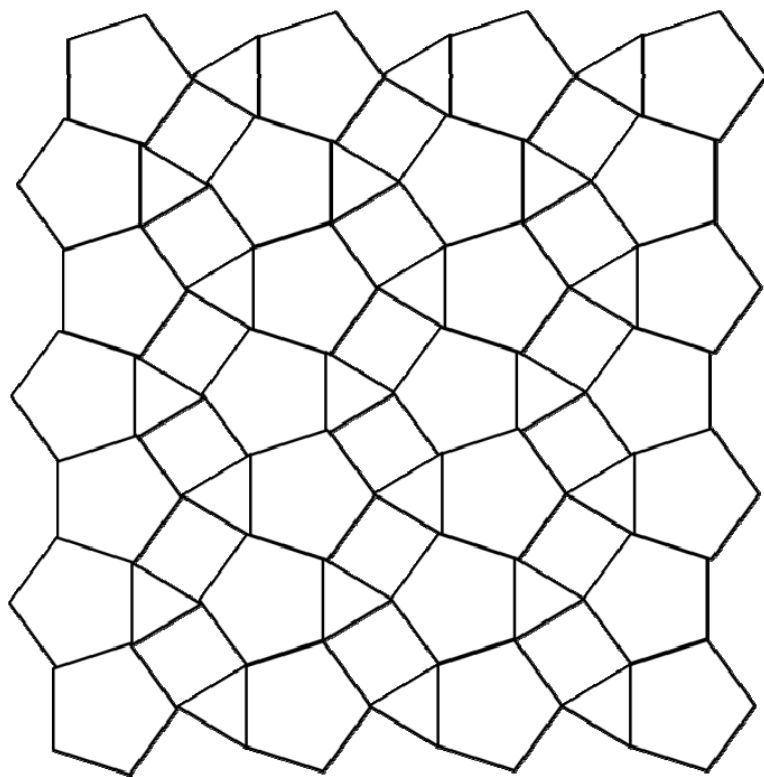


Figure 5.7. Schematic of the alpha-uranophane anion topology, composed of chains of edge-sharing pentagons connected by chains of alternating edge-sharing triangles (typically silica tetrahedra) and squares. Modified from (Burns, 1999a).

## Implications

About 500 ppm Np is in the used nuclear fuel from a reactor with a burnup of 40 MWd/kg of U (MegaWatt days/kg of uranium), and the amount of Np increases over time due to the decay of  $^{241}\text{Am}$ . Murphy and Grambow (2008) note that the amount of Np in used nuclear fuel is about 1000 ppm at 200 years due to increasing amounts of  $^{237}\text{Np}$  from decay of  $^{241}\text{Am}$ . However, solubility studies indicate that less Np would be available in a geologic repository (~2-200 ppm) (Efurd et al., 1998; Nitsche, 1991). Additionally, performance assessment studies have adopted much lower solubility limits (*e.g.* 0.1 to 1 ppm; Sassani et al., 2006). While geochemical modeling of Np-incorporation into the uranium(VI) silicate uranophane indicates that Np is relatively excluded from the uranyl mineral structure (Murphy and Grambow, 2008), the aqueous speciation and thermodynamic properties used in the modeling are uncertain. Based on the laboratory experiments and atomistic calculations the aqueous Np at a geologic repository could be limited via co-precipitation into uranyl minerals.

Burns et al. (2004) showed that 400 ppm (0.4 mg Np/g U+Np) Np can be incorporated into uranyl phases with interlayer cations (*e.g.*, Na-compreignacite synthesized at 100 °C). Similarly, calculated incorporation limits indicate that over 100 ppm Np can be incorporated into boltwoodite at 200 °C. Based on solubility studies, the amount of Np available in solution will not reach the capacity of uranyl minerals with interlayer cations; thus, Np-incorporation is a viable mechanism for limiting the mobility of aqueous Np in an oxidizing geologic repository environment.

Thus far, calculations and experiments on Np-incorporation into uranyl phases have only shown the capacity of uranyl minerals for Np. However, the kinetics of incorporation will determine the feasibility of the use of uranyl minerals for the immobilization of Np in a geologic environment. For example, Np (or  $\text{NpO}_2^+$ ) diffusion rates for different pathways through the mineral structure may reveal energy barriers for diffusion of the ion from the interlayer into the structural sheet. Furthermore, competitive cation-exchange reactions will determine which contaminants are more likely to be immobilized in specific uranyl minerals. Cation exchange of  $\text{Cs}^+$  in boltwoodite is the only documented experiment of cation exchange in a uranyl mineral, but further work can clarify the role of uranyl minerals for the immobilization of radionuclides. Calculations, like those presented here, can be used to guide experiments in terms of possible incorporation mechanisms. For example, the calculations indicate that substitution in the interlayer requires the least amount of energy when the exchanged cations have similar ionic radii. A complementary experiment could be done to test the incorporation limit of  $\text{Np}^{5+}$  in boltwoodite with varying interlayer compositions between pure K-boltwoodite to pure Na-boltwoodite. Likewise, the experimental set-up can be used to guide calculations. Using the method developed here for using aqueous molecular source and sink phases, calculations on incorporation energy can more accurately model synthesis experiments.

## References

Becker, U., Hochella, M.F., and Vaughan, D.J. (1997) The adsorption of gold to galena surfaces: Calculation of adsorption/reduction energies, reaction mechanisms, XPS

- spectra, and STM images. *Geochimica Et Cosmochimica Acta*, 61(17), 3565-3585.
- Buck, E.C., Brown, N.R., and Dietz, N.L. (1996) Contaminant uranium phases and leaching at the Fernald site in Ohio. *Environmental Science & Technology*, 30(1), 81-88.
- Buck, E.C., Finch, R.J., Finn, P.A., and Bates, J.K. (1998) Retention of neptunium in uranyl alteration phases formed during spent fuel corrosion. *Scientific Basis for Nuclear Waste Management XXI*, 506, 87-94.
- Buck, E.C., Hanson, B.D., Friese, J.I., Douglas, M., and McNamara, B.K. (2004) Evidence for neptunium incorporation into uranium (VI) phases. *Scientific Basis for Nuclear Waste Management XXVIII*, 824, 133-138.
- Burns, P.C. (1998) The structure of boltwoodite and implications of solid solution toward sodium boltwoodite. *Canadian Mineralogist*, 36, 1069-1075.
- (1999a) The crystal chemistry of uranium. In P.C. Burns, and R. Finch, Eds. *Uranium: Mineralogy, Geochemistry, and the Environment*, 38, p. 23-90.
  - (1999b) Cs boltwoodite obtained by ion exchange from single crystals: Implications for radionuclide release in a nuclear repository. *Journal of Nuclear Materials*, 265(1-2), 218-223.
  - (2005)  $U^{6+}$  minerals and inorganic compounds: Insights into an expanded structural hierarchy of crystal structures. *Canadian Mineralogist*, 43, 1839-1894.
- Burns, P.C., Deely, K.M., and Skanthakumar, S. (2004) Neptunium incorporation into uranyl compounds that form as alteration products of spent nuclear fuel: Implications for geologic repository performance. *Radiochimica Acta*, 92(3), 151-159.
- Burns, P.C., Ewing, R.C., and Miller, M.L. (1997) Incorporation mechanisms of actinide elements into the structures of  $U^{6+}$  phases formed during the oxidation of spent nuclear fuel. *Journal of Nuclear Materials*, 245(1), 1-9.
- Burns, P.C., and Klingensmith, A.L. (2006) Uranium mineralogy and neptunium mobility. *Elements*, 2(6), 351-356.

- Catlow, C.R.A. (1987) Recent Problems and Progress in the Study of UO<sub>2</sub> and Mixed UO<sub>2</sub>-PuO<sub>2</sub>. *Journal of the Chemical Society-Faraday Transactions II*, 83, 1065-1072.
- Choppin, G.R. (2007) Actinide speciation in the environment. *Journal of Radioanalytical and Nuclear Chemistry*, 273(3), 695-703.
- Civalleri, B., Ferrari, A.M., Llunell, M., Orlando, R., Merawa, M., and Ugliengo, P. (2003) Cation selectivity in alkali-exchanged chabazite: An ab initio periodic study. *Chemistry of Materials*, 15(21), 3996-4004.
- Deditius, A.P., Utsunomiya, S., and Ewing, R.C. (2008) The chemical stability of coffinite, USiO<sub>4</sub>·nH<sub>2</sub>O; 0 < n < 2, associated with organic matter: A case study from Grants uranium region, New Mexico, USA. *Chemical Geology*, 251(1-4), 33-49.
- Delley, B. (1990) An all-electron numerical-method for solving the local density functional for polyatomic-molecules. *Journal of Chemical Physics*, 92(1), 508-517.
- (1991) Dmol methodology and applications. *Density Functional Methods in Chemistry*, 101-107.
- Douglas, M., Clark, S.B., Friese, J.I., Arey, B.W., Buck, E.C., Hanson, B.D., Utsunomiya, S., and Ewing, R.C. (2005) Microscale characterization of uranium(VI) silicate solids and associated neptunium(V). *Radiochimica Acta*, 93(5), 265-272.
- Efurd, D.W., Runde, W., Banar, J.C., Janecky, D.R., Kaszuba, J.P., Palmer, P.D., Roensch, F.R., and Tait, C.D. (1998) Neptunium and plutonium solubilities in a Yucca Mountain groundwater. *Environmental Science & Technology*, 32(24), 3893-3900.
- Ferriss, E.D.A., Essene, E.J., and Becker, U. (2008) Computational study of the effect of pressure on the Ti-in-zircon geothermometer. *European Journal of Mineralogy*, 20(5), 745-755.

- Ferriss, E.D.A., Ewing, R.C., and Becker, U. (2010) Simulation of thermodynamic mixing properties of actinide-containing zircon solid solutions. *American Mineralogist*, 95(2-3), 229-241.
- Finch, R., and Ewing, R.C. (1992) Corrosion of uraninite under oxidizing conditions. *Journal of Nuclear Materials*, 190, 133-156.
- Finch, R., and Murakami, T. (1999) Systematics and paragenesis of uranium minerals. In P.C. Burns, and R. Finch, Eds. *Uranium: Mineralogy, Geochemistry, and the Environment*, 38, p. 91-179.
- Finn, P.A., Hoh, J.C., Wolf, S.F., Slater, S.A., and Bates, J.K. (1996) The release of uranium, plutonium, cesium, strontium, technetium and iodine from spent fuel under unsaturated conditions. *Radiochimica Acta*, 74, 65-71.
- Forbes, T.Z., and Burns, P.C. (2006) Ba(NpO<sub>2</sub>)(PO<sub>4</sub>)(H<sub>2</sub>O), its relationship to the uranophane group, and implications for Np incorporation in uranyl minerals. *American Mineralogist*, 91(7), 1089-1093.
- (2007) The crystal structures of X(NpO<sub>2</sub>)(PO<sub>4</sub>)(H<sub>2</sub>O)<sub>3</sub> (X = K<sup>+</sup>, Na<sup>+</sup>, Rb<sup>+</sup>, NH<sub>4</sub><sup>+</sup>) and their relationship to the autunite group. *Canadian Mineralogist*, 45, 471-477.
  - (2008) Synthesis, structure, and infrared spectroscopy of the first Np<sup>5+</sup> neptunyl silicates, Li<sub>6</sub>(NpO<sub>2</sub>)<sub>4</sub>(H<sub>2</sub>Si<sub>2</sub>O<sub>7</sub>)(HSiO<sub>4</sub>)<sub>2</sub>(H<sub>2</sub>O)<sub>4</sub> and K<sub>3</sub>(NpO<sub>2</sub>)<sub>3</sub>(Si<sub>2</sub>O<sub>7</sub>). *Inorganic Chemistry*, 47(2), 705-712.
- Forbes, T.Z., Wallace, C., and Burns, P.C. (2008) Neptunyl compounds: Polyhedron geometries, bond-valence parameters, and structural hierarchy. *The Canadian Mineralogist*, 46(6), 1623-1645.
- Fortner, J.A., Finch, R.J., Kropf, A.J., and Cunnane, J.C. (2004) Re-evaluating neptunium in uranyl phases derived from corroded spent fuel. *Nuclear Technology*, 148(2), 174-180.
- Friese, J.I., Douglas, M., Buck, E.C., Clark, S.B., and Hanson, B.D. (2004) Neptunium(V) incorporation/sorption with uranium(VI) alteration products. *Scientific Basis for Nuclear Waste Management XXVIII*, 824, 127-132.
- Frondel, C., and Ito, J. (1956) Boltwoodite, a new uranium silicate. *Science*, 124(3228), 931-931.

- Kaszuba, J.P., and Runde, W.H. (1999) The aqueous geochemistry of neptunium: Dynamic control of soluble concentrations with applications to nuclear waste disposal. *Environmental Science & Technology*, 33(24), 4427-4433.
- Kesraouiouki, S., Cheeseman, C.R., and Perry, R. (1994) Natural zeolite utilization in pollution-control - A review of applications to metals effluents. *Journal of Chemical Technology and Biotechnology*, 59(2), 121-126.
- Klingensmith, A.L., and Burns, P.C. (2007) Neptunium substitution in synthetic uranophane and soddyite. *American Mineralogist*, 92(11-12), 1946-1951.
- Klingensmith, A.L., Deely, K.M., Kinman, W.S., Kelly, V., and Burns, P.C. (2007) Neptunium incorporation in sodium-substituted metaschoepite. *American Mineralogist*, 92(4), 662-669.
- Locock, A.J., and Burns, P.C. (2003) The crystal structure of synthetic autunite,  $\text{Ca}[(\text{UO}_2)(\text{PO}_4)]_2(\text{H}_2\text{O})_{11}$ . *American Mineralogist*, 88(1), 240-244.
- Murphy, W.M., and Grambow, B. (2008) Thermodynamic interpretation of neptunium coprecipitation in uranophane for application to the Yucca Mountain repository. *Radiochimica Acta*, 96(9-11), 563-567.
- Nitsche, H. (1991) Solubility studies of transuranium elements for nuclear waste-disposal - Principles and overview. *Radiochimica Acta*, 52-3, 3-8.
- Ostanin, S., and Zeller, P. (2007) Ab initio study of the uranyl oxide hydrates: a proton transfer mediated by water. *Journal of Physics-Condensed Matter*, 19(24).
- Perdew, J.P., Burke, K., and Ernzerhof, M. (1996) Generalized gradient approximation made simple. *Physical Review Letters*, 77(18), 3865-3868.
- Robie, R.A., and Hemingway, B.S. (1995) Thermodynamic properties of minerals and related substances at 298.15 K and 1 bar (10 p5 s pascals) pressure and at higher temperatures. *U.S. Geological Survey Bulletin*, 2131, p. 461.
- Rosso, K.M., Rustad, J.R., and Bylaska, E.J. (2001) The Cs/K exchange in muscovite interlayers: An ab initio treatment. *Clays and Clay Minerals*, 49(6), 500-513.
- Sassani, D.C., Van Luik, A., and Summerson, J. (2006) Neptunium solubility in the near-field environment of a proposed Yucca Mountain repository. *Scientific Basis for Nuclear Waste Management XXIX*, 932, 991-998.

- Segall, M.D., Lindan, P.J.D., Probert, M.J., Pickard, C.J., Hasnip, P.J., Clark, S.J., and Payne, M.C. (2002) First-principles simulation: ideas, illustrations and the CASTEP code. *Journal of Physics-Condensed Matter*, 14(11), 2717-2744.
- Shannon, R.D. (1976) Revised effective ionic-radii and systematic studies of interatomic distances in halides and chalcogenides. *Acta Crystallographica Section A*, 32, 751-767.
- Shi, W.Y., Shao, H.B., Li, H., Shao, M.A., and Du, S. (2009) Progress in the remediation of hazardous heavy metal-polluted soils by natural zeolite. *Journal of Hazardous Materials*, 170(1), 1-6.
- Shuller, L.C., Ewing, R.C., and Becker, U. (2010) Quantum-mechanical evaluation of Np-incorporation into studtite. *American Mineralogist*, 95, 1151-1160.
- Skomurski, F.N., Rosso, K.M., Krupka, K.M., and McGrail, B.P. (2010) Technetium incorporation into hematite ( $\alpha$ -Fe<sub>2</sub>O<sub>3</sub>). *Environmental Science & Technology*, 44, 5855-5861.
- Stohl, F.V., and Smith, D.K. (1981) The crystal-chemistry of the uranyl silicate minerals. *American Mineralogist*, 66(5-6), 610-625.
- Sullivan, J.C., Zielen, A.J., and Hindman, J.C. (1961) Specific interaction between Np(V) and U(VI) in aqueous perchloric acid media. *Journal of the American Chemical Society*, 83(16), 3373.
- Vanderbilt, D. (1990) Soft self-consistent pseudopotentials in a generalized eigenvalue formalism. *Physical Review B*, 41(11), 7892-7895.
- Vochten, R., Blaton, N., Peeters, O., Van Springel, K., and Van Haverbeke, L. (1997) A new method of synthesis of boltwoodite and of formation of sodium boltwoodite, uranophane, sklodowskite, and kasolite from boltwoodite. *Canadian Mineralogist*, 35, 735-741.
- Wall, N.A., Clark, S.B., and McHale, J.L. (2010) Synthesis and characterization of 1:1 layered uranyl silicate mineral phases. *Chemical Geology*, 274(3-4), 149-157.
- Wong, V., Goodell, P.C., and Anthony, E.Y. (1999) Characterization of U-series disequilibria at the Pena Blanca natural analogue site, Chihuahua, Mexico. *Scientific Basis for Nuclear Waste Management XXII*, 556, 801-808.

Wronkiewicz, D.J., Bates, J.K., Wolf, S.F., and Buck, E.C. (1996) Ten-year results from unsaturated drip tests with UO<sub>2</sub> at 90 degrees C: Implications for the corrosion of spent nuclear fuel. *Journal of Nuclear Materials*, 238(1), 78-95.

# **Chapter 6**

## **Conclusions**

Materials challenges are present at every stage of the nuclear fuel cycle: *i*) mining and milling uranium ore, *ii*) in reactor performance of nuclear fuels, and *iii*) the long-term storage of nuclear waste forms. In particular, the properties and behavior of actinide solids is of great interest because of their environmental impact, their use in nuclear fuels, and their potential to be diverted as fissile material, *e.g.*, for use as nuclear weapons. For each of these issues, the mechanisms for and degree of incorporation of the actinides into materials is of critical interest. This thesis has focused on the use of computational methods to evaluate the solid-solution behavior in oxide fuels and in two of the principal alteration products of U-based nuclear fuels in a disposal environment. In each case, every effort was made to compare the computational results to experimental data or naturally-occurring actinide phases.

Every calculation has to make simplifying assumptions as to compromise between computational rigor and complexity of the system to be calculated. A quantum-mechanical approach was applied to get a relatively accurate idea of the energetics of different configurations for the solid-solution calculations and the same for different Np-incorporation mechanisms. The calculation of thermodynamic mixing properties for the

solid solutions containing many cations requires the additional implementation of Monte-Carlo simulations to adequately scale-up the system. For the solid solutions, a significant number of configurations had to be calculated, and for the alteration phases, in addition to their large unit cells, a number of incorporation mechanisms had to be analyzed. Thus, a traditional density functional theory (DFT) approach had to be chosen that did not include the highest level of computational rigor. Among the computational rigors are relativistic effects that can be explicitly treated or partially dealt with in the pseudopotentials.

In addition, the quantum-mechanical treatment of highly-correlated 5f electrons can be corrected using the Hubbard U method. For certain properties (*e.g.*, electronic properties) the inclusion of a Hubbard U correctional term improves the computational results (Gupta et al., 2007). Based on a preliminary comparison for the Th-U binary with and without the Hubbard U parameter, there is no clear trend in the resulting enthalpies of mixing (*i.e.*, increasing Hubbard U does not necessarily continually decrease the enthalpy of mixing). However, increasing the Hubbard U tends to promote the ideality of the Th-U solid solution. Experimental evidence does not confirm or reject the notion of a complete solid solution for the Th-U binary. The question of applying the Hubbard U method to our calculations arises from having to choose the value for the Hubbard U parameter, which is often empirically determined based on a specific property (*e.g.*, band gap, vibrational frequencies).

Based on the current DFT calculations and MC simulations in **Chapter 2**, the Th-U binary oxide would have a thermodynamic tendency exsolve only at very low temperatures (below room temperature). The exsolution lamellae are || to a linear

combination of  $\{111\}$  and  $\{100\}$ ; thus, the exsolution of the system is frustrated by choosing which symmetrically-equivalent linear combination of planes to exsolve parallel to. Kinetic hindrances tend to over-power the exsolution above room temperature. One such kinetic hindrance is the interfacial energy caused by the strain from the lattice mismatch of the exsolved end-members. Additionally, cation diffusion in oxides is slow, especially at low  $T$ ; therefore, further hindering exsolution. The thermodynamic properties of the Th-Ce binary (**Chapter 3**) are similar to the Th-U binary; however, no exsolution lamellae are observed, even at low  $T$ . Both binaries have only slightly positive enthalpies of mixing; thus, the solid solutions are nearly ideal. Conversely, the Ce-Zr and Th-Zr binaries (**Chapter 3**) have highly positive enthalpies of mixing and a significant drop in their configurational entropy at  $x = 0.5$  at low  $T$ . The drop in configurational entropy corresponds to nanoscale exsolution in the Ce-Zr binary (lamellae  $\parallel (10\bar{2})$  or any other linear combination of  $\{101\}$  and  $\{001\}$ ) and cation ordering in the Th-Zr binary. Further calculations considering a tetragonal or monoclinic  $ZrO_2$  end-member are necessary (and under way) to fully understand the solid-solution behavior of this system in all different structural frameworks. Overall, this computational approach for an atomistic investigation of binary oxide solid-solutions provides insight into the short-range cation-cation interactions that impact the miscibility of the solid solution and allows for the investigation of the energetics of different homogeneous and heterogeneous ordering schemes and for the comparison of different directions for exsolution within the isometric structure.

In **Chapters 4 and 5**, quantum-mechanical calculations were used to determine the energy required to incorporating Np into uranyl minerals, specifically studtite and

boltwoodite. Np<sup>6+</sup>-incorporation is more energetically favorable than Np<sup>5+</sup>-incorporation into studtite. Additionally, Np<sup>6+</sup> is completely miscible in studtite at room temperature with respect to a hypothetical Np<sup>6+</sup>-studtite end member that has a favorable enthalpy of formation based on a calculation from the oxides. Additionally, the electronic structure calculations provide insight into the Np-bonding environment in studtite, where the Np 5f orbitals occupy the space in the band gap of studtite narrowing the band gap from 2.29 eV to 1.09 eV.

For Np<sup>5+</sup>-incorporation, three charge-balancing mechanisms were compared: *i*) addition of H<sup>+</sup> [ $E_{\text{incorp}}(\text{studtite}) = 1.12 \text{ eV}$ ;  $E_{\text{incorp}}(\text{boltwoodite}) = 0.79 \text{ eV}$ ], *ii*) interlayer coupled-substitution [ $E_{\text{incorp}}(\text{boltwoodite}) = 1.20 \text{ eV}$ ], *iii*) intra-layer substitution [ $E_{\text{incorp}}(\text{boltwoodite}) = 0.87 \text{ eV}$ ]. In addition to the incorporation mechanism, the incorporation energy is highly dependent on the choice of source/sink phases for the substituted cations. For example, the incorporation energy for the interlayer coupled-substitution mechanism decreased from 2.4 eV to 1.2 eV by changing the source/sink phases for the interlayer cations from oxides to silicates. Most significant was the use, for the first time, of aqueous complexes as source/sink phases in reactions with crystalline phases. The aqueous reference phases are much more realistic to the actual sources and sinks in geologic settings; however, they have not been previously used due to the challenges of combining periodic and cluster calculations to derive the energy of a reaction containing both. By keeping the computational theory consistent within chemical reactions and combining reactions using  $\Delta E_{\text{reaction}}$ , we were able convert a reaction using neutral molecules (calculated in a periodic framework), which are not likely to exist in nature, to charged aqueous species (calculated in a cluster framework).

Finally, solid-solution calculations for  $\text{Np}^{5+}$  and  $\text{P}^{5+}$  substitution for  $\text{U}^{6+}$  and  $\text{Si}^{4+}$  in boltwoodite indicate that, at 300 °C, the incorporation limit is about 585 ppm, which is within the same order of magnitude as experimental results that show that hundreds of ppm of Np can be incorporated into uranyl minerals (*e.g.*, Na-compreignacite) that are synthesized at about 100 °C (Burns et al., 2004).

There are several limitations to the quantum-mechanical calculations that make the results more qualitative than quantitative. First, the systems need to remain small (less than 100 atoms is ideal) because the time for the calculation increases by the number of electrons cubed. Thus, accurate modeling of the mineral structures is challenging. For example,  $\text{UO}_2$  typically oxidizes to  $\text{UO}_{2+x}$  ( $x < 0.25$ ) and the solid-solution properties of  $\text{Th}_x\text{U}_{1-x}\text{O}_2$  may vary with the change in oxygen potential. Thus, simplified binary oxide solid solutions were evaluated to gain insight into the cation-cation ordering. The size limitation also played a significant role in the Np-incorporation calculations, where the minimum concentration of Np evaluated quantum-mechanically was 0.25 atomic percent for studtite and 0.5 atomic percent for boltwoodite. Conversely, experiments have shown that Np-incorporation limits are on the order of hundreds of ppm. In order to compare the incorporation limit for the calculation with experimental measurements, solid-solutions properties were estimated based on limited quantum-mechanical configurations.

In order to be sure that the computational limitations do not hinder the integrity of the calculations, results are validated with experimental measurements whenever possible. Most commonly, structural measurements (*i.e.*, unit cell parameters and volume) are compared. Validation of thermodynamic properties, such as enthalpy of formation or free energy of mixing, can be done using calorimetric measurements. For example,

calorimetric measurements of the enthalpy and free energy of mixing were compared to solid solution calculations of  $\text{Th}_x\text{U}_{1-x}\text{O}_2$  in Chapter 2. Similarly, calorimetric measurements were used to validate calculations in Chapter 4 (*e.g.*, the calculated and measured enthalpies of formation of studtite were comparable).

Finally, measurements of the limit of incorporation were compared with the calculated limit of incorporation (Chapter 5). Although the incorporation limit was determined for different uranyl minerals under different environmental conditions (*e.g.*, pH plays a large role in the incorporation limit for experimental studies), the results provide a qualitative confirmation that uranyl minerals may be a viable means of Np immobilization in a geologic environment.

For accurate validation of the solid-solution calculations, it is imperative that systematic calorimetric measurements be complete for each binary. Additionally, transmission electron microscopy (TEM) is a powerful tool for imaging on the nanoscale and can be used to validate possible cation-ordering or nano-scale exsolution; however, for the binary oxides discussed in Chapters 2 and 3, no TEM results are available.

For the oxide solid solutions, future work is needed to add complexity to the system, including not only changing oxygen potential, but also to determine the diffusion of oxygen and cations within the solid solutions. However, quantum-mechanical calculations are inherently static calculations; therefore, kinetic components, such as diffusion, should be calculated with empirical potentials developed from accurate quantum-mechanical calculations, or can be incorporated by using the energetics of static diffusion paths in the crystal.

For the Np-immobilization in uranyl minerals, better synergy between computational and experimental efforts will expedite the amount of knowledge gained concerning immobilization mechanisms and the limit of immobilization. For example, the present calculations indicate that  $\text{Ca}^{2+}$  may more likely exchange in Na-boltwoodite than K-boltwoodite. This theory could be tested experimentally. The synthesis of Np-doped uranyl minerals in the presence of different charge-balancing cations could also be tested experimentally. On the computational front, diffusion of cations, in particular  $\text{NpO}_2^+$ , through the interlayer, as well as the uranyl sheet, should be evaluated in order to determine possible diffusion pathways and gain insight into the kinetics of Np-incorporation into uranyl minerals.

Finally, a more thorough comparison of DFT and beyond-DFT theories is necessary to confirm the solid-solution properties of actinide-containing materials. The Hubbard U parameter has been shown to correct for the over-bonding of the U 5f electrons that cause the metallic-like behavior in traditional DFT. However, the Hubbard U parameter is an empirical fit parameter; therefore, the predictive power of calculations using such a theory is limited. The development of advanced computational theories are necessary to accurately treat highly-correlated systems; however, in the meantime, a thorough comparison of materials properties (*e.g.*, electronic, optical, mechanical) based on different computational approaches (*e.g.*, DFT, Hubbard U, Hybrid) on a variety of actinide-containing systems (*e.g.*, simple and complex oxides, metals) can be undertaken.

In summary, atomistic calculations were used to determine properties of actinide-bearing oxides that may influence behavior of the material during fabrication of the fuel, performance in the reactor, and stability as waste form. The simplified approach taken

for the calculations in this thesis lays the groundwork for more complex future calculations, both in terms of the computational approach for handling highly-correlated 5f electrons or the computational set-up for dealing with more complex systems.

## References

- Burns, P.C., Deely, K.M., and Skanthakumar, S. (2004) Neptunium incorporation into uranyl compounds that form as alteration products of spent nuclear fuel: Implications for geologic repository performance. *Radiochimica Acta*, 92(3), 151-159.
- Gupta, F., Brilliant, G., and Pasturel, A. (2007) Correlation effects and energetics of point defects in uranium dioxide: a first principle investigation. *Philosophical Magazine*, 87(16-17), 2561-2569.